Master thesis and internship[BR]- Master's thesis : Identification of nonlinear frequency response and backbone curves using phase-locked loop methods[BR]- Integration internship

Auteur : Marchant, Louise
Promoteur(s) : Kerschen, Gaëtan
Faculté : Faculté des Sciences appliquées
Diplôme : Master en ingénieur civil en aérospatiale, à finalité spécialisée en "aerospace engineering"
Année académique : 2024-2025
URI/URL : http://hdl.handle.net/2268.2/23340

Identification of nonlinear frequency response and backbone curves using phase-locked loop methods

Master's Thesis

Author

Louise Marchant

Supervised by

Prof. Gaëtan Kerschen

A Thesis submitted in fulfillment of requirements for the degree of
Master of Science in Aerospace Engineering

University of Liège
Faculty of Applied Sciences

Academic year 2024-2025

Examination committee

President

Prof. Gaëtan Kerschen
University of Liège

Academic supervisor

Prof. Gaëtan Kerschen
University of Liège

Industrial supervisor

Sophie Denis
V2i

Members

Dr. Ghislain Raze
University of Liège

Prof. Loïc Salles
University of Liège

Abstract

Vibration testing plays an important role in the development of modern engineering structures by revealing their dynamic limitations, providing validation data for numerical models, and serving as a benchmark in standardised testing procedures. While modal analysis of linear systems is a well-established process, with linear systems characterised by constant resonance frequencies regardless of excitation amplitude, the adoption of novel materials and complex structures in the aeronautical industry has led to the increased occurrence of nonlinear phenomena. Such systems may exhibit multiple stable and unstable solutions, superharmonic and subharmonic resonances, and amplitude-dependent frequency responses, thereby challenging classical identification techniques in the reconstruction of complete bifurcation diagrams.

To identify complete frequency response and backbone curves of nonlinear structures, experimental continuation methods have recently gained interest. This thesis investigates the implementation of a phase-locked loop (PLL) algorithm in the LabVIEW FPGA environment to perform real-time tracking of fundamental frequency response and backbone curves, with a view towards industrial application.

The PLL approach is first developed within the Simulink environment as a reference model, and is validated numerically and experimentally. The algorithm is then implemented in LabVIEW, and multiple tests are performed on experimental setups. Results demonstrate that the LabVIEW-based PLL achieves real-time computation of frequency response and backbone curves with an accuracy comparable to that of the Simulink implementation. An industrial application of the present work can be considered to track frequency response and backbone curves of fundamental resonances of nonlinear systems. However, instabilities arising from the inappropriate calibration of controller gains when identifying unstable responses prevent a smooth application of the method, and a robust technique for determining these gains has yet to be established.

Keywords: Nonlinear dynamics, Experimental continuation, Phase-locked loop method, Nonlinear frequency response curve, Backbone curve

Résumé

Les essais vibratoires jouent un rôle essentiel dans le développement des structures d'ingénierie modernes, en révélant leurs limitations dynamiques, en fournissant des données de validation pour des modèles numériques, et en servant de référence dans les procédures d'essais normalisées. Alors que l'analyse modale des systèmes linéaires est un processus bien établi, où les systèmes linéaires sont caractérisés par des fréquences de résonance indépendantes de l'amplitude d'excitation, l'adoption croissante de matériaux innovants et de structures complexes dans l'industrie aéronautique met de plus en plus en évidence des phénomènes non-linéaires. De tels systèmes peuvent présenter plusieurs solutions stables et instables, des résonances super-harmoniques et sous-harmoniques, ainsi que des réponses en fréquence qui dépendent de l'amplitude d'excitation, que les techniques classiques d'identification ne permettent pas de distinguer.

Afin d'identifier les courbes complètes de réponse en fréquence des structures non-linéaires, les méthodes de continuation expérimentale suscitent un intérêt croissant. Cette thèse investigue la mise en œuvre d'un algorithme de boucle à verrouillage de phase (PLL) dans l'environnement LabVIEW FPGA, permettant le suivi en temps réel de réponses fréquentielles, dans une optique d'application industrielle.

La méthode de boucle à verrouillage de phase est premièrement développée dans l'environnement Simulink en tant que modèle de référence, et est validée numériquement et expérimentalement. L'algorithme est ensuite implémenté dans LabVIEW, et plusieurs essais sont réalisés sur des bancs expérimentaux. Les résultats montrent que la PLL implémentée sur LabVIEW permet un calcul en temps réel des courbes de réponse en fréquence avec une précision comparable à celle obtenue avec Simulink. Une application industrielle des travaux présentés peut être envisagée pour le suivi des courbes de réponses en fréquence et de lieu des points de résonance associées aux résonances fondamentales des systèmes non-linéaires. Cependant, les instabilités découlant d'une calibration inapropriée des gains du contrôleur lors de l'identification de réponses instables empêche une application fluide de la méthode, et une technique robuste pour déterminer ces gains reste à établir.

Mots-clés : Dynamique non-linéaire, Continuation expérimentale, Méthode de boucle à verrouillage de phase, Courbe de réponse en fréquence non-linéaire, Courbe de lieu des points de résonance

Acknowledgements

First and foremost, I would like to express my gratitude to my academic supervisor, Professor Gaëtan Kerschen, for his continuous support, availability, and invaluable guidance throughout this Master's thesis.

I am also grateful to Sébastien Hoffait for giving me the opportunity to undertake my internship at V2i. I am equally thankful to Sophie Denis for her constant availability, support, and technical guidance during this internship. I also extend my thanks to Jérôme Ligot for giving me precious advice on the technical aspects of LabVIEW. More broadly, I am grateful to the entire V2i team for their warm welcome, which greatly facilitated my integration and allowed me to make the most of this enriching experience.

I would like to thank Dr. Ghislain Raze and François Winand for generously sharing their expertise on phase-locked loop methods, and for their valuable advice throughout this work.

Finally, I am grateful to my family and friends, and especially to Anaïs and Luca, for their unfaltering support and for being a constant source of encouragement.

Alejandro, thank you for your love and support, especially during the moments I needed it most. Your reassuring presence has been invaluable.

Contents

1 Introduction **1**
1.1 Objectives . . . 4

2 Theory of linear and nonlinear vibrations **5**
2.1 Linear systems . . . 5
2.1.1 Single-degree-of-freedom conservative systems . . . 6
2.1.2 Linear normal modes . . . 7
2.1.3 Multiple-degree-of-freedom forced and damped systems . . . 8
2.2 Nonlinear systems . . . 10
2.2.1 Single-degree-of-freedom conservative systems . . . 10
2.2.2 Nonlinear normal modes . . . 12
2.2.3 Multiple-degree-of-freedom forced and damped systems . . . 13
2.3 Characteristics of nonlinear systems . . . 13
2.3.1 Backbone curve . . . 13
2.3.2 Nonlinear frequency response curve . . . 14
2.3.3 Bifurcation . . . 15
2.3.4 Secondary resonance . . . 15
2.4 Conclusion . . . 16

3 Introduction to control systems **18**
3.1 Open-loop and closed-loop control systems . . . 18
3.2 Fundamental principles of feedback control systems . . . 19
3.3 PID control and gain adjustments . . . 20
3.3.1 Proportional gain . . . 21
3.3.2 Integral gain . . . 21
3.3.3 Derivative gain . . . 21
3.3.4 Summary of gain tuning for PID controllers . . . 22
3.4 Conclusion . . . 23

4 Phase-locked loop algorithms **25**
4.1 Introduction . . . 25
4.2 Presentation of the algorithm . . . 26
4.3 Adaptive filters . . . 27
4.4 Identification of backbone curves . . . 29
4.5 Identification of frequency response curves . . . 30
4.6 Gain tuning of the PI controller . . . 30
4.7 Parameter selection . . . 32

4.8 Conclusion . . . 32

5 Numerical applications of the phase-locked loop method 34
5.1 Practical considerations on the implementation . . . 34
5.2 Methodology . . . 34
5.3 Single-degree-of-freedom linear system . . . 35
5.4 Single-degree-of-freedom nonlinear Duffing oscillator . . . 36
5.5 Single-degree-of-freedom softening-hardening system . . . 37
5.6 Parameter analysis . . . 38
5.7 Conclusion . . . 40

6 Experimental validation of the phase-locked loop method implemented in Simulink 42
6.1 Methodology . . . 42
6.2 Practical considerations . . . 42
6.3 Electronic Duffing oscillator . . . 43
6.3.1 Setup description . . . 43
6.3.2 Results . . . 44
6.4 Nonlinear beam . . . 46
6.4.1 Setup description . . . 46
6.4.2 Results . . . 47
6.5 Effects of controller gain tuning on the performance of the phase-locked loop method 52
6.6 Conclusion . . . 52

7 Implementation of a phase-locked loop method in LabVIEW 54
7.1 Presentation of LabVIEW . . . 54
7.2 Introduction to FPGA . . . 54
7.2.1 Architecture of an FPGA chip . . . 55
7.3 Integration of FPGA hardware in LabVIEW . . . 55
7.3.1 CompactRIO . . . 56
7.3.2 Modules I/O . . . 58
7.4 Implementation considerations . . . 59
7.4.1 Data type . . . 59
7.4.2 Data size . . . 59
7.4.3 Throughput versus latency . . . 60
7.4.4 Pipelining . . . 60
7.5 Comparison of the implementations of the method in Simulink and LabVIEW . . . 61
7.6 Conclusion . . . 62

8 Experimental validation of the phase-locked loop method implemented in LabVIEW 63
8.1 Methodology . . . 63
8.2 Nonlinear beam . . . 63
8.2.1 Setup description . . . 64
8.2.2 Results . . . 64
8.3 Bolted beam . . . 64
8.3.1 Setup description . . . 65
8.3.2 Results . . . 65
8.4 Thin nonlinear beam . . . 67
8.4.1 Setup description . . . 67

8.4.2 Results 68
8.5 Conclusion and remaining challenges 71

9 Nonlinear controller for the phase-locked loop method **73**
9.1 Presentation of the nonlinear controller 73
9.2 Review of the method 74
9.3 Conclusion 75

10 Conclusions and perspectives **76**
10.1 Future work 77

Bibliography **79**

A Simulink diagrams **85**
A.1 Phase-locked loop method 85

B Experimental modal analysis of the nonlinear beam **87**
B.1 Setup description 87
B.2 Results 87

1 Introduction

The analysis of structural vibrations is a fundamental practice in engineering, as all bodies constituting the universe are in a state of perpetual motion. Vibration testing is a standard procedure in the development of engineering systems, employed for various purposes ranging from the experimental characterisation of aerospace components during the development phase to the modal analysis and structural health monitoring of large-scale civil infrastructures. It plays a critical role in the validation and verification processes of engineered systems.

In industrial applications, it is often convenient to assume that systems behave linearly, as this assumption considerably simplifies their analysis. However, in practice, few systems are truly linear. Nonlinearities are ubiquitous in real-world systems — present not only in engineered structures but also in natural systems, including biological structures [1]. Nonlinear systems exhibit distinct behaviours, which can vary from complex and unpredictable responses to fully chaotic dynamics. As a result, understanding and characterising these nonlinear behaviours remain both a challenging and essential aspect of system analysis.

In linear systems, the *principle of superposition* holds. The principle of superposition is defined by two properties: *additivity* and *homogeneity*. The first one claims that the response of a system to an excitation composed of multiple sources is equal to the sum of the response to each source individually. The homogeneity property states that scaling the input results in a proportional scaling of the output. The properties of additivity and homogeneity significantly facilitate the analysis of vibrating linear systems, as they allow the response to complex excitations to be decomposed into a superposition of simpler, more tractable problems. Moreover, linear structural dynamics relies on three main assumptions. The first one assumes that materials exhibit linear elastic behaviour, as described by Hooke's law. It is also assumed that structures undergo small rotations and displacements, and that the damping is directly proportional to the velocity of the structure, a property also known as *viscous damping*.

Nonlinear systems, however, exhibit fundamentally different dynamic behaviours. The origins of nonlinearities are varied. For instance, nonlinearities may arise from friction, as investigated by Ackermann and Müller [2], from material properties, such as nonlinear composites or viscoelastic materials [3, 4]. Nonlinear effects may also originate from geometric aspects, as observed, for example, in large deformations of rotors [5], or from boundary conditions [6]. Finally, interaction nonlinearities can also occur, as in fluid-structure interactions.

In the aeronautical industry, nonlinear analysis is becoming progressively more prevalent. The introduction of new materials and connection mechanisms has led to the identification of sources of nonlinearities within aeronautical systems. For example, the nonlinear dynamics of an F-16 aircraft has been investigated multiple times, as in [7, 8], where it is observed that nonlinearities arise in the mechanisms linking the payload fixed to the wing of the military aircraft and the wing itself.

Another contemporary example is the open-fan architecture engine introduced in the framework of the RISE (Revolutionary Innovation for Sustainable Engines) program [9], a collaborative initiative led by CFM International. Extensive research is being conducted on this next generation of engines, as they promise significant reduction of CO_2 emissions and fuel consumption, thereby making a substantial contribution towards achieving European greenhouse gas reduction targets.

In such open-rotor engines, the mounting of engine components, such as the heat exchanger or oil reservoir, poses considerable challenges. Indeed, in this type of architecture, components must not only be securely mounted to the structure but must also be capable of withstanding significant thermal, mechanical, and vibrational loads. Within this context, Walloon companies in the aeronautical sector explore structural technologies capable of withstanding extreme temperatures while also resisting high-level vibrations. One of the proposed solutions involves transitioning from rigid to flexible connections, including the use of non-rigid joints, spherical bearings, or sliding systems, which allow for controlled movement and thermal expansion. However, these newly proposed solutions are accompanied by complex dynamic phenomena, including nonlinear behaviours arising from clearance, friction, and intermittent contact within the flexible connections.

Experimental vibration testing of such aeronautical systems is crucial for validating the corresponding numerical models, which are subsequently used to predict system behaviour under specified loading. Furthermore, vibration testing is critical for verifying the structural design in accordance with the RTCA-DO standard, a widely recognised benchmark for structural qualification in the aerospace industry. During these tests, the structure is typically mounted on a shaker, which is used to excite the structure. Depending on the experimental objectives, the excitation force generated by the shaker may vary; for instance, it may consist of broadband random noise, a sine sweep signal, or a sinusoidal excitation with a controlled frequency, as typically employed in dwell testing. The structural response is measured using accelerometers and strain gauges strategically positioned on the system, which, in certain cases, may exhibit nonlinear behaviour.

When experimentally testing systems that exhibit nonlinearities, such as systems equipped with semi-flexible fixtures, V2i's vibration testing methodology encounters some challenges due to the linearity assumption embedded in the shaker control loop, which presumes a linear transfer function between the excitation and the response. In such cases, nonlinearities can arise, disrupting the linear relationship on which the control loop relies. The main current limitations are the inability to predict the unstable branches of *frequency response functions* (FRFs), called *nonlinear frequency response curves* (NFRCs) in nonlinear systems, which hinders a complete characterisation of the system's dynamics and prevents the development and validation of accurate numerical models. Additionally, dwell testing poses challenges due to control difficulties and instabilities arising from resonant amplification or damping behaviour, which can shift unpredictably as a result of sudden response *jumps*. Illustration of such behaviours are reported in Figure 1.1, namely level-dependent NFRCs in Figure 1.1a and jumps in Figure 1.1b.

Figure 1.2 illustrates the theoretical relevance of continuation methods in recovering the bifurcation diagram near the fundamental resonance of a nonlinear system. The NFRC is superimposed on the frequency response obtained using linear identification techniques, highlighting the ability of continuation methods to reveal inaccessible solution branches.

As related by Raze *et al.* [10], a variety of continuation methods have emerged since the early work on experimental nonlinear dynamics [11]. The first experimental continuation method implemented was the *control-based continuation* (CBC), which was introduced by Sieber *et al.* [12]. The main drawback of CBC is that it requires the computation of derivatives from experimental data, a procedure

that is highly sensitive to noise and computationally demanding. Since then, various *derivative-less* experimental continuation methods have emerged, such as the *phase-locked loop* (PLL) [13] or *response-control testing* (RCT) [14] methods. These methods have recently attracted considerable interest in the field of experimental nonlinear dynamics, as they offer a promising alternative for the experimental determination of NFRCs and *backbone curves*.

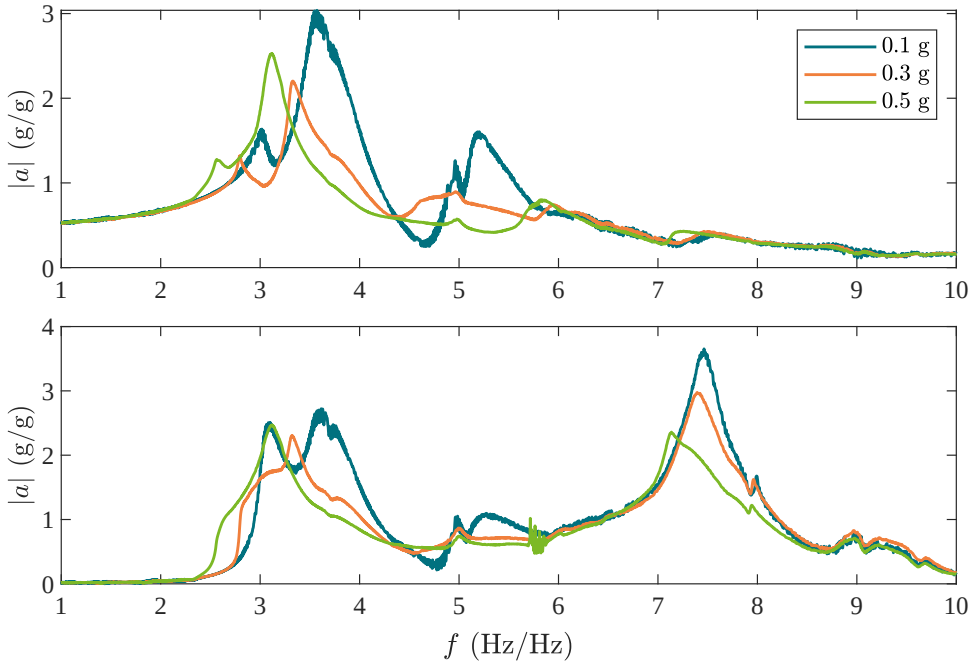

(a) FRFs measured experimentally at two locations for various amplitudes of excitation. Shifts of the resonance peaks are observed with varying amplitudes of excitation.

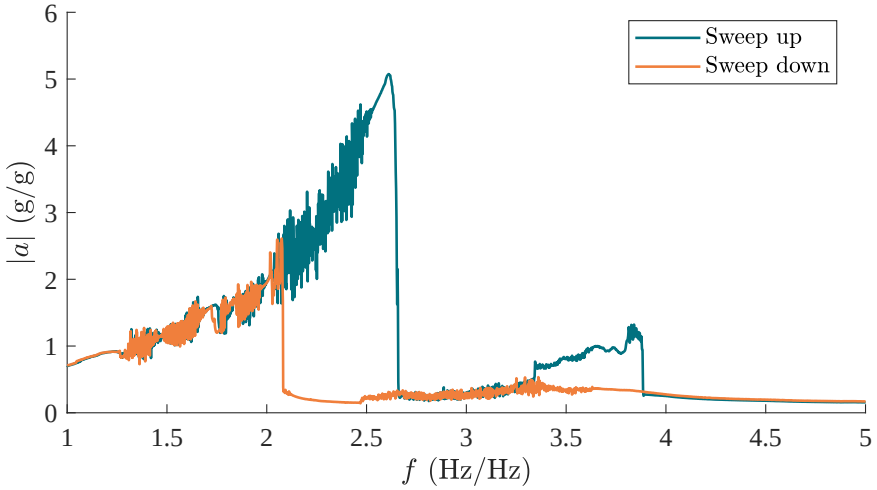

(b) FRFs measured experimentally when performing sine sweep up and down excitations at dwell testing level. Jump phenomena are observed.

Figure 1.1: Examples of nonlinear behaviours observed in industry during vibration testing (courtesy of V2i).

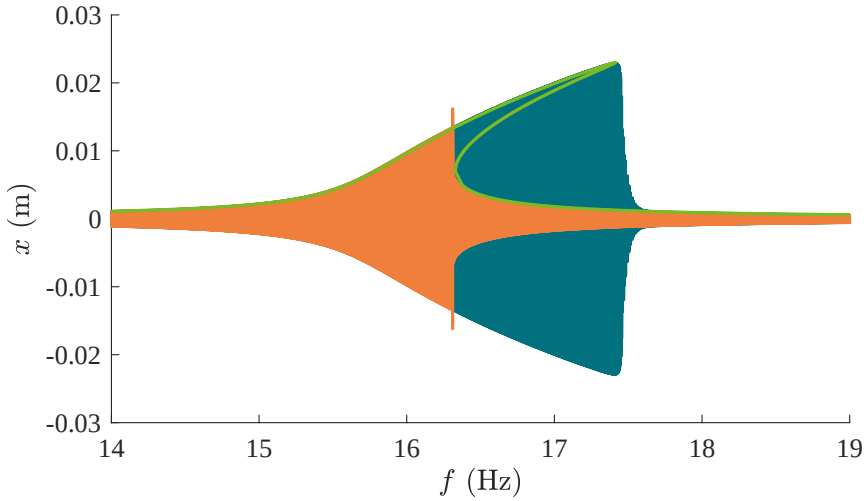

Figure 1.2: Response of a nonlinear system to sweep up (—) and down (—) excitations of the same amplitude. The corresponding NFRC computed with a continuation method is also depicted (—).

1.1 Objectives

The objectives of this Master's thesis are to explore the feasibility and practicality of employing a PLL method to track the fundamental resonance curves of nonlinear industrial systems, and to assess its applicability at the V2i company. Specifically, the thesis investigates the potential for implementing such *real-time* method within the LabVIEW environment, which is used for application development at V2i. Additionally, the thesis will evaluate the nonlinear controller presented in the very recent work of Chukwu *et al.* [15] in its effectiveness, ease of implementation, and application being thoroughly evaluated.

The methodology of the research is the following. Initially, the PLL method will be implemented within the well-established Simulink environment. The method will then undergo numerical validation by simulating the dynamics of both linear and nonlinear systems and retrieving their NFRCs and backbone curves. Following the successful numerical validation of the PLL method in Simulink, experimental tests will be conducted on academic nonlinear systems to further validate the algorithm experimentally.

Once these tests are completed, attention will shift to LabVIEW environment. To facilitate real-time control and data acquisition, an FPGA chip will be used in conjunction with the LabVIEW FPGA module, which allows describing hardware systems graphically. The primary aim of this LabVIEW implementation is to evaluate the feasibility of performing such analyses within the LabVIEW FPGA environment, specifically focusing on whether the required computational speed is sufficient to enable experimental real-time control of nonlinear systems. Finally, experimental analyses will be conducted using the LabVIEW implementation of the PLL to evaluate the quality and performance of the method within the LabVIEW environment, and comparison will be drawn with the results obtained with PLL implementation carried out in Simulink.

This thesis concludes with an evaluation of a novel control method proposed for the feedback control of frequency within the PLL algorithm, where a nonlinear element is introduced into the controller.

2 Theory of linear and nonlinear vibrations

The theory of system vibrations is believed to have originated in antiquity, around the fifth century BC, with the Pythagoreans. These early philosophers observed that the *natural frequency* of a vibrating system is an intrinsic property, independent of the type of excitation applied. At that time, Pythagoreans experimentally established the fundamental natural frequencies of multiple simple systems, such as vibrating strings or pipes [16].

Since the early developments of vibration theory, numerous comprehensive works have emerged that delve deeply into these phenomena. Today, references such as the famous work of Géradin and Rixen [17] or Genta [18] offer extensive coverage of the current state of vibration theory. While Géradin and Rixen provided a detailed explanation of linear mechanical vibrations in both discrete and continuous systems, Genta extends the discussion to nonlinear systems and the dynamics of rotating machinery. An additional key reference in the study of nonlinear vibrating systems is the seminal work by Nayfeh and Mook [19].

This chapter introduces the fundamental principles of the theory of vibration of linear and nonlinear systems. The study begins with the introduction of the linear paradigm, and the assumptions and properties upon which linear system analysis is based. Mathematical formulations of the dynamics of single-degree-of-freedom (SDOF) and multiple-degree-of-freedom (MDOF) linear systems are presented, alongside important concepts of linear systems, namely the FRFs and *mode shapes*. The paradigm then shifts to nonlinear systems, where the simplifications arising from the linearisation of system dynamics are no longer valid. The typical sources and types of nonlinearities encountered in structures are outlined, and the characteristic behaviours of nonlinear systems are illustrated. A parallel between the exact solution of a linear SDOF conservative system and its nonlinear counterpart is derived, highlighting the fundamental differences between both system types. Finally, the concepts of *nonlinear normal modes* (NNMs) and NFRCs are introduced, alongside the presentation of phenomena intrinsic to nonlinear structures, such as bifurcations and solution instabilities.

2.1 Linear systems

Despite the widespread recognition of nonlinear phenomena in structural dynamics, the linear paradigm continues to dominate system analysis. While the fundamental principles governing mechanical systems, such as the *principle of virtual work* or *Hamilton's principle* [17], inherently lead to nonlinear equations of motion, the dynamic behaviour of such systems may, in certain engineering applications, be satisfactorily approximated by small oscillations about a static equilibrium configuration [17]. In such cases, the dynamics of the system can be significantly simplified by considering the *linearised* equations of motion about an equilibrium position. This approach, when applicable, is often favoured due to the simplicity it affords. Linear time-invariant (LTI) systems

are characterised, as previously stated, by two fundamental properties: additivity and homogeneity. These properties facilitate the computation of the response of such systems to external forces. Indeed, in linear systems, the response to a complex excitation, *e.g.,* consisting of multiple harmonics, can be decomposed into the response to each individual excitation, thereby making the computation considerably more straightforward. Moreover, in linear systems, the computation of the linear modes and their associated natural frequencies can be performed with robust standard numerical methods. Although such simplifications are undoubtedly practical, it is important to emphasise that their validity is restricted to scenarios involving small deformations and displacements. Beyond these limits, the assumption of linearised dynamics ceases to be applicable.

This section introduces the concept of *resonance* in linear SDOF and MDOF systems. The focus is also placed on the FRFs of such systems, alongside the identification of their mode shapes and natural frequencies.

2.1.1 Single-degree-of-freedom conservative systems

The following reasoning is presented to facilitate a qualitative comparison between the behaviours of linear and nonlinear conservative SDOF systems. This analysis is based on the developments presented in the lecture of *Nonlinear Vibrations of Aerospace Structures* presented by Prof. Kerschen and Dr. Raze at ULiège [20].

Consider a linear conservative SDOF system whose dynamics is driven by the following equation

$$m\ddot{x}(t) + kx(t) = 0, \tag{2.1}$$

where $x(t)$ is the system displacement, $\ddot{x}(t)$ its acceleration, m its mass and k its stiffness.

Equation 2.1 can be mass-normalised to obtain the following formulation

$$\ddot{x}(t) + \omega_0^2 x(t) = 0 \quad \text{with} \quad \omega_0 = \sqrt{k/m}, \tag{2.2}$$

where ω_0 denotes the natural frequency of the system.

Consider the system defined in Equation 2.2 with the following initial conditions in terms of velocity and displacement respectively

$$\dot{x}(0) = \dot{x}_0 \ \text{ and } \ x(0) = x_0. \tag{2.3}$$

To find the exact solution $x(t)$ of the system, Equation 2.2 is multiplied by the system velocity $\dot{x}(t)$ and subsequently integrated. The mathematical developments are detailed in [20], and the corresponding solution is given by

$$x(t) = \sqrt{x_0^2 + \frac{\dot{x}_0^2}{\omega_0^2}} \sin\left(\omega_0 t + \arctan\frac{\omega_0 x_0}{\dot{x}_0}\right). \tag{2.4}$$

Equation 2.4 provides insight into the expected behaviour of a linear conservative SDOF system. More particularly, it indicates that the amplitude of the solution will depend only on the initial conditions and the natural frequency of the system. It also indicates that the system oscillates at a frequency corresponding to its fundamental natural frequency, which depends solely on the system's physical properties and is independent of its initial conditions.

Equation 2.4 can be reformulated as follows

$$x(t) = \frac{\dot{x}_0}{\omega_0} \sin \omega_0 t + x_0 \cos \omega_0 t, \tag{2.5}$$

where the first term corresponds to the response induced by the initial velocity of the system, while the second term represents the response due to the system's initial position. The response of a linear conservative SDOF system to varying initial conditions is presented in Figure 2.2a.

2.1.2 Linear normal modes

A *linear normal mode* (LNM) of a dynamical system is defined as a *synchronous* motion, meaning that all DOFs oscillate at a common natural frequency ω_0, and reach their minima, maxima, or pass through zero simultaneously [17].

The following presentation of LNMs is sourced from [17]. LNMs can be readily introduced mathematically by developing the general form of the equations of motion of a conservative MDOF linear system

$$\boldsymbol{M}\ddot{\boldsymbol{x}}(t) + \boldsymbol{K}\boldsymbol{x}(t) = \boldsymbol{0}, \tag{2.6}$$

where $\boldsymbol{x}^T(t) = [x_1(t)\ x_2(t)\ \cdots\ x_n(t)]$ is the displacement vector, with n the number of degrees of freedom in the system, and $\boldsymbol{K}$ and $\boldsymbol{M}$ are respectively the system stiffness and mass matrices.

A particular solution of the form

$$\boldsymbol{x} = \boldsymbol{n}\phi(t), \tag{2.7}$$

where $\boldsymbol{n}$ is a vector of constant scalars, which governs the deformation shape, and $\phi(t)$ is the temporal law of motion, is sought. The solution described by Equation 2.7 is referred to as synchronous, as all degrees of freedom of the system follow the same temporal evolution.

Substituting Equation 2.7 into Equation 2.6 leads to

$$\ddot{\phi}(t)\boldsymbol{M}\boldsymbol{n} + \phi(t)\boldsymbol{K}\boldsymbol{n} = \boldsymbol{0}. \tag{2.8}$$

If the matrix $\boldsymbol{K}$ is non-singular, Equation 2.8 can be reformulated as

$$\boldsymbol{K}\boldsymbol{n} = -\frac{\ddot{\phi}(t)}{\phi(t)}\boldsymbol{M}\boldsymbol{n} = \omega^2\boldsymbol{M}\boldsymbol{n}. \tag{2.9}$$

Equation 2.9 establishes an *eigenvalue problem*, where the vector $\boldsymbol{n}$, also known as *eigenmode*, describes a free synchronous vibration motion of the system, and the variable ω^2 is its associated *eigenvalue*. The nontrivial solution $\boldsymbol{n}_{(r)}$ of this system of equations is found by computing

$$(\boldsymbol{K} - \omega_r^2\boldsymbol{M})\boldsymbol{n}_{(r)} = \boldsymbol{0}, \tag{2.10}$$

where ω_r^2 is the root of

$$\det(\boldsymbol{K} - \omega_r^2\boldsymbol{M}\boldsymbol{n}_{(r)}) = 0. \tag{2.11}$$

Equations 2.10 and 2.11 define the mode shapes and the associated natural frequencies of the system.

LNMs exhibit two principal properties of significant interest. Firstly, they are invariant, implying that a motion initiated in a given LNM remains confined to that specific mode. Secondly, both the free and forced responses of a linear mechanical system can be represented as a linear combination of several distinct LNMs [21].

The computation of LNMs is particularly useful in vibration analysis, as they provide valuable physical insight into the structural deformation of the system at resonance. Specifically, they provide information regarding the locations of maximum deformation within the structure. For instance, when performing experimental measurements at resonance, it is crucial to place the sensors away from *vibration nodes*, where the deformation of an MDOF structure in response to an excitation force is null. Consequently, measurements taken at these nodes will result in the absence of resonance identification in the FRF. A similar outcome will occur if the excitation force is applied at a vibration node or if it is oriented perpendicular to the direction of the structural deformation of the mode shape.

2.1.3 Multiple-degree-of-freedom forced and damped systems

The equations of motion of a damped and forced linear MDOF system can be derived from the conservative counterpart (Equation 2.6) by adding damping and external excitation

$$\boldsymbol{M}\ddot{\boldsymbol{x}}(t) + \boldsymbol{C}\dot{\boldsymbol{x}}(t) + \boldsymbol{K}\boldsymbol{x}(t) = \boldsymbol{f}(t), \tag{2.12}$$

where $\boldsymbol{f}(t)$ is the vector of excitation forces, and $\boldsymbol{C}$ is the damping matrix of the system.

In the frequency domain, *i.e.,* by assuming an oscillatory motion of the system of the form $\boldsymbol{x}(t) = \boldsymbol{X}e^{j\omega t}$, Equation 2.12 becomes

$$(-\omega^2\boldsymbol{M} + i\omega\boldsymbol{C} + \boldsymbol{K})\boldsymbol{X}(\omega) = \boldsymbol{F}(\omega), \tag{2.13}$$

and the transfer matrix takes the form of a matrix of FRFs

$$\boldsymbol{H}(\omega) = (-\omega^2\boldsymbol{M} + i\omega\boldsymbol{C} + \boldsymbol{K})^{-1}, \tag{2.14}$$

where an element $H_{lm}(\omega)$ of the FRF matrix corresponds to the frequency response at coordinate n°l to a single excitation of unit amplitude at coordinate n°m [17].

To illustrate the principles of the forced response of a linear damped system, the case of a SDOF system is considered. This choice is made for the sake of simplicity in the theoretical development; however, the same principles are applicable to both SDOF and MDOF systems.

The dynamics of an SDOF mass-spring-damper system is easily derived from the MDOF counterpart (Equation 2.12)

$$m\ddot{x}(t) + c\dot{x}(t) + kx(t) = f(t). \tag{2.15}$$

This equation can be normalised by the mass and expressed in the following form

$$\ddot{x}(t) + 2\zeta\omega_0\dot{x}(t) + \omega_0^2 x(t) = f(t)/m, \tag{2.16}$$

where

$$\zeta = \frac{c}{2m\omega_0} \quad \text{and} \quad \omega_d = \omega_0\sqrt{1-\zeta^2}. \tag{2.17}$$

Equation 2.17 defines the *damping ratio* ζ and the *damped natural frequency* ω_d of the system.

By expressing Equation 2.15 in the frequency domain, it comes

$$(-\omega^2 m + i\omega c + k)X(\omega) = F(\omega). \tag{2.18}$$

The FRF of the linear system is then mathematically expressed as

$$H(\omega) = \frac{X(\omega)}{F(\omega)} = \frac{1}{k}\frac{1}{1 - \omega^2/\omega_0^2 + 2i\zeta\omega/\omega_0}, \tag{2.19}$$

where the term $1/k$ represents the static response of the system, and the remaining term is known as the *dynamic amplification factor*.

The FRF provides a quantitative measurement of the magnitude and phase of the output of the system as a function of the input force, *i.e.*, it offers quantitative insight into the amplification or attenuation of the system's response amplitude relative to the excitation force, as well as the phase difference between input and output. It is a constant property in linear systems and is widely used in vibration testing.

The amplitude of the FRF increases significantly when the excitation frequency ω lies in the vicinity of the system's natural frequency ω_0, a phenomenon commonly referred to as resonance. Two types of resonance are typically distinguished: *amplitude resonance*, which occurs when the amplitude of the FRF reaches its maximum, and *phase resonance*, characterised by a quadrature phase lag, *i.e.,* a phase difference of $\pi/2$ rad, between the excitation force and the system's response. In undamped systems, amplitude and phase resonances coincide; however, in the presence of damping, the disparity between these two resonance frequencies increases with the damping.

In the case of lightly damped structures with well-separated modes, the FRF data can be used to compute the mode shapes of the structure using, for instance, the polyreference least-squares complex frequency-domain method [22].

Figure 2.1 illustrates the typical appearance of an FRF curve for an SDOF mass–spring–damper system. The influence of the damping ratio of the system on its dynamics is demonstrated. As observed in Figure 2.1a, the amplitude of the resonance peak of the FRF decreases as the damping ratio increases. For a damping ratio of 95%, it is observed that the overshoot disappears. Furthermore, it is evident that amplitude resonance occurs at lower frequencies for systems with higher damping, thereby illustrating the distinction between the natural frequency and the damped natural frequency defined in Equation 2.17. Finally, it is worth noting that, in damped systems, amplitude resonance no longer corresponds to a phase lag of $-\pi/2$ rad between the system's response and the excitation signal, but it appears at phase lags greater than $-\pi/2$ rad.

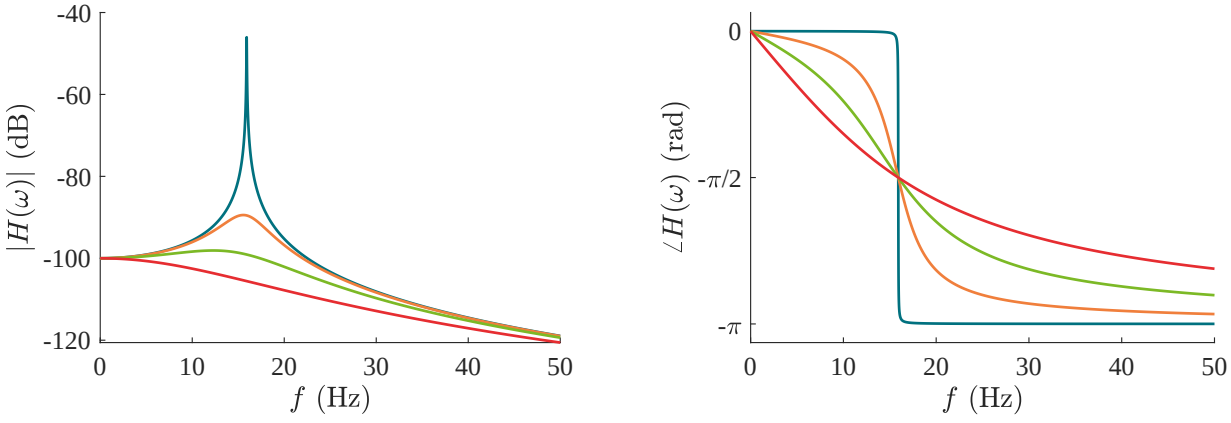

(a) Amplitude of the FRFs.

(b) Phase of the FRFs.

Figure 2.1: Bode plots of the FRFs of a mass-spring-damper SDOF system (Equation 2.19) for various damping ratios: ζ = 0.1% (—), ζ = 15% (—), ζ = 45% (—) and ζ = 95% (—) and a natural frequency ω_0 = 15.91 Hz.

2.2 Nonlinear systems

In cases where systems exhibit, for instance, excessively large deformations, or when nonlinearities arise from material properties or contact conditions, the linearisation of their dynamics is no longer valid. As a consequence, the dynamics of the whole nonlinear system must be investigated.

The study of nonlinear dynamical systems, encompassing both theoretical and experimental approaches, has constituted an extensive research field for over a century. It was first introduced by Poincaré in the nineteenth century, who, at the time, provided a mathematical formulation of the dynamics of self-oscillating systems [10]. Since then, considerable research has been conducted on nonlinear dynamics, accompanied by the development of numerical and experimental methods aimed at investigating the often unpredictable behaviour of nonlinear systems.

2.2.1 Single-degree-of-freedom conservative systems

This section aims to present the fundamental principles underlying nonlinear systems. A conservative *Duffing oscillator* is employed as an introductory example to illustrate the essential characteristics of such systems. The Duffing oscillator, which consists of a classical mass-spring-damper system where a cubic stiffness term is added, is among the most frequently studied nonlinear systems in the literature [23, 24].

The following equation describes the dynamics of a conservative SDOF Duffing oscillator, normalised with respect to the system mass

$$\ddot{x}(t) + \omega_0^2 x(t) + \alpha_3 x(t)^3 = 0, \tag{2.20}$$

where α_3 is the cubic stiffness coefficient. The system has the following initial conditions

$$x_0(0) = x_0 \text{ and } \dot{x}_0(0) = 0. \tag{2.21}$$

The exact analytical solution of this equation is not trivial. The details of the demonstration can be retrieved in [20].

The solution of Equation 2.20 is expressed as a function of an elliptic cosine

$$x(t) = x_0 \mathrm{cn}(\Omega t|\gamma) \quad \text{with} \quad \Omega = \sqrt{\omega_0^2 + \alpha_3 x_0^2} \quad \text{and} \quad \gamma = \frac{\alpha_3 x_0^2}{2\Omega^2}. \tag{2.22}$$

Important conclusions can be drawn from Equation 2.22. Firstly, the form of the exact solution indicates that the response no longer exhibits purely harmonic motion. Secondly, the frequency of vibration depends not only on the system stiffness and mass, as in the linear case, but also on the cubic stiffness coefficient and on the initial displacement. In such cases, the systems are said to be *frequency-amplitude dependent*. These observations are of significant importance, as they highlight the fundamental principles on the dynamics of nonlinear systems. From these observations, it can be concluded that the response of a Duffing oscillator varies quantitatively depending on the initial displacement and the magnitude of the nonlinear stiffness term. In such conditions, the superposition principle can no longer be applied.

Figure 2.2 compares the response of a conservative SDOF linear system and a conservative SDOF Duffing oscillator. As discussed in the previous section, the linear system exhibits harmonic motion at its natural frequency, irrespective of its initial conditions, the latter only influencing the amplitude

of the vibratory motion. On the other hand, Figure 2.2b demonstrates a different behaviour. While the amplitude of the system's response depends on its initial displacement, the frequency of oscillation is also influenced by it, as well as by the cubic stiffness coefficient. In such cases, the system no longer exhibits a purely harmonic motion.

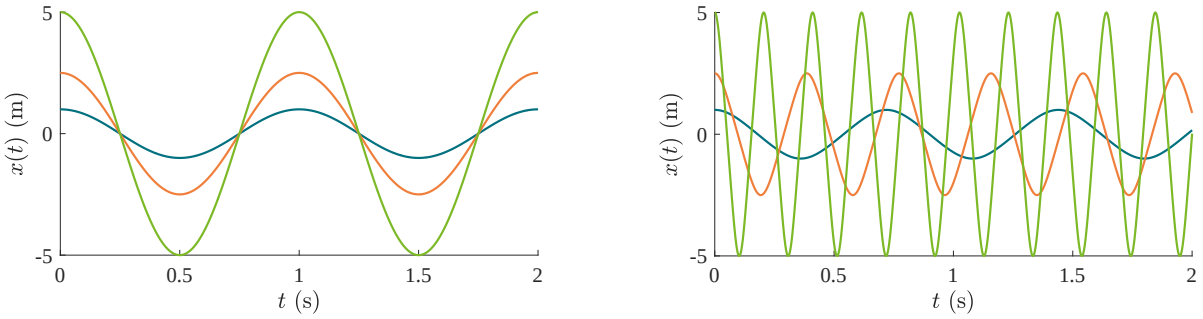

(a) Response of the linear system.

(b) Response of the Duffing system.

Figure 2.2: Comparison of the response variation of conservative SDOF linear (Equation 2.1) and nonlinear (Equation 2.20) systems having a natural frequency $\omega_0 = 1$ Hz, a nonlinear coefficient $\alpha_3 = 50$ N/(kg m^3) and various initial conditions. In both cases, $\dot{x}_0 = 0$ m/s for the three curves, and $x_0 = 1$ m (—), $x_0 = 2.5$ m (—) and $x_0 = 5$ m (—).

Figure 2.3 illustrates another characteristic of nonlinear systems, namely the dependence of the system's oscillation frequency on the nonlinear stiffness coefficient. As expected from physical reasoning, the frequency of oscillation increases with the magnitude of the nonlinear stiffness coefficient, such that the response of the nonlinear system is no longer purely periodic.

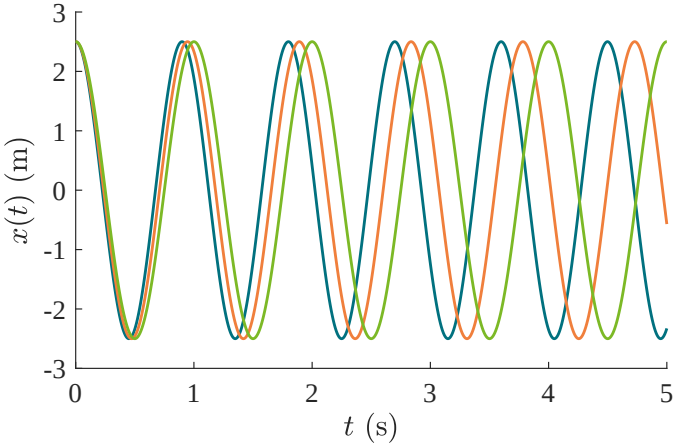

Figure 2.3: Free response of the conservative SDOF Duffing oscillator (Equation 2.20) of natural frequency $\omega_0 = 1$ Hz for various nonlinear stiffness coefficients: $\alpha_3 = 2$ N/(kg m^3) (—), $\alpha_3 = 1$ N/(kg m^3) (—) and $\alpha_3 = 0$ N/(kg m^3) (—). The initial conditions are kept constant between the various responses and are set to $x_0 = 2.5$ m and $\dot{x}_0 = 0$ m/s.

It is interesting to mention that the Jacobi elliptic cosine function is represented in a Fourier expansion by an infinite number of harmonics [20], which can be observed by computing the Fast Fourier Transform (FFT) of the response of the Duffing oscillator. Figure 2.4 illustrates the harmonics creation of the nonlinear system, as three resonance peaks are visible in the Fourier Transform of the free response of the undamped Duffing oscillator defined in Equation 2.20.

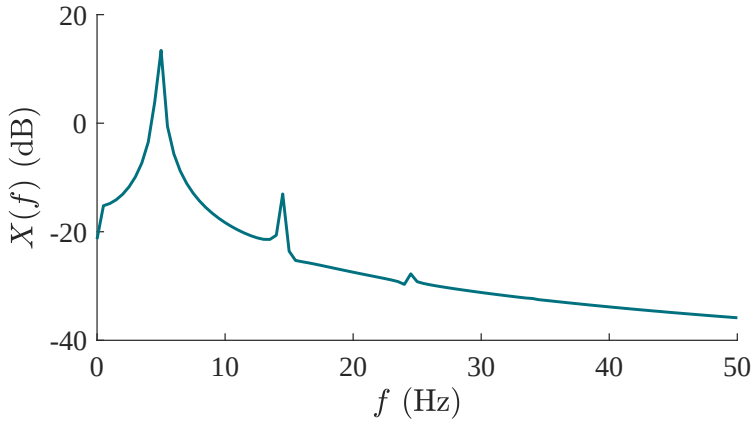

Figure 2.4: Computation of the FFT of the free response of the conservative SDOF Duffing oscillator (Equation 2.20) of natural frequency $\omega_0 = 1$ Hz, defined with the following initial conditions $x_0 = 5$ m and $\dot{x}_0 = 0$ m/s. The nonlinear coefficient α_3 is set to 50 N/(kg m^3).

This observation confirms that nonlinear systems do not exhibit purely harmonic motion, as they tend to generate higher-order harmonics, a phenomenon not observed in linear systems.

2.2.2 Nonlinear normal modes

NNMs are the nonlinear counterpart of LNMs arising in linear systems. NNMs were first introduced by Rosenberg in the 1960s [25]. Since then, NNMs have attracted increasing attention and were investigated extensively in the literature, notably by Shaw and Pierre [26].

Within the field, there exist mainly two definitions of the NNMs [21], one introduced by Rosenberg [25], and a second by Shaw and Pierre [26].

Rosenberg's definition is considered as an extension of the linear approach to nonlinear systems. He defined an NNM as a synchronous oscillation of the undamped and unforced system, where all points of the system reach their maxima, minima, or pass through zero simultaneously. However, Rosenberg's approach, while elegant and insightful, remains relatively restrictive in its applicability. Specifically, it requires multi-point, multi-harmonic forcing on the structure, which is not commonly used in practice [27]. Rosenberg's definition, as it stands, cannot be extended to non-conservative systems. Furthermore, in the presence of internal resonances, where multiple NNMs interact, some coordinates on the structure might have a dominant frequency component that differs from those of other coordinates. In such cases, the requirement for a synchronous motion is no longer satisfied [21, 25].

As a consequence, Kerschen *et al.* [21] proposed a revised definition of NNMs introduced by Rosenberg. This formulation extends the original definition by characterising an NNM as a periodic motion of a nonlinear system, thereby eliminating the requirement for synchronous motion and enabling the inclusion of internal resonances within the NNM framework.

Shaw and Pierre, on the other hand, proposed a definition of an NNM that is an extension of the form of the NNM presented by Rosenberg, and which is extendable to damped systems. In their work, Shaw and Pierre defined an NNM as a two-dimensional invariant manifold in phase space. Such a manifold is invariant under the flow, *i.e.,* orbits that start out in the manifold remain in it for all time, which extends the invariance property of LNMs to nonlinear systems [21, 26]. This second

definition is less favoured in the experimental approach, because of the practical complications it involves [28].

2.2.3 Multiple-degree-of-freedom forced and damped systems

The general form of equations of motion for a forced and damped MDOF nonlinear system is given by

$$\boldsymbol{M}\ddot{\boldsymbol{x}}(t) + \boldsymbol{C}\dot{\boldsymbol{x}}(t) + \boldsymbol{K}\boldsymbol{x}(t) + \boldsymbol{f}_{\mathrm{nl}}(\boldsymbol{x}(t), \dot{\boldsymbol{x}}(t)) = \boldsymbol{f}_{\mathrm{exc}}(\omega, t), \tag{2.23}$$

where $\boldsymbol{f}_{\mathrm{nl}}(\boldsymbol{x}(t), \dot{\boldsymbol{x}}(t))$ is the vector of nonlinear forces and $\boldsymbol{f}_{\mathrm{exc}}(\omega, t)$ is the vector of excitation forces.

Obtaining the exact solution of such dynamical systems is far from being the norm in nonlinear dynamics. Consequently, the computation of the dynamics of nonlinear systems typically relies on approximation methods, which have become the standard approach in such analyses. The following discussion briefly presents several commonly employed methods.

One widely employed approach for identifying periodic solutions of nonlinear systems is the harmonic balance method (HBM). The HBM is a numerical method which employs Fourier basis functions and corresponding weighting functions as an ansatz for the solution [29]. The rationale for employing Fourier series lies in the fact that a reasonably accurate approximation of the steady-state response of a system subjected to a harmonic excitation can often be obtained by retaining only the first few harmonics of the series. However, this method is not suitable for non-periodic systems or non-smooth nonlinearities such as Coulomb friction [20]. Moreover, ensuring sufficient accuracy requires either prior knowledge of the solution or the inclusion of a sufficient number of harmonics in the Fourier series [19].

Another commonly used approach is the shooting method, which iteratively determines the initial conditions that lead to a periodic motion of the system. A root-finding algorithm, such as Newton-Raphson, is employed to refine the guess for the initial conditions. While this method yields a single solution, continuation techniques, such as sequential or pseudo-arclength continuation, can be used to trace complete solution branches [20].

Finally, Nayfeh and Mook [19] presented the method of multiple scales to compute an approximate solution of nonlinear oscillations by considering different time scales in the approximated response.

2.3 Characteristics of nonlinear systems

As reviewed in Section 2.2, nonlinear systems exhibit behaviours that are unique to their nature. This section presents several properties and characteristics that are essential in the analysis of such systems. More precisely, the concept of backbone curve, NFRC, bifurcation and secondary resonance are presented.

2.3.1 Backbone curve

One of the most well-known characteristics of nonlinear systems is the dependence of their frequency of oscillation on the amplitude of motion. This property, also known as frequency-energy, or frequency-amplitude dependence, is commonly illustrated using a backbone curve. This curve, which represents the amplitude of the response of a nonlinear system at resonance as a function of its frequency of oscillation, is commonly used to characterise nonlinear systems.

The concept of the backbone curve was introduced in the 1960s by Rosenberg, alongside his definition of NNM [25, 30]. In his text, Rosenberg presented the backbone as an indicator of how the natural frequency of the conservative system varied with the amplitude of its response (and its initial conditions). At that time, the backbone curve was closely linked to the NNM. Subsequently, Nayfeh *et al.* [19] introduced a second definition of the backbone curve, corresponding to the curve tracing the loci of the peak amplitudes of the NFRCs. In such a definition, the backbone is associated to non-conservative systems. A third definition arises from the phase resonance condition [31], whereby the backbone curve corresponds to the response amplitude when phase quadrature between the system response and the excitation force is enforced. This last definition also pertains to non-conservative systems, and will be considered in this Master's thesis. An illustration of a backbone curve can be found in Figure 2.5a.

2.3.2 Nonlinear frequency response curve

It is common practice to characterise nonlinear systems, analogously to their linear counterparts, using NFRCs. However, an NFRC and an FRF do not have the same properties. As its name suggests, an NFRC is not a function but a *curve*, meaning that there might be multiple coexisting solutions associated with a given excitation frequency. Furthermore, as will be detailed below, the curve shape of the NFRC depends heavily on the forcing applied to the system.

To introduce the principle of NFRC, consider an SDOF damped and forced Duffing oscillator, whose motion is described by the following equation

$$\ddot{x}(t) + 2\zeta\omega_0\dot{x} + \omega_0^2 x(t) + \alpha_3 x(t)^3 = F\cos(\omega t), \tag{2.24}$$

where F is a scalar representing the forcing amplitude of the excitation force, and ω is the frequency of excitation.

NFRCs were computed for an SDOF damped Duffing oscillator subjected to varying amplitudes of excitation. The resulting curves are presented in Figure 2.5a.

As shown, the resonance peak of the NFRC shifts towards higher frequencies as the amplitude of excitation increases. This phenomenon, which is indicative of nonlinear stiffness effects, reflects the characteristic *hardening* behaviour of the Duffing oscillator. This response is consistent with Equation 2.24, wherein the presence of a positive cubic stiffness term leads to an effective increase in system stiffness. The contribution of this nonlinear term scales cubically with the system's displacement. Consequently, at low levels of excitation, where the structural response remains minimal, the influence of the nonlinear term is negligible and the system exhibits predominantly linear behaviour. In contrast, as the amplitude of excitation increases, and with it the displacement, the contribution of the nonlinear term becomes increasingly significant, thereby amplifying the system's nonlinear characteristics.

As previously discussed, the term *curve* is used in reference to the NFRC rather than *function*, owing to the potential existence of multiple solutions in nonlinear systems. This multiplicity of solutions can be observed in Figure 2.5a. For instance, in the case of the 25 N excitation curve, three distinct response amplitudes of the NFRC correspond to a frequency of 17 Hz: one at $x = 0.02$ m, another at $x = 0.018$ m, and a third one at $x = 0.0018$ m. In such cases, the lower part of the NFRC peak, which is highlighted by a dashed line in Figure 2.5a, is an *unstable* part. When the system resides in an unstable solution, small perturbations lead it to converge towards an alternative stable solution.

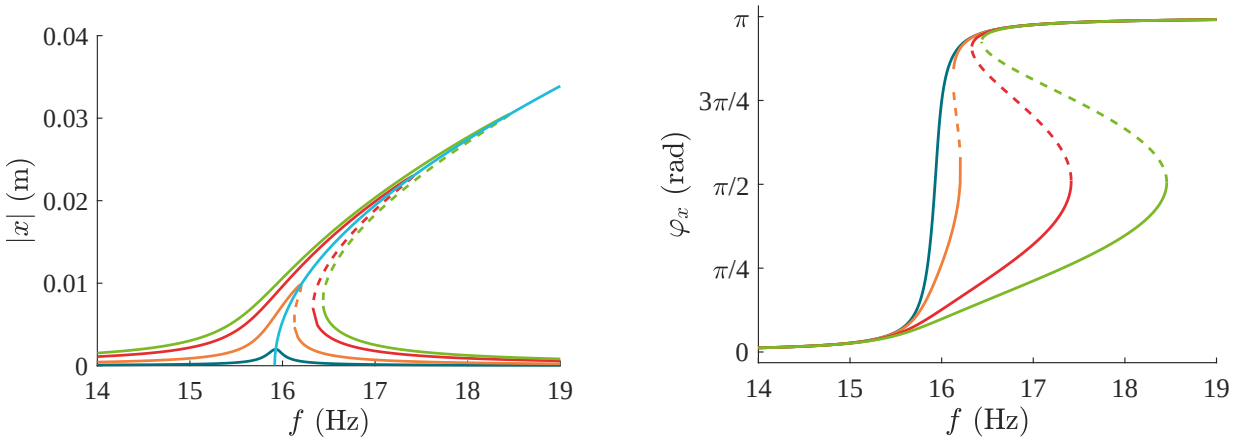

(a) NFRCs and backbone curve.

(b) Phase of the response.

Figure 2.5: Response of the damped Duffing oscillator defined in Equation 2.24 for the following parameters: $\omega_0 = 15.91$ Hz, $\zeta = 0.5$ % and $\alpha_3 = 5 \times 10^6$ N/(kg m^3). Four forcing levels were used: 2 N (—), 10 N (—), 25 N (—) and 35 N (—). The dashed lines denote the unstable parts. The computations were carried out using the HBM implemented within the NI2D software.

In nonlinear systems, the steady-state response is highly sensitive to initial conditions, which dictate the specific branch of the solution to which the system will converge.

2.3.3 Bifurcation

When performing classical sine sweep tests, which consist of gradually and continuously increasing the excitation frequency while maintaining a constant excitation amplitude, nonlinear systems exhibiting unstable regions typically undergo abrupt transitions, or jumps, from one stable state to another. Such jump phenomena are hallmark features of nonlinear systems. However, characterising the unstable regions of nonlinear systems remains essential, as changes in stability can significantly influence the system's dynamics through the occurrence of *bifurcations*. One of the most common types of bifurcations is *fold* bifurcation, which is located near resonances. Fold bifurcations are observed at the turning point of the NFRCs in Figure 2.5a, they delimit the unstable regions. Other types of bifurcations, such as *branch-point* bifurcations or *Neimark-Sacker* bifurcations also exist. However, a comprehensive review of these bifurcations and their methods of computation falls outside the scope of this thesis. The reader can refer to [32, 33] for bifurcation analysis of nonlinear systems.

2.3.4 Secondary resonance

This work focuses on identifying NFRCs and backbone curves associated with fundamental resonances. Nevertheless, it is important to acknowledge that nonlinear systems frequently exhibit additional forms of resonances, referred to as *superharmonic*, *subharmonic* and *ultra-subharmonic* resonances.

As previously noted in this chapter, nonlinear systems are characterised by the generation of harmonics. This property can be exploited by representing the NFRCs of the system when computed using the HBM formulated with multiple harmonics.

Figure 2.6 displays both superharmonic and subharmonic resonances of a Duffing oscillator. Let us note the frequency $k\omega_0/\nu$, where k and ν are incommensurate positive integers. Following this definition, the fundamental resonance happens when $k = \nu = 1$. The superharmonic resonances happen at frequencies for which $\nu = 1, k > 1$, whereas subharmonic resonances are characterised by frequencies for which $k = 1, \nu > 1$. The ultra-subharmonic resonances happen at frequencies for which $k \neq \nu \neq 1$. The superharmonic (subharmonic) resonances are located before (after) the fundamental resonance, and can be perceived at frequencies lower (higher) than 1 in Figure 2.6. The location of the ultra-subharmonic on the bifurcation diagram depends on the harmonics, if $k > \nu$, the ultra-subharmonic is located before the fundamental resonance, and to the right if $k < \nu$.

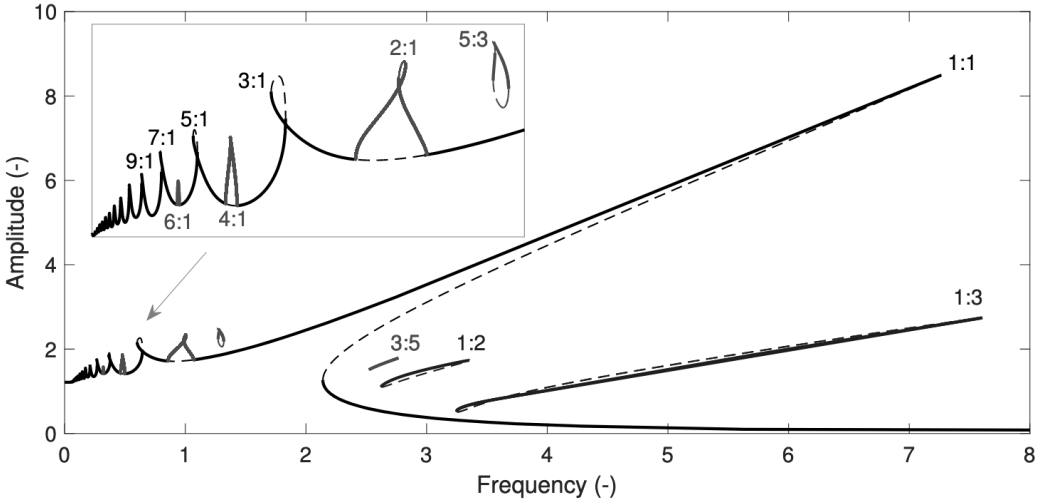

Figure 2.6: Bifurcation diagram of a Duffing oscillator, displaying the fundamental resonance, as well as superharmonic, subharmonic and ultra-subharmonic resonances [10].

Subharmonic responses in nonlinear systems often manifest as detached solution branches known as *isolas* or *isolated response curves*. These isolated branches of periodic solutions are not retrieved trivially. Hirai and Sawai [34] proposed a general criterion for the existence conditions of such jump phenomena in nonlinear systems, Woiwode and Krack [31] investigated the experimental uncovering of isolas using backbone tracking implemented with a PLL method. Additional information on isolas formation and tracking can be found in [35, 36].

2.4 Conclusion

This chapter presented the fundamentals of linear and nonlinear vibrating systems, emphasising the key distinctions between the linear and nonlinear paradigms.

The linear paradigm was shown to offer substantial simplifications in both the formulation and the resolution of system dynamics. It was demonstrated that, in conservative linear systems, the amplitude of the response depends solely on the initial conditions, while the system consistently oscillates at its fundamental frequency, which is determined by its stiffness and damping properties. The mode shapes of linear systems were then presented. Also known as linear normal modes, these deformations are a useful tool in modal analysis of systems, as they provide information on the system deformation and behaviour under resonance conditions.

Nonlinear systems, on the other hand, exhibit more complex dynamics. The introduction of such systems began with the derivation of the exact solution of a conservative SDOF Duffing oscillator. The analysis of this system concluded with the observation that the frequency of oscillation of the free response of the undamped Duffing oscillator depended not only on its natural frequency, but also on its initial conditions. In such cases, the response of the system does not follow a purely periodic motion, as opposed to linear systems. Moreover, due to the inherent characteristics of nonlinear dynamics, such systems are observed to generate harmonic components.

The reader was also introduced to NNMs, which are the nonlinear counterpart of LNMs. Although these two motions describe the structural deformation at resonance, they exhibit distinct properties. For nonlinear systems, it was observed that NNMs may exhibit unstable regions, are energy-dependent and may interact, thereby invalidating the properties of modal superposition and orthogonality derived in the linear paradigm.

This chapter concluded with the introduction of two essential properties of nonlinear systems, namely the NFRC and the backbone curve. The NFRCs were the support for the presentation of multiple features of nonlinear systems, such as stable and unstable regions, jump phenomena observed in classical sine sweep analysis performed on nonlinear systems, and the concept of superharmonic and subharmonic resonances, the latter of which often take the form of isolas. It was observed that the definition of the backbone curve can be linked to conservative systems and non-conservative systems. In the latter case, the backbone was found to approximate the loci of the NFRCs of nonlinear systems.

3 Introduction to control systems

A comprehensive review of the fundamental principles of control theory is essential before analysing the algorithm of the PLL. Feedback control has always been a part of our everyday lives. Its introduction is thought to date from antiquity, where water clocks used feedback control to keep track of time [37]. Nowadays, feedback control is omnipresent in aerospace engineering systems. For instance, they are used in satellite attitude control, where the disturbances have to be diminished to ensure precise attitude regulation [38], as well as in the new generation of gravitational wave observatories, where active isolation is required to reduce all sources of noise, and particularly seismic noise [39].

The main idea behind feedback control is that the system's output is continuously monitored and used in a *feedback loop*. This feedback loop allows the controller to adjust its output to bring the system to a desired state autonomously, while still requiring adequate tuning of the controller gains. In this chapter, the focus will be on *proportional-integral-derivative* (PID) controllers, whose principle was introduced in 1911 by Sperry [40].

This chapter introduces fundamental concepts of control theory, defining the differences between open-loop and closed-loop systems. It then focuses on the definition of PID control, examining the influence of gain parameters and their tuning on system performance.

3.1 Open-loop and closed-loop control systems

When designing control systems, one of the primary considerations is whether a feedback loop will be incorporated within the system. If no feedback is present, the system is classified as an *open-loop* system (Figure 3.1a). Conversely, if the controller includes a feedback mechanism, the system is referred to as a *closed-loop* one (Figure 3.1b).

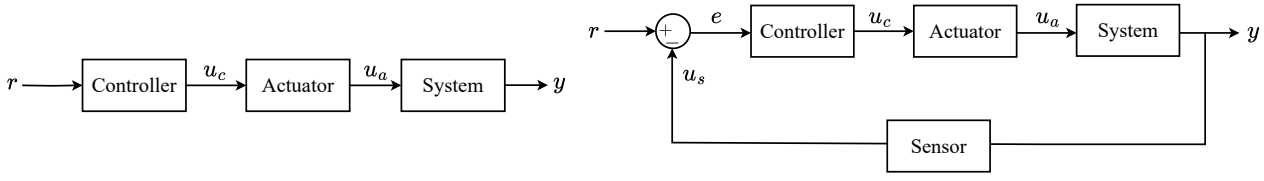

(a) Block diagram of an open-loop control.

(b) Block diagram of a closed-loop control.

Figure 3.1: Presentation of open-loop and closed-loop control systems.

The structure of control systems are often described using block diagrams. This type of representation highlights the causal links between the various components of the system, and their inputs

and outputs. In Figure 3.1, the controller, the actuator, the sensor and the system are represented by black boxes, which take an input, perform an operation on this input, and return the output.

In an open-loop system, the reference input r is processed by the controller, which generates an appropriate control signal u_c for the system. This control signal is fed to an actuator that translates it into an actuating signal u_a. The system then responds to this signal, and its output state is referred to as y. In open-loop control systems, the absence of a feedback loop prevents the controller from automatically adapting its control signal to the system state, necessitating external intervention for system calibration.

On the other hand, in a closed-loop control scheme, the output of the system y is measured by a sensor, and fed back to the input of the controller. To do so, the sensor signal u_s, which is equal to the system state y in a theoretical ideal system, is compared to the reference value. An error signal e is derived from this difference and is used as an input of the controller. Thanks to the addition of a negative feedback loop, the controller adapts its output automatically to the state of the system.

In real experimental conditions, sensor measurements may be affected by noise, and the system may be influenced by external disturbances. For the sake of clarity, these disruptive signals are omitted in the block diagrams.

Despite the structural differences between open-loop and closed-loop control systems, they both share a common goal, which is to bring the controlled system to a reference state. However, the feedback loop has the advantage to reduce the sensitivity of the system to external disturbances or to modifications of the system itself. Feedback control systems also have the possibility to modify the dynamics of a system, for example, by implementing active isolation to enhance its damping, or to stabilise unstable or marginally stable system conditions [41].

To illustrate the difference between open-loop and closed-loop control systems, one could imagine the management of an aircraft speed through throttle control. In a simple open-loop system, the pilot manually sets the throttle to a desired power level. To achieve a desired aircraft speed, the skilled pilot observes the aircraft's flight characteristics and manually adjusts the throttle accordingly. In a closed-loop system, the pilot would set a desired aircraft speed, and the throttle would automatically adapt its engine power depending on various parameters, such as the current aircraft speed, altitude, pitch angle, wind strength and direction.

In general, closed-loop systems are more often considered in engineering systems, as they offer more precise, situation-specific control when properly calibrated. Controller tuning will be addressed in the following sections.

3.2 Fundamental principles of feedback control systems

As detailed in [42], a closed-loop control system is expected to meet the following criteria:

- *Stability*: the controlled system has to be stable.
- *Accuracy*: the controlled system must track the reference state as accurately as possible.
- *Active isolation*: the controlled system's output must be as independent as possible from external disturbances.

Concerning the stability requirement, there are two possible scenarios. The first one is that the system is initially unstable, in that case the feedback control must render it stable. The second case

is that the system is initially stable, but the addition of feedback control makes it unstable. In both scenarios, the addition of feedback control has to lead to a stable output of the system.

It is common practice to evaluate the robustness and efficiency of a controller by analysing the system response to a step excitation, which entails transitioning the system input from zero to a constant value. In particular, it is customary to analyse system *rise time*, *settling time*, *overshoot* and *steady-state error*. These variables are all presented in Figure 3.2, which represents a typical curve of a step response of a second-order system.

The rise time t_r is the time the system takes to approximately reach the new set point. It is often referred to as the time the system takes to go from 10% to 90% of the set point. In applications that require a swift response of the system, the rise time is expected to be sufficiently low.

The overshoot, associated with a time t_p, quantifies the maximum amplitude the system reaches before attaining its final value. It is often expressed as a quotient, where the maximal value is divided by the final value of the system. The overshoot is directly related to the system damping ratio, and its amplitude decreases as the damping ratio of the system increases. The overshoot does not exist for critically damped ($\zeta = 1$) and overdamped ($\zeta > 1$) systems.

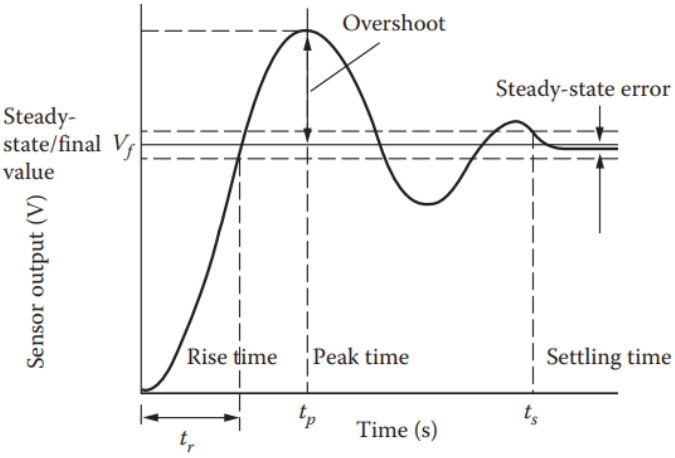

Figure 3.2: Time-domain specifications of the step response of a controlled system. [43]

The settling time t_s is a characteristic of the transient part of the system's response. It corresponds to the time the system takes to approximately reach a steady-state. It is commonly required to obtain a fast and efficient controller.

Finally, the steady-state error is introduced. The steady-state error is measured when the system has reached a steady-state, *i.e.*, when the transient part of the response has faded out. It corresponds to the error that exists between the desired state and the actual system state. For applications that require high-level precision (*e.g.*,, satellite attitude control), minimal steady-state error should be obtained, making it a key criterion for the controller design.

3.3 PID control and gain adjustments

A PID controller is nowadays the most commonly used type of feedback control system [44]. It consists of three primary components: a proportional gain, an integral gain, and a derivative gain. While this thesis primarily focuses on proportional-integral (PI) control, the derivative gain will be introduced for the sake of completeness.

The following presentation of PID feedback is based on [41, 42, 44]. In the case of a PID, the action of the controller is expressed by the following equation

$$u_c(t) = k_p e(t) + k_i \int_0^t e(\tau) d\tau + k_d \frac{de(t)}{dt}, \tag{3.1}$$

where $u_c(t)$ is the signal output by the controller, e is the error (see Figure 3.1b), k_p is the proportional gain, k_i is the integral gain, and k_d is the derivative gain. The role of each of these three gains is detailed in the following subsections.

3.3.1 Proportional gain

In classical, rudimentary, on-off control systems, switching from one state to another, *i.e.*, from on to off or vice versa, causes oscillations in the system. This behaviour is observed because the system overreacts, as a small change in the error makes the actuated variable switch across its full range. The introduction of a proportional constant k_p is used to dampen this effect. In proportional control, the controller output is directly proportional to the control error

$$u_c(t) = k_p e(t). \tag{3.2}$$

While the addition of proportional gain mitigates the high oscillations present in on-off control, it causes the system to settle at a value different from the reference, resulting in a steady-state error. This effect is demonstrated in Equation 3.2, where it is clear that, for the system to reach the reference state, the error $e(t)$ must be zero, indicating that the controller would not be functioning. Consequently, controller start-up is associated with a non-zero static error.

The closed-loop system presented in Figure 3.1b can be translated in the Laplace domain

$$\left.\begin{array}{l} Ek_p = Y/G \\ R - Y = E \end{array}\right\} \Leftrightarrow Y/R = \frac{k_p G}{1 + k_p G}, \tag{3.3}$$

where G denotes the transfer function of the system. From Equation 3.3, it is easily observable that the state of the system tends to the reference state when $k_p \to \infty$. However, setting the proportional gain too high causes the controller to overshoot the set point, making the system oscillatory and, in some cases, unstable. Thus, the calibration of the proportional gain results from a compromise between the amplitude of the system's offset and its stability.

3.3.2 Integral gain

Integral gain was introduced to solve the problem of static error caused by the proportional gain. It is used to reduce the system offset and the steady-state output response to disturbances. With an integral gain, Equation 3.2 becomes

$$u_c(t) = k_p e(t) + k_i \int_0^t e(\tau) d\tau, \tag{3.4}$$

which defines a PI controller. The integral term in Equation 3.4 indicates that the controller no longer depends solely on the error at time t, but also on the system's error history. Equation 3.4 also shows that the controller is active, and sensitive to the error, as long as the error is non-null.

Whereas the action of a high integral gain allows attenuating the influence of disturbances, too high integral gain values can lead to an oscillatory behaviour of the system and a possible instability.

3.3.3 Derivative gain

The last term introduced in PID controllers is the derivative gain. The derivative term, often referred to as the *anticipatory* term, aims to improve closed-loop stability of the system, but also to reduce

the overshoot and to speed up the transient response. An estimation of the error is found by linearly extrapolating the error

$$e(t + T_d) \simeq e(t) + T_d \frac{de(t)}{dt}, \tag{3.5}$$

where T_d is the time for which the error is predicted.

Derivative controllers are almost never used alone. They have the advantage to be anticipatory, as the derivative term has information on the slope of the signal; thus, the output of the derivative term is dependent on the trend of the error signal. On the other side, the derivative term does not provide information on the desired final state, and for constant error, the derivative control is not active, requiring the addition of a proportional and/or integral control(s). Furthermore, derivative control tends to enhance noise, potentially resulting in system instability.

3.3.4 Summary of gain tuning for PID controllers

Figures 3.3 and 3.4 synthesise the action of the three parts of the PID controller, and the influence of their gains.

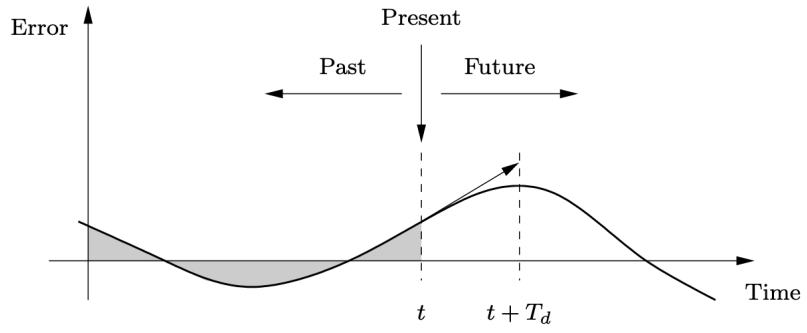

Figure 3.3: Action of the three terms of a PID controller. At time t, the output of the PID depends on the error at instant t, measured by the action of the proportional control, on the history of the error up to time t (grey area), controlled by the integral part, and on the prediction of the growth or decay of the error, computed by the derivative term. T_d represents the time for which the derivative of the error is estimated. [44]

PI controllers are often the chosen solution in the industry, as the combination of proportional and integral control gives a fast and precise response while avoiding the risk of system instability caused by noise amplification associated with derivative control. For the purposes of this thesis, a PI controller was selected for the PLL algorithm, in line with current practice.

Although studies were carried out to establish tuning methods for PI(D) controllers [45, 46] there is as yet no effective method for implementing controller gain tuning in the PLL algorithm, so that control gains are often determined empirically.

To more effectively illustrate the influence of gain parameters on system stability, a representative example is presented. Consider an SDOF linear mass–spring–damper system, whose dynamics are governed by Equation 2.15, and whose transfer function is provided in Equation 2.18.

Let us assume that the system is subjected to external excitations. A sensor, which measures the position of the mass, and an actuator, which applies a corrective force to restore the mass to a desired position, are integrated into a feedback control system governed by a PI controller.

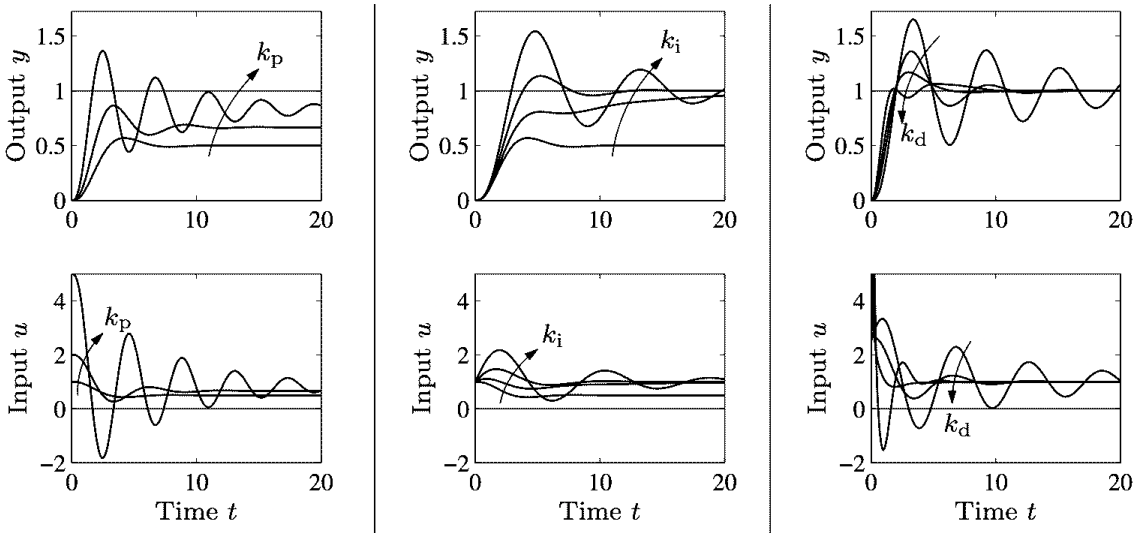

(a) Proportional control (b) PI control (c) PID control

Figure 3.4: Influence of the proportional, integral and derivative gains on the step response of a second order system controlled by (a) a proportional controller, (b) a PI controller, and (c) a PID controller. [44]

To tune the gains of the PI controller, the step response of the closed-loop system is computed using MATLAB `step` function, which computes the step response of the system, and the proportional and integral gains are tuned according to the response. Since the purpose of this example is to demonstrate the unstable behaviour of a poorly tuned system, several scenarios are considered. Initially, the off-control response is presented (Figure 3.5a). Subsequently, proportional and integral gains are adjusted to achieve a stable response (Figure 3.5b). The integral gain is then progressively increased to produce a marginally stable system (Figure 3.5c), and finally, an unstable one (Figure 3.5d).

As illustrated in Figure 3.5, improper tuning of the proportional and integral gains in a PI controller can result in system instability. In particular, an excessively high integral gain leads to a diverging response, while an overly large proportional gain increases the oscillatory nature of the system response—both of which are undesirable and should be avoided. It is also observed that the proportional gain helps stabilise the system, as the response of the system tuned with the same integral gain can lead to stable (Figure 3.5b) or unstable outcomes (Figure 3.5d) depending on the tuning of the proportional gain.

3.4 Conclusion

This chapter introduced the fundamentals of control theory, distinguishing open-loop systems, where the controller's input signal is independent of the system's output, and closed-loop systems, which incorporate a feedback path. Particular emphasis was placed on the PID controller, a widely used feedback control method. The chapter methodically presented each component of the PID controller, detailing the role and action of the proportional, integral, and derivative terms, and their collective influence on system performance. A simple example of an SDOF system was subsequently introduced to illustrate how improper tuning of the PI controller can lead to system instability, and to examine the resulting system behaviour in such cases. By understanding these core concepts and the detailed

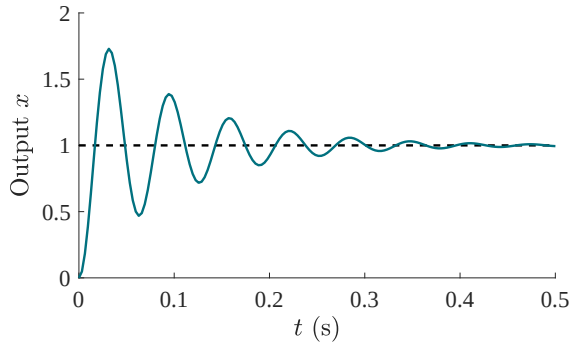

(a) Off-control system.

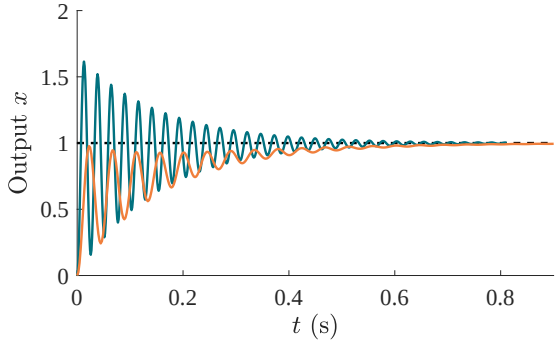

(b) Closed-loop system with $k_p = 5$ N/m and $k_i = 41$ N/(ms) (—), and $k_p = 1$ N/m and $k_i = 10$ N/(ms) (—). The response of the system is stable as it decays toward the aimed state.

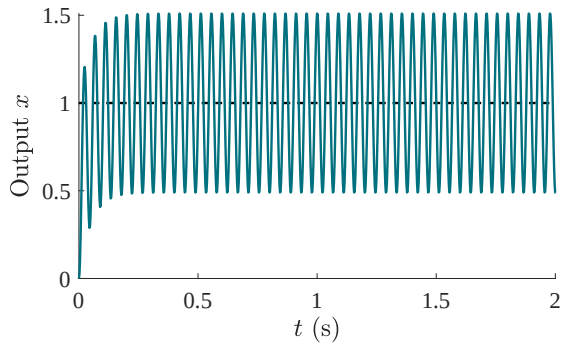

(c) Closed-loop system with $k_p = 1$ N/m and $k_i = 40$ N/(ms). The response of the system is marginally stable as bounded sustained oscillations are observed.

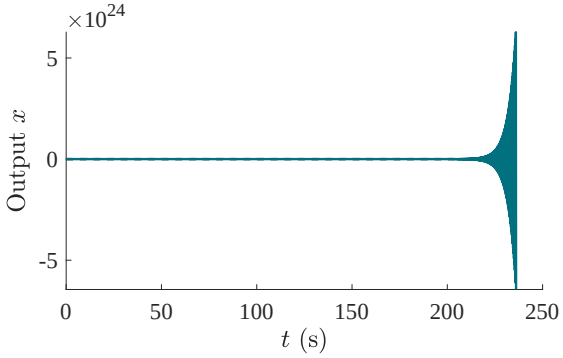

(d) Closed-loop system with $k_p = 1$ N/m and $k_i = 41$ N/(ms). The response of the system is unstable as it grows in an unbounded way.

Figure 3.5: Step response of an SDOF mass-spring-damper system for four cases: (a) off-control system and (b), (c), (d) closed-loop system with varying proportional and integral gains of the PI controller. The reference state (– –) is indicated.

time specifications of control systems, the foundation for PID gain tuning was established. Given the lack of a universally accepted approach for tuning PID gains to control nonlinear systems, the gain tuning process will be conducted through trial and error. Recent research on gain tuning in the context of PLL controllers, employed for the identification of NFRCs and backbone curves, will be presented in subsequent chapters.

4 Phase-locked loop algorithms

The PLL method belongs to the family of experimental continuation techniques employed in the analysis of nonlinear systems. Originally introduced in radio technology during the 1930s [28], the PLL method has only recently begun gaining interest within the field of experimental analysis of nonlinear dynamical systems, where a first experimental application of a PLL method to retrieve the NFRC of a Duffing oscillator was proposed by Mojrzisch *et al.* [47]. Peter *et al.* [28] then extended the concept to the experimental tracking of backbone curves. Since then, numerous studies have been carried out on the application of PLL, and more generally on experimental continuation methods in the field of nonlinear vibratory systems.

This chapter presents the state of the art of the experimental continuation methods in the field of nonlinear dynamics. The focus is then brought to the PLL technique, carefully detailing the principle of the method and the *adaptive filter* that is employed in the algorithm. This chapter concludes with a discussion of the parameters associated with the PLL method.

4.1 Introduction

The experimental analysis of nonlinear mechanical systems is a vast research area. Recent advances in this field have been thoroughly reviewed thoroughly reviewed by Raze *et al.* [10].

The latest developments in experimental continuation methods have been motivated by their simplicity, as they enable a model-free approach in the analysis of nonlinear systems, in contrast to more complex approaches such as nonlinear system identification methods. Sieber *et al.* [12] firstly pioneered experimental continuation methods by introducing the CBC method, which relies on a Newton-Raphson algorithm. Since then, less costly derivative-free methods have been developed. The PLL method is currently among the most commonly employed continuation techniques for the analysis of nonlinear systems, alongside other experimental continuation methods, such as the simplified-CBC (SCBC), and the arclength control-based continuation (ACBC) methods, which was introduced in [48].

Experimental continuation methods are generally based on a common working principle. The controlled system typically comprises the structure under test, an actuator (*e.g.*, a shaker), one or more sensors to measure the structural response, and a controller. In such methods, a desired state is indicated as an input of the controlled system. The controller, which receives the discrepancy between the measured state of the structure and the desired state, adjusts the actuation signal accordingly to drive the system towards the specified target.

An important property of experimental continuation techniques that must be enforced is the *non-invasiveness* of the controller. This property states that the equilibrium position of the plant, which

is typically composed of the structure under test, but also of the actuators and sensors, should not be modified by the presence of the controller. In the PLL method, non-invasiveness is naturally reached when the excitation frequency ω of the closed-loop system is stabilised [10].

The PLL method, as opposed to CBC methods, has the advantage of not relying on an iterative process, thereby offering the advantage of faster computation of NFRCs and backbone curves. Furthermore, the implementation of a PLL algorithm is comparatively straightforward and less complex than that of CBC methods, which require two principal resolution algorithms. However, the working principles of the PLL algorithm rely on the assumption that the phase lag exhibits a monotonic behaviour in the vicinity of the targeted resonance. Consequently, this method encounters difficulties when tracking non-monotonic phase behaviour, which may arise in the presence of secondary resonances such as isolas [31]. Moreover, this assumption restricts the applicability of the PLL algorithm, rendering it unsuitable for broadband NFRC testing, where non-monotonic phase behaviour is expected.

In this thesis, the investigation is centred on the fundamental resonances of nonlinear systems; as a consequence, the PLL algorithm is regarded as a particularly appropriate choice, as it provides a simple and efficient means of recovering the characteristic curves of nonlinear systems under real-time conditions.

4.2 Presentation of the algorithm

A PLL testing setup typically consists of a structure under test, a phase detector, a PI controller, a voltage-controlled oscillator (VCO), an actuator and a sensor. The working principles of the PLL are illustrated in Figure 4.1.

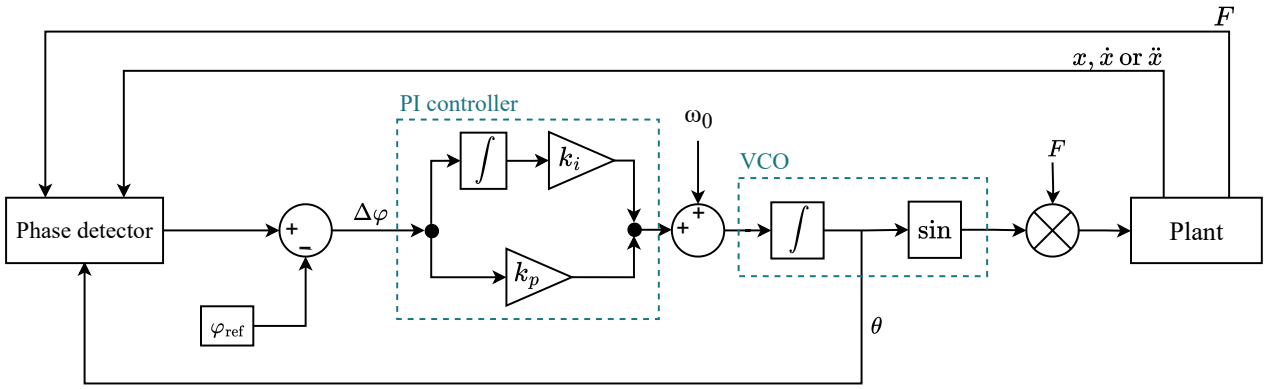

Figure 4.1: Schematic illustration of the PLL algorithm.

Specifically, within a PLL algorithm, a reference phase lag φ_{ref} is prescribed by the experimenter. This reference phase is compared with the phase lag observed between the system's response, measured using either the displacement, the velocity, or the acceleration of the structure at a chosen location, and the excitation force. The latter may correspond either to the voltage signal transmitted to the actuator or to the measured excitation force generated by the actuator, depending on practical considerations discussed in further detail in Section 6.4. The phase error $\Delta\varphi$ between the measured phase lag and the reference state is then used as an input of a PI controller, which adapts the excitation

frequency of the exciter $\omega(t)$ to reach the desired phase lag within the system

$$\omega(t) = \omega_0 + k_p \Delta\varphi(t) + k_i \int_0^t \Delta\varphi(\tau) d\tau. \tag{4.1}$$

Thus, the frequency of excitation is determined by an open-loop frequency ω_0, and the output of a PI controller, which is dependent on its integral and proportional gains, respectively k_i and k_p.

The derived frequency is sent to the VCO, which generates a signal oscillating at a frequency ω; this signal is subsequently used as the input to a sine function that serves to excite the structure. Finally, the sine excitation force is multiplied by a forcing amplitude F, which is determined by the experimenter. The excitation force is derived from

$$f(t) = F \sin\theta(t) = F \sin\left(\int_0^t \omega(\tau) d\tau\right). \tag{4.2}$$

In the PLL algorithm, the phase detector constitutes the principal component. In the implementation presented in this thesis, the adaptive filter was selected for this purpose. Further details concerning phase detectors, with a focus on adaptive filters are provided in the following section.

4.3 Adaptive filters

The phase detector is an essential component in a PLL algorithm as it enables the determination of the phase difference between two signals, namely the system's response and the excitation force, which is the driving factor of the PLL method.

A widely used method to perform a Fourier decomposition of a signal, though less common in PLL implementations, is the discrete Fourier transform (DFT). The DFT computes Fourier coefficients offline from recorded time signals by processing data over defined intervals. While effective, its offline nature limits real-time application, where online methods are preferred for continuous coefficients estimation [48].

Traditionally, phase detection in phase-controlled vibration testing employed *synchronous demodulation* (homodyne detection), which performs online Fourier decomposition by multiplying the signal with sine and cosine functions at the controller frequency and applying low-pass filters to extract amplitude and phase of the fundamental harmonic [13, 49, 50].

More recently, Abeloos *et al.* introduced adaptive filters within PLL algorithms, describing them as elements approximating signals using a time-varying Fourier series basis, enabling improved real-time analysis [51]. The main goal of the adaptive filter is to estimate the amplitude and phase lag of a signal by using a truncated Fourier expansion as a basis in which the signal is expressed. For a signal $x(t)$, the approximation $\tilde{x}(t)$ is obtained by

$$x(t) \simeq \boldsymbol{z}^T(t)\boldsymbol{q}(t) = z_0(t) + \sum_{k=1}^{n_H} \left(z_{sk}(t) \sin\left(k\theta(t)\right) + z_{ck}(t) \cos\left(k\theta(t)\right)\right) = \tilde{x}(t), \tag{4.3}$$

where $\boldsymbol{q}(t)$ is a vector that contains the n_H harmonic functions of the Fourier series, and the vector

$\boldsymbol{z}(t)$ includes the weight factors of each harmonic. These two vectors are developed as follows

$$\boldsymbol{q}(t) = \begin{bmatrix} 1 \\ \sin(\theta(t)) \\ \cos(\theta(t)) \\ \sin(2\theta(t)) \\ \vdots \\ \cos(n_H\theta(t)) \end{bmatrix} \quad \text{and} \quad \boldsymbol{z}(t) = \begin{bmatrix} z_0(t) \\ z_{s1}(t) \\ z_{c1}(t) \\ z_{s2}(t) \\ \vdots \\ z_{cn_H}(t) \end{bmatrix}. \tag{4.4}$$

When the error between the signal $x(t)$ and its approximation $\tilde{x}(t)$ is negligible and the weight coefficients $\boldsymbol{z}(t)$ have converged, Equation 4.3 represents a Fourier decomposition of $x(t)$, and $\boldsymbol{z}(t)$ approximates its Fourier coefficients.

The coefficients $\boldsymbol{z}(t)$ are updated using adaptive filtering with a least mean-squares (LMS) algorithm [52]. LMS algorithm enables the estimation of the Fourier coefficients at discrete time, and it is commonly employed to compute in real time conditions the amplitude and phase of acquired signals during vibration testing. LMS is well suited for use in a PLL method applied in nonlinear vibration testing, owing to its simplicity and low computational cost [49, 52].

At a time step t_i, the error between the signal and its estimate is given by

$$\varepsilon(t_i) = x(t_i) - \boldsymbol{z}^T(t_i)\boldsymbol{q}(t_i), \tag{4.5}$$

and the coefficients $\boldsymbol{z}(t_i)$ are updated according to the following law derived from the LMS algorithm

$$\boldsymbol{z}(t_{i+1}) = \boldsymbol{z}(t_i) + \mu \left(x(t_i) - \boldsymbol{z}^T(t_i)\boldsymbol{q}(t_i) \right) \boldsymbol{q}(t_i) \tag{4.6}$$

where μ is the step-size factor of the LMS method. In the following, μ will also be referred to as the adaptive filter gain, and $\tilde{\mu} = \mu f_s$ as the adaptive filter cut-off frequency, where f_s is the sampling frequency. This variable represents the rapidity of the filter to adapt to the measured signal. A stability analysis of this variable can be found in [48], and further discussions are presented in Sections 4.7 and 5.6.

From Equations 4.3- 4.6, it is possible to retrieve the amplitude and phase of the k-th harmonic of the measured signal, respectively, using the following relations

$$A_k = \sqrt{z_{sk}^2 + z_{ck}^2} \quad \text{and} \quad \varphi_k = \arctan(z_{ck}/z_{sk}). \tag{4.7}$$

The phase lag of the fundamental harmonic of the measured acceleration with respect to the applied excitation force is approximated by employing the adaptive filter method to both the response of the system and the excitation force

$$\varphi \simeq \varphi_{\ddot{x},1} - \varphi_{F,1}. \tag{4.8}$$

A comparison of the settling time and accuracy of results obtained with the DFT, the synchronous demodulation and the adaptive filter methods was carried out by Abeloos in [48]. In his thesis, Abeloos concluded that the adaptive filter exhibits a faster and more accurate estimation of the measured signal than the performance offered by the synchronous demodulation. Similar conclusions were also drawn by Hippold *et al.* [49], who compared experimentally the capacity of the adaptive filter and synchronous demodulation to retrieve the phase lag of a signal. From their experiments, they concluded that, for a similar cut-off frequency of the phase detector and temporal signal, the adaptive filter leads to smaller fluctuations in the estimated phase lag compared to the synchronous demodulation. As a consequence of these observations, the adaptive filter method appears to be the most suitable choice and will therefore be implemented in this thesis.

4.4 Identification of backbone curves

To experimentally identify an NNM, the *force appropriation* method is commonly employed [28]. While the theoretical definition of NNMs, as introduced in Section 2.2.2, assumes conservative systems, experimental conditions invariably involve damping. Consequently, the non-conservative form of the equations of motion must be considered when describing the dynamics of experimental systems. The force appropriation method is particularly well suited to this context.

The force appropriation method is based on the principle that an NNM arises when the external excitation force precisely compensates for the system's dissipative forces [53]. This principle is illustrated in Figure 4.2, where the terms are obtained by expressing Equation 2.23 in the frequency domain.

Because nonlinear systems generate harmonics, this force-dissipation equilibrium must hold at every harmonic component of the motion. This equilibrium can be represented graphically in a complex plane, as illustrated in Figure 4.2. An NNM occurs when the excitation force counteracts the damping at each harmonic. In the case of viscous damping, this results in a phase quadrature between the excitation force and both the system displacement and acceleration [28]. In conclusion, a phase lag of $\pi/2$ rad between the excitation and the response at each harmonic is required to ensure the presence of an NNM.

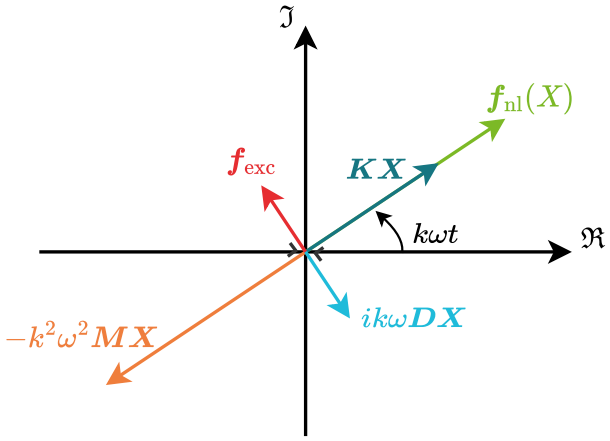

Figure 4.2: Phase diagram describing the dynamics of the k-th harmonic of an NNM motion of a non-conservative system (derived from Equation 2.23 expressed in the frequency domain). The excitation force $\boldsymbol{f}_{\mathrm{exc}}$ is in phase quadrature with the system displacement and acceleration, and it balances out the damping term.

Because of the presence of multiple harmonics in nonlinear systems dynamics, the application of such a method requires the use of a multi-point, multi-harmonic excitation force. Each harmonic of the excitation force must be in phase quadrature with the corresponding harmonic of the system's response at the collocated point. Such requirements are usually not practically feasible during vibration testing; as a consequence, a mono-harmonic single excitation is often employed. This approximation proved sufficient in the case of lightly damped structures with well-separated modes, where the fundamental harmonic dominates the dynamics [28, 54]. However, caution is required in the vicinity of internal resonances or when modes are closely spaced, where higher harmonics have a greater influence on the system's response [28].

Following the previous discussion, an NNM motion can be approximated by imposing a phase lag

φ_{ref} of $-\pi/2$ rad between the system's response and the collocated excitation force. Imposing such a phase lag while gradually increasing the excitation force F allows tracking the backbone curves of nonlinear systems. The first step in the algorithm consists in locking the system's state at the initial reference state, which is fixed by a phase lag imposed at $-\pi/2$ rad and a low forcing amplitude that is chosen by the experimenter. Typically, the forcing amplitude is selected so that the system lies initially in the vicinity of its linear regime. Once the system response has converged to a steady-state, the force is gradually increased, at a rate that allows the convergence of the system to a steady-state for each loop iteration.

It is important to note that, under experimental conditions, shaker dynamics cause a phase lag between the voltage input and the actual force delivered. Consequently, the phase lag between the voltage signal and the system's response may not exactly be $-\pi/2$ rad, but such a phase lag will be observed between the applied excitation force and the system's response. Moreover, if the excitation and measurement points are not collocated, an additional phase lag arises between the applied force and the measured response due to propagation delay of the force along the structure. Algorithm 1 presents the methodology used during backbone tracking.

Algorithm 1 Identification of backbone curves of nonlinear systems using the PLL method.

1: $\varphi_{\text{ref}} \leftarrow -\pi/2$
2: $F \leftarrow F_{\text{init}}$
3: **loop**
4: Convergence of the PLL ($\Delta\varphi \rightarrow 0$)
5: Computation of the amplitude of the response
6: $F \leftarrow F + \Delta F$
7: **end loop**

4.5 Identification of frequency response curves

The identification of the NFRCs is led similarly as the computation of the backbone curves. To compute the NFRCs, the amplitude of the forcing signal F_0 is fixed by the experimenter, and an initial phase reference φ_{init} is also imposed. Once the system is locked to the initial state, *i.e.,* once the phase of the system is locked to the desired state, a sweep in the phase is triggered.

Typically, to construct a complete bifurcation diagram, the reference phase is selected such that the computation of the NFRCs begins well before or well after the resonance. It is then gradually modified to reach the resonance condition, and subsequently adjusted continuously until the system is no longer in the vicinity of resonance. Usually, the phase reference is swept from 0 to $-\pi$ rad; however, as previously mentioned, the presence of the shaker may introduce a phase lag between the voltage signal and the applied excitation force, which consequently affects the monitored phase difference between the voltage signal and the system's response. Algorithm 2 describes the methodology employed for the computation of the NFRCs.

4.6 Gain tuning of the PI controller

The PLL method presented in this chapter employs a PI controller to control the phase lag of the system. The properties of such controllers were highlighted in Chapter 3. In the context of the

Algorithm 2 Identification of NFRCs of nonlinear systems using the PLL method.

1: $F \leftarrow F_0$
2: $\varphi_{\text{ref}} \leftarrow \varphi_{\text{init}}$
3: **loop**
4: Convergence of the PLL ($\Delta\varphi \rightarrow 0$)
5: Computation of the amplitude of the response
6: $\varphi_{\text{ref}} \leftarrow \varphi_{\text{ref}} + \Delta\varphi_{\text{increment}}$
7: **end loop**

PLL employed in the identification of the NFRCs and backbone curves of nonlinear systems, it is widely acknowledged that, to date, the tuning of the controller gains remains largely heuristic. As highlighted by Peter *et al.* [28], several studies were carried out concerning the stability requirement for integral and PI controllers of nonlinear systems, and can be found in [13, 49].

The development of a systematic procedure for determining the controller gains of the PLL remains an active area of research. Recently, multiple studies have been conducted proposing methodologies to facilitate the tuning of controller gains. Hippold *et al.* [49] proposed a more systematic design approach for backbone tracking using a PLL method. Their work was established on the fundamental assumptions that the amplitude and phase lag of the system evolve slowly compared to the action of the phase controller, and that the normal modes are well-separated and no internal resonance occurs. The determination of the PI controller gains was based on the linear dynamics of the system, and the resulting gains were retained throughout the computation of the backbone curve. To derive the ideal controller gains, Hippold *et al.* investigated the asymptotic behaviour of the system around the locked state. From their mathematical developments, they found an expression of the controller gains that depends solely on the linear dynamics of the system. According to their results, the tuning of the gains led to a fast and robust tracking of backbone curves.

On the other hand, Denis *et al.* [13] analysed the stability condition of a Duffing oscillator controlled by the PLL method implemented with a purely integral controller for any imposed phase, *i.e.,* to track backbone curves or NFRCs. Similarly to the analysis of Hippold *et al.*, they used the averaged dynamics of the system to derive the amplitude and phase of the signal at steady-state, from which a stability criterion is established. Denis *et al.* also investigated the influence of the integral gain on the stability of the system. They concluded that increasing the integral gain extends the boundary of the stable region, thereby contributing, up to a certain extent, to the stabilisation of the controlled system. Furthermore, it was observed that the optimal value of the integral gain depends on both the system damping and the adaptive filter gain.

Finally, Chukwu *et al.* [15] recently introduced a novel controller to employ within the PLL algorithm. This method involves augmenting the conventional PI controller with a nonlinear element, which is combined with a low-pass filter. As this approach is analysed thoroughly in Chapter 9, implementation details are omitted at this stage.

Despite the development of numerous methodologies, a general and direct procedure for determining controller gains that guarantee system stability has yet to be established. In the present study, the controller gains were determined with intuitive reasoning and trial-and-error procedures, with the aim of achieving both rapid convergence and robust performance.

4.7 Parameter selection

In addition to the PI controller gains, the implementation of the PLL method also requires the specification of additional parameters: the open-loop frequency ω_0, the adaptive filter gain μ and the number of harmonics in the adaptive filter n_H.

To ensure convergence of the PLL method towards the desired solution rather than an unintended one, it is essential to select an open-loop frequency ω_0 that lies in close proximity to the target solution. It is common practice to define this frequency as the linear natural frequency of the analysed mode.

The adaptive filter cut-off frequency $\tilde{\mu}$, which depends on both the filter gain and the sampling frequency, is an important property. As related in [49], the cut-off frequency of the adaptive filter is directly linked to the time scale of the transients; as a consequence, this cut-off frequency has a great influence on the speed of the tracking. Indeed, the frequency components not considered in the adaptive filter lead to variations in the estimated Fourier coefficients, which determine the amplitude and phase lag of the signals. As a result, the estimated quantities could be erroneous or no steady-state could be reached. However, it is also important to emphasise that increasing the cut-off frequency enhances the sensitivity of the adaptive filter, particularly with respect to noise disturbances.

Additionally, the number of harmonics n_H in the truncated Fourier expansion of the adaptive filter should be chosen with care. Indeed, considering a high number of harmonics in the adaptive filter may help to mitigate the fluctuation effects in the phase and amplitude detection. Moreover, even if the assumption of weak modal interaction is made in this implementation of the PLL method, so that the weight coefficients associated with high harmonics are expected to be moderate, some type of nonlinearities, such as non-smooth nonlinearities, can create higher harmonics in the system response. As a result, a higher number of harmonics in the adaptive filter leads to less spurious fluctuations, but practical considerations on the real-time controller limit the possible maximal number of harmonics. Too many harmonics can lead to extensive computations, which could slow down the operation speed of the controller, and consequently, the achievable sampling. Furthermore, the highest harmonic coverable without the risk of aliasing is limited by the sampling frequency of the controller [49]. A trade-off between the computational resources, controller capacity and signal aliasing is thus necessary to determine the number of harmonics to be used in the adaptive filter.

4.8 Conclusion

This chapter reviewed the current state of the art of experimental continuation methods applied to identify resonance phenomena in nonlinear systems. Two main branches of experimental continuation methods were introduced: the CBC and the PLL methods. The characteristics of each method, as well as their drawbacks and advantages were summarised.

The focus was then turned to the PLL algorithm and its adaptive filter, which showed an efficient and accurate way of estimating the phase lag of the system with respect to the excitation force. The methodologies behind the identification of the backbone curves and NFRCs were introduced, and the force appropriation method was presented.

Finally, the chapter concluded with a discussion of the principal topical issues concerning the PLL method: the tuning of the controller gains and the parameters of the adaptive filter. Although several recent advances have been made on this subject, such as the works of Hippold *et al.* [49]

and Chukwu *et al.* [15], it was observed that no generalised tuning procedure currently exists for the controller gains of the PLL technique, and that the process remains largely heuristic.

5 Numerical applications of the phase-locked loop method

The PLL method introduced in Chapter 4 is commonly used to obtain NFRCs and backbone curves of nonlinear systems. The principal advantage of the PLL method over alternative techniques lies in its suitability for experimental analysis; nevertheless, it can also be effectively employed in numerical studies.

This chapter investigates the effectiveness of the PLL method in retrieving numerically the characteristics of nonlinear systems. Specifically, the implementation of the PLL method, which is carried out in Simulink, is evaluated.

The analysis begins with a brief overview of the practical aspects of implementing the PLL method in Simulink and the methodology adopted for the numerical experiments. The PLL is initially tested on a simple linear system, and nonlinearities are subsequently introduced to test its ability to track unstable response branches. The chapter concludes with a discussion on the influence of PLL gain tuning on tracking performance and result accuracy.

5.1 Practical considerations on the implementation

Simulink is a high-level graphical programming environment built on MATLAB, widely employed for the modelling, analysis, and simulation of dynamic systems. Due to its intuitive block-diagram interface and seamless integration with MATLAB functions, Simulink is particularly well suited for implementing and testing control algorithms, such as the PLL method. The detailed implementation of the PLL method in Simulink can be found in Appendix A.

In the present numerical investigations, the `ode4` solver, which implements a fourth-order Runge-Kutta integration method with a fixed time step, was used. A time step of 10^{-4} s was adopted for all simulations to ensure sufficient numerical accuracy.

5.2 Methodology

The computation of the NFRCs and backbone curves was conducted by incrementally varying the phase reference and forcing amplitude, respectively, in small discrete steps, as described in Algorithms 1 and 2. The NFRCs were computed by varying the imposed phase lag from 0 to $-\pi$ rad at constant forcing amplitude, while the backbone curves were obtained by fixing the phase lag at $-\pi/2$ rad and gradually increasing the excitation force amplitude. For each computed response, the error tolerance between the measured phase and the reference phase was set to 0.01 rad.

5.3 Single-degree-of-freedom linear system

The implementation of the PLL method is first evaluated on an SDOF linear system, whose dynamics are described by Equation 2.15. This system is interesting as a first evaluation of the PLL method, as it represents the simplest case of study. The parameters of the system used during the experiments are the following: $\omega_0 = 50.3$ Hz and $\zeta = 1.6\%$.

To compute the FRF of the linear SDOF system, the force amplitude is fixed at 5 kN, while it is varied from 1 N to 6 kN for the computation of the backbone curve. The parameters of the PLL method used for the identification of the FRF and the backbone curve are summarised in Table 5.1. The results of the FRF and backbone identification of this SDOF system are presented in Figure 5.1, where the FRF computed with the PLL algorithm is compared to the analytical solution presented in Equation 2.19.

PLL parameter	$\tilde{\mu}$ (Hz)	n_H	k_p (s^{-1})	k_i (s^{-2})
Value	100	1	2	10

Table 5.1: Parameters of the PLL algorithm used in the identification of the FRF and the backbone curve of the SDOF linear system.

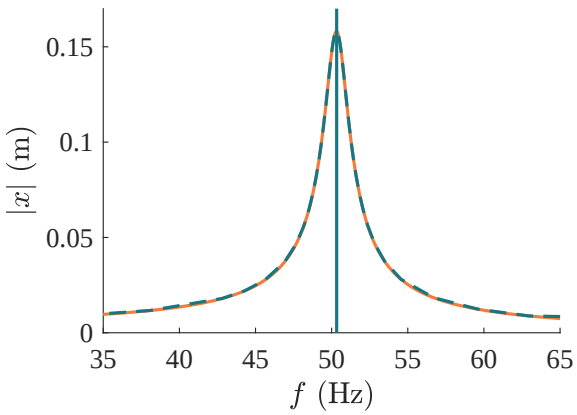

(a) FRF and backbone of the system.

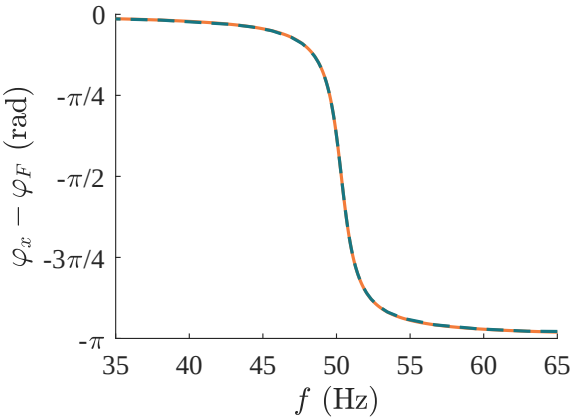

(b) Phase lag between the system response and the excitation force.

Figure 5.1: Comparison of the results obtained with the PLL method (—) and the analytical expression of the FRF (– –).

As observed in Figure 5.1, the FRF and backbone curve were successfully identified. The FRF computed with the PLL algorithm implemented in Simulink matches perfectly with the analytical expression of the FRF of the SDOF linear system. Concerning the backbone curve, it forms a straight line at the resonance frequency of the system, which follows the expected behaviour of the backbone curve of a linear system, as the natural frequency of a linear system does not depend on the amplitude of the excitation force.

The results also demonstrate that the phase lag detected by the adaptive filter implemented in the PLL algorithm is accurate, as the computed phase lag matches closely with the analytical curve. Moreover, the results confirm that amplitude resonance occurs at around $-\pi/2$ rad, which is expected as the system is lightly damped.

5.4 Single-degree-of-freedom nonlinear Duffing oscillator

Following the verification of the method's implementation on an SDOF linear system, nonlinearities are introduced to assess its performance under nonlinear conditions, particularly its ability to stabilise unstable solution branches. A cubic stiffness nonlinearity is introduced into the dynamics of the SDOF system, resulting in a Duffing oscillator described in Equation 2.24. The parameters of the system are the following: $\omega_0 = 50.3$ Hz, $\zeta = 1.6\%$ and $\alpha_3 = 10^7$ N/(kg m^3).

The parameters of the PLL algorithm used to perform the numerical experiments are summarised in Table 5.2. An NFRC of the system was computed with an amplitude of excitation of 5 kN and the backbone curve was determined by varying the excitation amplitude from 10 N to 6 kN.

PLL parameter	$\tilde{\mu}$ (Hz)	n_H	k_p (s^{-1})	k_i (s^{-2})
Value	100	9	100	100

Table 5.2: Parameters of the PLL algorithm used in the identification of the NFRC and the backbone curve of the SDOF Duffing oscillator.

The NFRC and backbone curve of the nonlinear SDOF system identified with the PLL algorithm are illustrated in Figure 5.2. The NFRC and backbone curve computed numerically with the PLL method are compared with the NFRC of the system identified with NI2D software, where the NFRC is computed with the HBM implemented with nine harmonics and the backbone curve is computed using the conservative system. Figure 5.2 demonstrates strong agreement between the two sets of results, thereby validating the ability of the PLL algorithm, when correctly tuned, to stabilise the unstable solution branch of the NFRC. Furthermore, since the fundamental harmonic predominantly governs the system dynamics, the applied force offsets the damping, and the backbone curve computed using the PLL method closely approximates the NNM of the associated conservative system. Finally, as the system is lightly damped, amplitude resonance and phase resonance coincide.

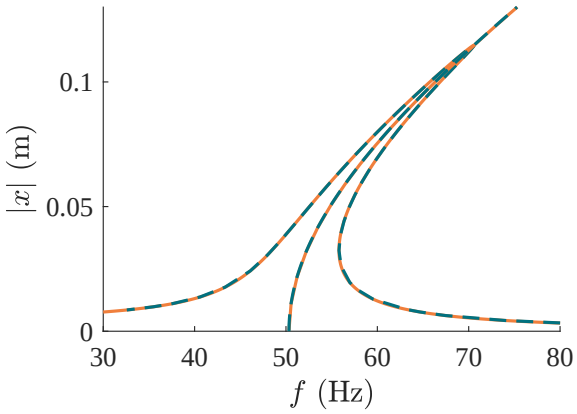

(a) NFRC and backbone curve of the system computed with the PLL method (– –) and the HBM (– –). The backbone curve computed with the PLL algorithm is compared with the NNM.

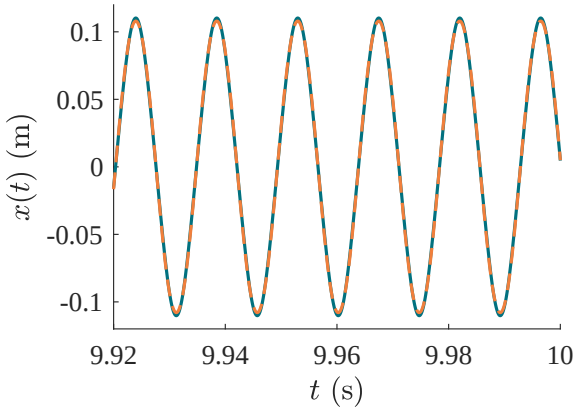

(b) Comparison between the temporal response of the system (– –) and the approximation of the signal reconstructed using the coefficients associated with the fundamental harmonic of the Fourier expansion computed with the adaptive filter (– –).

Figure 5.2: Results obtained with the PLL method applied to the SDOF Duffing oscillator.

A comparison between the reconstructed signal using the first harmonic of the fitted Fourier series implemented in the adaptive filter and the system response is presented in Figure 5.2b. This figure represents the temporal signals at steady-state when a phase lag of -1.2 rad is imposed. The comparison between the exact and approximated signals demonstrates the effectiveness of the adaptive filter in reconstructing signals from a Fourier basis, and highlights the approximation's ability to capture the signal's essential characteristics.

5.5 Single-degree-of-freedom softening-hardening system

To conclude this validation section, the PLL method is tested on a system displaying softening-hardening nonlinearities. To simulate such a system, a quadratic stiffness term is added to the Duffing oscillator defined in Equation 2.24. The equation of motion of this system is presented below

$$\ddot{x}(t) + 2\zeta\omega_0\dot{x} + \omega_0^2 x(t) + \alpha_3 x(t)^3 + \alpha_2 x(t)^2 = F\cos(\omega t), \tag{5.1}$$

where α_2 is the quadratic stiffness coefficient. The softening-hardening nonlinear system exhibits multiple unstable regions; as a consequence, investigating the performance of the PLL in retrieving these various unstable branches is of interest.

To compute the NFRC of the system, an excitation amplitude of 4 kN was applied. The backbone curve was obtained by sweeping the forcing amplitude from 1 N to 5 kN. The parameters of the PLL employed during the identification are presented in Table 5.3, and the parameters of the system are as follow: $\omega_0 = 50.3$ Hz, $\zeta = 1.6\%$, $\alpha_3 = 7 \times 10^6$ (N/kg m^3) and $\alpha_2 = 1.5 \times 10^6$ (N/kg m^2).

PLL parameter	$\tilde{\mu}$ (Hz)	n_H	k_p (s^{-1})	k_i (s^{-2})
Value	20	17	300	100

Table 5.3: Parameters of the PLL algorithm used in the identification of the NFRC and the backbone curve of the SDOF nonlinear softening-hardening system.

The results obtained with the PLL method are presented in Figure 5.3, where it is observed that the NFRC computed with the PLL method matches closely with the NFRC computed using the HBM method implemented with 17 harmonics. This final observation validates that the PLL algorithm is able to track multiple unstable branches of an NFRC.

The effect of the number of harmonics n_H included in the Fourier basis implemented in the adaptive filter is presented in Figure 5.3b. Particularly, this figure compares the exact response of the system at steady-state with the approximation obtained by including different numbers of harmonics in the Fourier basis of the adaptive filter. As observed in this figure, to obtain a sufficiently accurate approximation of the system response, at least three harmonics are required in the truncated Fourier expansion. The response was obtained by using the PLL with an imposed phase lag -0.52 rad between the system response and the external excitation force.

The influence of the quadratic term on the system dynamics is clearly evident in Figure 5.3b, as seen in the smoother response for negative displacements and the sharper transitions for positive displacements. Moreover, the asymmetry in the response is characteristic of even-order harmonics. As shown in the figure, incorporating the second harmonic in the expansion enables the reconstruction of these observed features.

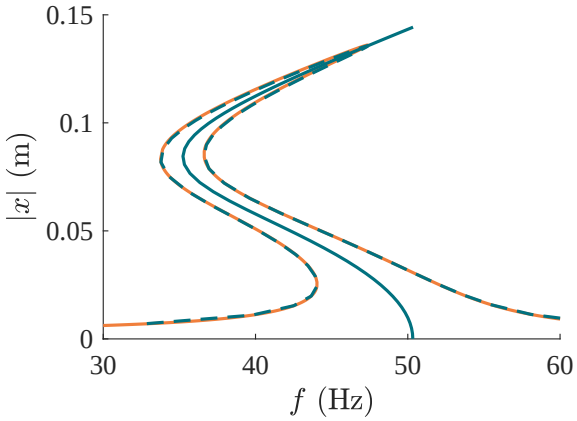

(a) NFRC and backbone curve computed with the PLL method (—) and the HBM (– –).

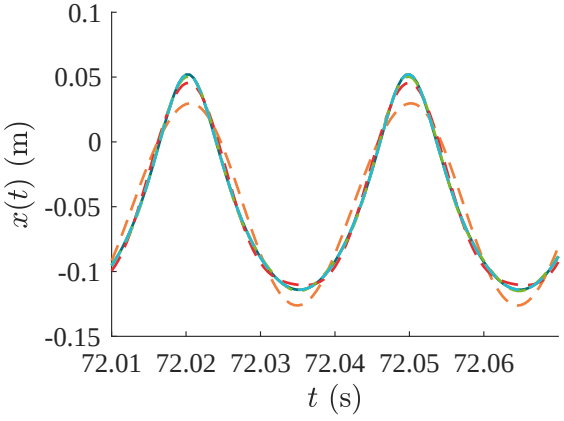

(b) Comparison of the temporal response of the system (—) and the signal approximation obtained with the adaptive filter with multiple values of n_H: $n_H = 1$ (– –), $n_H = 2$ (– –), $n_H = 3$ (– –), $n_H = 9$ (– –), and $n_H = 17$ (– –).

Figure 5.3: Results obtained with the PLL method applied to the SDOF softening-hardening nonlinear system.

5.6 Parameter analysis

To perform the numerical computations, several parameters were specified. While selecting the sampling frequency and the number of harmonics in the Fourier expansion of the adaptive filter is relatively straightforward for numerical experiments, determining appropriate values for the adaptive filter step-size factor μ and the proportional and integral gains k_p and k_i of the PI controller is considerably more complex.

To illustrate the effect of the adaptive filter gain μ, the phase lag estimated by the adaptive filter is computed in open-loop tests on the Duffing system presented in Section 5.4 for various values of μ and an amplitude of excitation of 5 kN. The open-loop frequency is fixed at the linear natural frequency of the system and the number of harmonics in the Fourier series of the adaptive filter is fixed at nine. To generalise the results, the adaptive filter gain μ is multiplied by the sampling frequency and normalised by the linear natural frequency of the system, so that $\tilde{\mu}/\omega_0 = \mu f_s/\omega_0$ is varied.

Figure 5.4 presents the phase lag between the system response and the excitation force estimated by the adaptive filter for values of $\tilde{\mu}/\omega_0$ ranging from 0.02 to 20. As illustrated in the results, increasing the adaptive filter cut-off frequency accelerates the settling of the phase estimation but also leads to larger oscillation amplitudes, as the phase detector becomes more sensitive. Under experimental conditions, signal-to-noise ratio is an important factor, and a noisy signal entering the adaptive filter with a high cut-off frequency could lead to spurious phase fluctuations. Consequently, the choice of the cut-off frequency should result from a compromise between speed of response, accuracy and stability. In the presented scenario, it is observed that the adaptive filter cut-off frequency of 100 Hz, leading to a gain $\mu = 0.01$, which was adopted during the experiments, is a satisfactory choice. For the experiments performed on the softening-hardening system, the cut-off frequency was reduced, as some unstable orbits were difficult to stabilise.

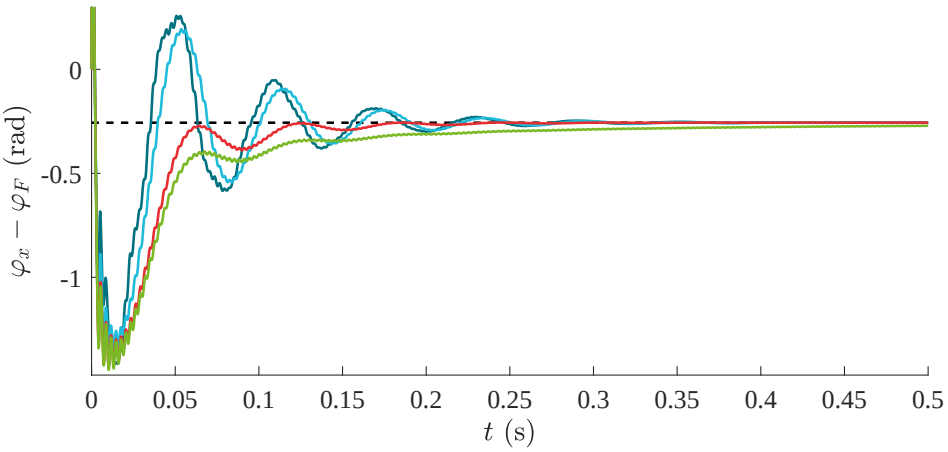

Figure 5.4: Phase lag estimated by the adaptive filter for open-loop tests performed on the Duffing oscillator. Various values of the adaptive filter cut-off frequency were imposed: $\tilde{\mu}/\omega_0 = 20$ (—), $\tilde{\mu}/\omega_0 = 2$ (—), $\tilde{\mu}/\omega_0 = 0.2$ (—) and $\tilde{\mu}/\omega_0 = 0.02$ (—). The reference phase lag of -0.26 rad is also illustrated (– –).

The effects of the proportional and integral gains of a PI controller were reviewed extensively in Chapter 3. It was concluded that the proportional gain helps stabilising the control system, but introduces a steady-state error. In contrast, the integral gain eliminates the steady-state error and enhances the tracking ability of the controller with greater speed and robustness. However, excessively high integral gains should be avoided, as they can induce instabilities in the system. As a consequence, the tuning of the PI gains was guided by a trade-off between robustness, tracking speed, and accuracy.

For the linear system, gain tuning was relatively straightforward, as the response remained stable. The integral gain was set to 10 s^{-2} to enable sufficiently fast curve tracking while limiting controller-induced oscillations. The proportional gain was set to 2 s^{-1} to enhance system stability. This value could have been slightly increased or decreased without significantly affecting the system response.

In contrast, gain tuning for the nonlinear systems was more challenging, as the controller had to stabilise one or more unstable response branches. The integral gain was increased to 100 s^{-2} in both cases to accelerate convergence to the steady state, and the proportional gain was raised to higher values to stabilise the unstable branches. For the softening-hardening system, the proportional gain was set to 300 s^{-1} as lower values failed to stabilise all points on the NFRC.

Figure 5.5 illustrates the effects of the PI gains on the response of the softening-hardening system for a forcing amplitude of 4 kN and a reference phase lag of –0.44 rad, *i.e.*, when the system response is located on the first unstable branch shown in Figure 5.3a, which is particularly challenging to stabilise. During the computations, the PI gains were varied, while the remaining parameters were fixed as detailed in Section 5.5.

In Figure 5.5, the gain tuning used for the computation of the NFRC and the backbone curve of the softening-hardening system (Figure 5.3), that is $k_p = 300$ s^{-1} and $k_i = 100$ s^{-2}, is represented by a black line. This case serves as the reference for the following discussion.

For the same proportional gain as the reference case, increasing the integral gain results in faster convergence, while decreasing it slows convergence. In both cases, the response remains stable

and approaches the desired state. Conversely, keeping the integral gain constant but reducing the proportional gain causes insufficient stabilisation, with the response oscillating between neighbouring points on the same solution branch. Increasing the proportional gain introduces small initial oscillations during stabilisation, but the system ultimately stabilises. Finally, when both gains are too low, the response jumps between solution branches without stabilising. When set too high, the gains render the system overly sensitive, resulting in high-frequency oscillations and preventing stabilisation. For clarity, this case is not illustrated in the figure. Although the integral gain could have been increased during the computations, the chosen value was sufficient to ensure fast and accurate response tracking.

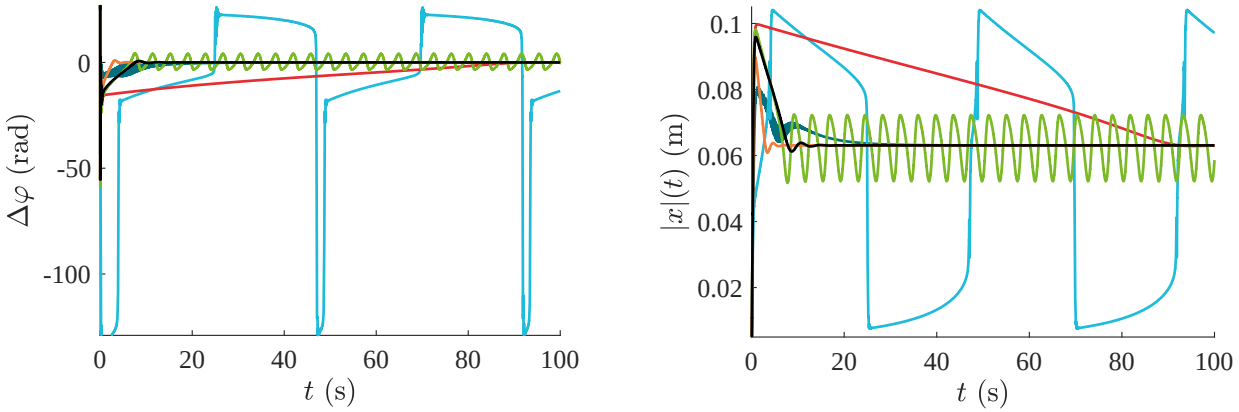

(a) Temporal variation of the phase error.

(b) Temporal variation of the amplitude of the system response estimated with the adaptive filter.

Figure 5.5: Illustration of the effect of PI controller gains of the PLL method on the response of the softening–hardening system. Various gain combinations were used: $k_p = 300$ s^{-1} and $k_i = 100$ s^{-2} (—), $k_p = 300$ s^{-1} and $k_i = 300$ s^{-2} (—), $k_p = 300$ s^{-1} and $k_i = 8$ s^{-2} (—), $k_p = 250$ s^{-1} and $k_i = 100$ s^{-2} (—), $k_p = 900$ s^{-1} and $k_i = 100$ s^{-2} (—) and $k_p = 10$ s^{-1} and $k_i = 8$ s^{-2} (—).

5.7 Conclusion

The implementation of the PLL method in Simulink was numerically validated on numerous models displaying linear and nonlinear behaviours. The computation of the NFRCs and backbone curves with the PLL implemented in Simulink proved efficient to retrieve precisely the characteristics of nonlinear systems numerically.

The effects of the number of harmonics included in the Fourier basis of the adaptive filter were analysed. It was observed that, for nonlinear systems, a sufficient number of harmonics is required to accurately model the measured response. However, increasing the number of harmonics raises computational cost, necessitating a trade-off between accuracy and efficiency.

An analysis on the effect of the adaptive filter gain μ was also performed, and it was concluded that higher gains are favourable as they speed up the computation time; however, these gains are limited by the noise-induced fluctuations, which can be particularly problematic during experiments at low-excitation levels. The effects of the PI controller gains on system dynamics were illustrated. It was observed that the integral gain facilitates faster response tracking, while the proportional gain is crucial for stabilising unstable orbits. Consequently, fixing the adaptive filter and PI controller gains involves a trade-off among these parameters to robustly and rapidly stabilise unstable orbits.

The approach presented in this chapter can readily be extended to MDOF systems, provided that the modes are sufficiently well separated. As these analyses closely resemble those conducted for SDOF systems, they are not presented in this work.

In conclusion, the numerical validation confirmed the robustness of the Simulink-based PLL implementation and supports the feasibility of its subsequent experimental application.

6 Experimental validation of the phase-locked loop method implemented in Simulink

This chapter presents the experimental validation of the PLL algorithm implemented in Simulink. The tests focus on two distinct systems: an electronic Duffing oscillator and a nonlinear beam. The objective of this section is to evaluate the ability of the implemented method to experimentally retrieve the NFRCs and backbone curves of the tested structures.

Details of the experimental setups of the electronic Duffing oscillator and the nonlinear beam are provided in the following sections. Subsequently, the results derived from the application of the PLL method are presented, followed by a discussion on the ease of use, gain tuning, and precision of results offered by the PLL method.

6.1 Methodology

Prior to applying the PLL algorithm to a system, its linear natural frequencies are first identified. These frequencies may be determined, for example, by using a low-amplitude sine sweep force to excite the system's linear response, or by performing an experimental modal analysis (EMA).

After having determined the natural frequencies of the system, the NFRCs and backbone curves are drawn. To compute an NFRC, the amplitude of the voltage signal is fixed, and the imposed phase lag is varied from an initial phase lag φ_{init}, which is often set to 0 rad, to a final phase lag $\varphi_{\text{final}} = \varphi_{\text{init}} - \pi$ rad. However, as will be detailed in Section 6.4, the presence of the shaker and its dynamics shifts the imposed phase lag, as a phase delay exists between the voltage signal sent to the shaker and the measured excitation force applied to the beam.

The backbone curve is computed by enforcing a phase lag that satisfies the phase quadrature criterion between the measured acceleration of the structure and the applied excitation force. Once the phase is locked, the excitation amplitude, which is initially set at a very low level, is gradually increased until the maximum desired amplitude is reached.

6.2 Practical considerations

To conduct the tests, the structures are controlled through a Simulink model via a MicroLabBox (dSPACE), which is programmed using a Real-Time Interface (RTI) for Simulink. This setup enables real-time modification of the PLL implementation parameters, facilitating the tuning of the PI controller gains to track the NFRCs and backbone curves.

During the experiments, the sampling frequency is set to 10 kHz. According to the Shannon-Nyquist criterion, to avoid aliasing

$$f_s \geq 2f_{\max}, \tag{6.1}$$

where f_s is the sampling frequency and $f_{\max}$ is the highest frequency considered in the analysed system. Moreover, for real-time control in closed-loop systems, this frequency is recommended to be approximately 10–20 times the system's closed-loop bandwidth [42]. Given the experimental frequency range, which is from 20 Hz to 400 Hz for the fundamental frequencies, and the low rate of phase or voltage signal variation during PLL tracking, the chosen sampling frequency is more than sufficient.

6.3 Electronic Duffing oscillator

The first experiment is conducted on an electronic Duffing oscillator, which is presented in Figure 6.1. This system is characterised by low damping and a modular cubic nonlinearity [55].

The fundamental operating principle of this electronic Duffing oscillator is that its output voltage is governed by a Duffing equation

$$C_1C_2R_4R_5\ddot{V}_{\text{out}} + p_1\frac{C_2R_4R_5}{R_1}\dot{V}_{\text{out}} + p_2\frac{R_4R_7}{R_2R_6}V_{\text{out}} + p_3\frac{g_m^2R_4R_7^3}{R_3R_6^3}V_{\text{out}}^3 = V_{\text{in}}, \tag{6.2}$$

where the parameters R_i and C_i for $i = 1, ..., 7$ are the resistance and capacitance values of the electrical circuit. The system was designed by Raze; detailed information regarding its implementation can be found in [55].

6.3.1 Setup description

The characteristics of the system are modified using the three knobs of the potentiometers located at the bottom of the printed circuit board (PCB) in Figure 6.1. These knobs are used to modify the system damping (p_1), stiffness (p_2) and cubic nonlinearity (p_3).

To measure the potentiometers p_1, p_2 and p_3, the corresponding switches are flipped to connect the potentiometers to the power supply. The output of the buffer connected to these potentiometers is connected to three test points, which are located at the bottom left of the PCB in Figure 6.1. A voltmeter can be used to measure the voltage at these test points; for a power supply V_s, the identified values correspond to p_iV_s. As the power supply V_s was at 15.08 V during the experiments, the values of the potentiometers could be determined.

The mass m, damping c, stiffness k and cubic nonlinear coefficient k_3 of the system can finally be computed by comparing the equation of a classical Duffing oscillator (Equation 2.24) with Equation 6.2, where the values of the resistances and capacitances are defined in [55]. These parameters are summarised in Table 6.1.

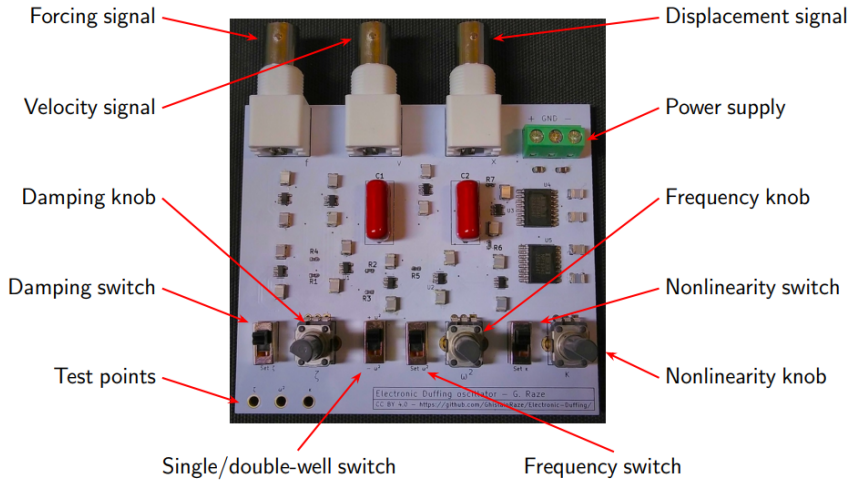

Figure 6.1: Photograph of the electronic Duffing oscillator. [55]

Parameter	Value
p_1	0.4496
p_2	0.2566
p_3	0.472
m (s^2)	10^{-4}
c (s)	4.496×10^{-4}
k (-)	2.566
k_3 (V^{-2})	0.472
ω_0 (Hz)	25.49
ζ (%)	1.4

Table 6.1: Parameters of the Duffing oscillator.

To drive the electrical circuit and measure its response, BNC connectors are used. The driving force is applied through the forcing signal port, and the displacement and velocity of the system are measured as outputs of the system. In this experiment, the displacement signal is used as the input to the PLL algorithm.

As outlined in [55], the electronic circuit is not ideal, and the three primary undesired effects are voltage offsets, which hinder perfect symmetry in the oscillator; imperfect integrators resulting from finite open-loop gains; and an imperfect nonlinearity due to inaccuracies in the analogue multipliers. However, these limitations did not qualitatively alter the results.

6.3.2 Results

To identify the NFRCs of the electronic Duffing oscillator, the PLL algorithm was employed with varying amplitudes of the excitation signal. To capture the NFRCs, phase sweeps from 0 to $-\pi$ rad were performed at various voltage amplitudes. To determine the backbone curve, the phase was locked at $-\pi/2$ rad, and the amplitude of excitation was continuously increased from 0.001 V to 1.35 V. The integral and proportional gains were adjusted between the different experiments to ensure a fast and robust tracking of the NFRCs. Their values are presented in Table 6.2. Finally, the adaptive filter cut-off frequency $\tilde{\mu}$ was set to 100 Hz, and 17 harmonics were used in the adaptive filter, which is more than sufficient for the experiments conducted, given that mainly the first and third harmonics are expected to play a major role in the system response.

The identification of the NFRCs and backbone curve was successfully carried out, as demonstrated in Figure 6.2a. The resulting curves reveal that the system exhibits a hardening behaviour, which is consistent with the characteristics of the Duffing oscillator. Additionally, it was observed that as the amplitude of excitation increases, the nonlinear behaviour of the system becomes more pronounced, whereas for the lowest excitation levels, the system behaves nearly linearly. This can be attributed to the cubic term in the nonlinear equation, which remains negligible for small displacements and increases significantly as the displacement grows. Finally, Figure 6.2a illustrates a strong agreement between the various NFRCs and the backbone curve, which represents the locus of amplitude peaks of the NFRCs, thereby further confirming the effectiveness of the PLL implementation in accurately capturing the system's characteristics. Figure 6.2a demonstrates the ability of the PLL

Type of curve	F (V)	k_p (s^{-1})	k_i (s^{-2})
NFRC	0.04	10	25
NFRC	0.08	10	25
NFRC	0.3	50	100
NFRC	0.6	50	100
NFRC	0.9	250	500
NFRC	1.2	250	500
Backbone	0.01 $\rightarrow$ 1.4	20	50

Table 6.2: Controller gains used for the identification of the NFRCs and backbone curve of the electronic Duffing using the PLL method.

to experimentally stabilise and track the unstable branch of the fundamental resonance of a Duffing oscillator.

It is also interesting to observe the evolution of the phase between the displacement and the applied force when varying the frequency of excitation of the system. The results, presented in Figure 6.2b, exhibit the characteristic behaviour of hardening nonlinear systems, which display a bump near the resonance phase. The phase of resonance remains constant across increasing amplitudes of excitation, but appears at higher frequencies as the amplitude of excitation increases. This observation is in agreement with the behaviour of a hardening system.

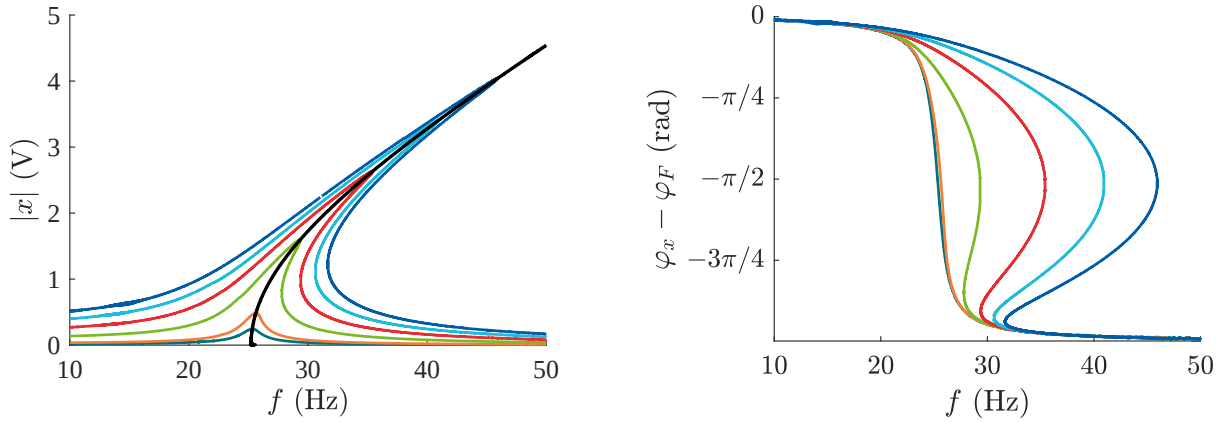

(a) NFRCs and backbone curve (—).

(b) Phase lag between the displacement and the forcing signal.

Figure 6.2: Application of the PLL method to the electronic Duffing oscillator. Various excitation amplitudes were used: 0.04 V (—), 0.08 V (—), 0.3 V (—), 0.6 V (—), 0.9 V (—) and 1.2 V (—).

To further validate the results, the NFRC drawn at a forcing amplitude of 1.2 V is superposed to the response of the system to sine sweep up and down excitations at the same voltage amplitude. The results are presented in Figure 6.3, where it is observed that the NFRC identified with the PLL method overlaps well with the response of the system to classical sweep up and down excitations. As Figure 6.3 highlights, the PLL method enables the recovery of the unstable part of the NFRC of the fundamental resonance of the Duffing oscillator, which cannot be detected using classical identification methods.

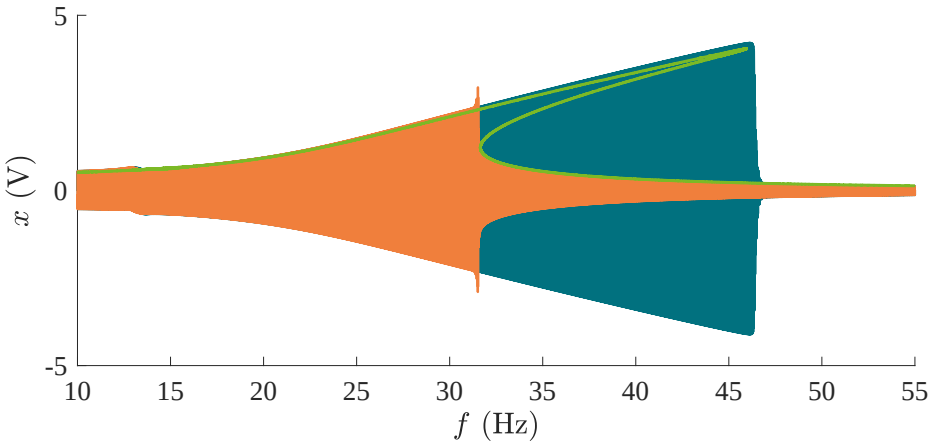

Figure 6.3: Superposition of the NFRC identified with the PLL method (—) and the system response to sweep up (—) and down (—) excitations for a forcing level of 1.2 V.

6.4 Nonlinear beam

While the electronic Duffing oscillator allowed initial experimental testing of the PLL method, it corresponds to almost ideal testing conditions and does not reflect the typical challenges associated with *shaker–structure interactions*. This section experimentally applies the PLL method to the first three modes of a clamped beam excited by a shaker.

6.4.1 Setup description

The steel structure comprises two sections: a main beam (700 mm×14 mm×14 mm) and a laminated end (40 mm×14 mm×0.5 mm), clamped within a steel block. The setup is shown in Figure 6.4. The nonlinearity of the structure mainly arises from large displacement-related effects, *i.e.,* geometric nonlinearity.

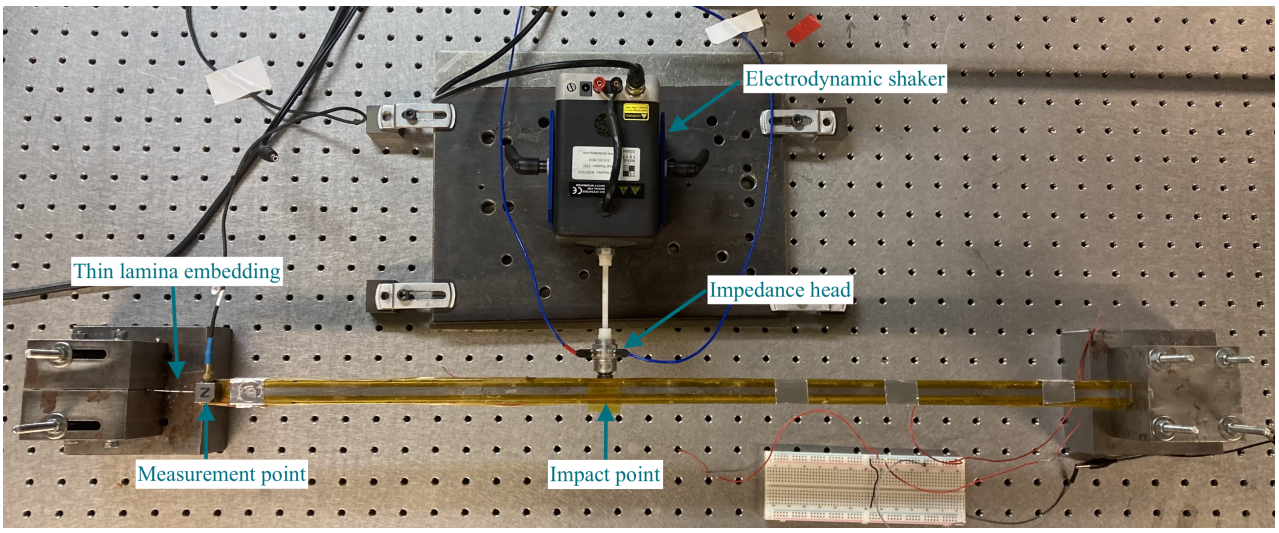

Figure 6.4: Setup of the nonlinear beam.

To perform the tests, an electrodynamic shaker (Modal Shop K2007E01) is connected to the beam through a plastic rod. An impedance head (Dytran 5860B), glued 30 cm from the left end of

the beam (excluding the lamina), measures both the applied force and the acceleration at the driving point. A triaxial accelerometer is placed at the left tip of the beam to record the system response and extract the NFRCs and backbone curves for the first three modes. The positioning of the impedance head and accelerometer was guided by an EMA, detailed in Appendix B.

6.4.2 Results

The EMA allowed the identification of the first three natural frequencies of the beam in the direction of the excitation, which are located at 35 Hz, 140 Hz, and 400 Hz.

To apply the PLL algorithm, the voltage signal sent to the shaker was used as an input to the adaptive filter instead of the forcing signal measured by the impedance head. This approach enabled the consideration of the entire plant, comprising both the structure and the shaker, during the experiment. As a result, shaker-structure interactions were not accounted for.

Nevertheless, it is important to mention that, due to the shaker's inertia, the voltage signal and the excitation force measured at the impedance head are not perfectly in phase. Consequently, amplitude resonance does not occur at or near a phase lag of $-\pi/2$ rad between the system's acceleration and the input signal, as would be expected in an ideal case because the structure is lightly damped. Instead, a constant phase shift is observed. Nonetheless, phase quadrature is still evident between the system's response and the collocated applied excitation force. Similar observations were reported by Gabos *et al.* in [56].

Additionally, due to shaker-structure interactions, the force applied to the structure when performing a frequency sweep is not constant, even when the forcing voltage maintains a constant amplitude. In light of this, the mean amplitude of the measured excitation force is employed to quantify the effective amplitude of the force applied to the structure.

Finally, it is important to note that the experimental setup was operated near its physical limits, with the maximum feasible excitation amplitude nearly reached. The primary limitation arose from the mounting of the impedance head; as it was glued to the beam, and high excitation forces caused it to detach frequently.

For the experiments conducted on the three modes, the PLL method was applied with the adaptive filter cut-off frequency fixed at 100 Hz, and the number of harmonics included in the Fourier basis, n_H, set to nine.

First mode of the nonlinear beam

The identification of the NFRCs of the first mode of the nonlinear beam is done by exciting the structure with different excitation amplitudes, with mean values of the applied force ranging from 1.1 N to 7.3 N. The integral and proportional gains used during the experiments are summarised in Table 6.3. The results are displayed in Figure 6.5a.

The controller gains were mainly adjusted across the measurements to improve tracking speed, which was achieved by increasing the integral gain. The proportional gain was increased consequently to ensure stability, as detailed in Sections 3.3 and 5.6.

As Figure 6.5a shows, the structure exhibits a *softening-hardening* behaviour. The hardening nonlinear behaviour comes from the clamping of the thin lamina, whereas the softening behaviour may be due to deformation of the lamina from previous experiments, creating a bending moment

Type of curve	F (V)	F_{mean} (N)	k_p (s^{-1})	k_i (s^{-2})
NFRC	0.05	1.1	10	50
NFRC	0.1	2.6	10	50
NFRC	0.15	4.1	10	75
NFRC	0.25	7.3	25	90
Backbone	$0.005 \rightarrow 0.3$	$0.5 \rightarrow 7.5$	35	110

Table 6.3: Controller gains used for the identification of the NFRCs and backbone curve of the first mode of the nonlinear beam.

when it is clamped. Figure 6.5a also demonstrates the capability of the PLL method to stabilise the unstable part of the NFRC.

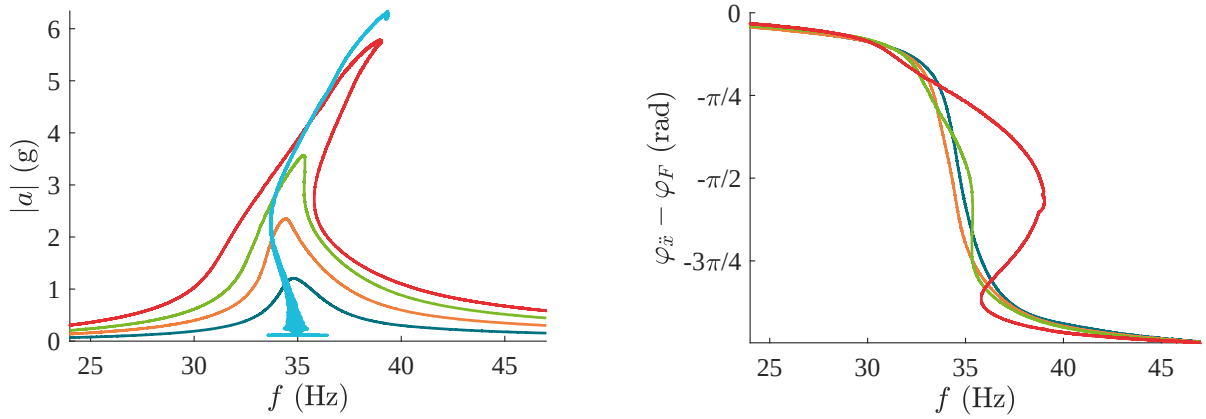

(a) NFRCs and backbone curve (—).

(b) Phase lag between the acceleration of the beam and the forcing signal.

Figure 6.5: Application of the PLL algorithm to the first mode of the nonlinear beam. Various amplitudes of excitation were used: 1.1 N (—), 2.6 N (—), 4.1 N (—) and 7.3 N (—).

The backbone curve shown in Figure 6.5a is slightly shifted from the maxima of the NFRCs. This shift arises from the presence of the shaker in the test setup and the non-collocation of the excitation and measurement points used for the PLL tracking. Consequently, the resonance of the overall system was not detected at a phase lag of $-\pi/2$ rad, the phase lag imposed during the measurement of the backbone curve, but rather at -1.65 rad. As several high-amplitude experiments were conducted between the acquisition of the NFRCs and the backbone measurement, the system's properties appear to have undergone slight alterations, potentially due to structural heating during testing or progressive deformation of the lamina under large excitation amplitudes. As a result, the backbone curve corresponding to the measured NFRCs and a phase lag of -1.65 rad could not be fully retrieved. Nevertheless, the results remain sufficiently consistent to conclude that the algorithm successfully identified the NFRCs associated with the first mode of the nonlinear beam.

The variation of the phase lag between the acceleration of the beam and the excitation signal is illustrated in Figure 6.5b. This figure further reveals the softening-hardening behaviour of the system. Initially, a decrease in the resonance frequencies is observed between the two lowest excitation levels, where the softening behaviour is predominant. At higher excitation levels, the resonance frequency increases, reflecting a transition to a hardening behaviour. Additionally, at high excitation amplitudes, the softening response is evident for phase lag close to 0 rad and $-\pi$ rad, where a slight reduction in

frequency precedes a more pronounced increase due to the onset of hardening behaviour. Figure 6.5b also proves that the amplitude resonance occurs at a phase lag lower than $-\pi/2$ rad, as previously mentioned.

Second mode of the nonlinear beam

The second mode of the nonlinear beam is located at around 140 Hz. The NFRCs were identified for mean applied force amplitudes ranging from 0.4 N to 22.6 N. The controller gains used during the identification are presented in Table 6.4, and the corresponding results are displayed in Figure 6.6. The integral gain was increased between experiments to accelerate the tracking. As no unstable response branches required stabilisation during these tests, the gain tuning process was relatively straightforward, and the proportional gain was kept constant.

Type of curve	F (V)	F_{mean} (N)	k_p (s^{-1})	k_i (s^{-2})
NFRC	0.01	0.4	2	15
NFRC	0.1	3.7	25	45
NFRC	0.4	13.6	25	100
NFRC	0.7	22.6	25	150
Backbone	$0.005 \rightarrow 0.75$	$0.2 \rightarrow 30$	25	100

Table 6.4: Controller gains used for the identification of the NFRCs and backbone curve of the second mode of the nonlinear beam.

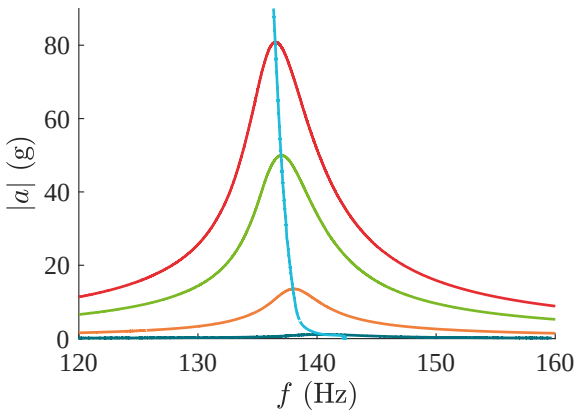

(a) NFRCs and backbone curve (—).

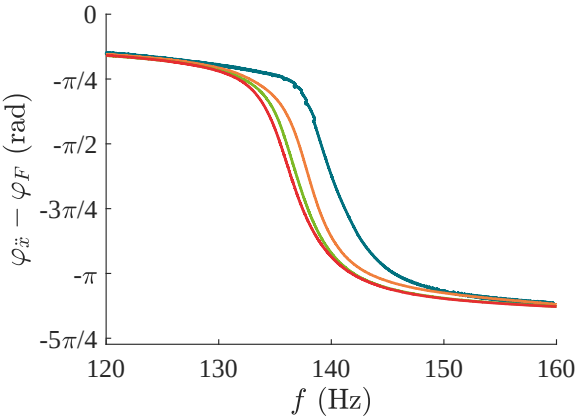

(b) Phase lag between the acceleration of the beam and the forcing signal.

Figure 6.6: Application of the PLL algorithm to the second mode of the nonlinear beam. Various amplitudes of excitation were used: 0.4 N (—), 3.7 N (—), 13.6 N (—), 22.6 N (—).

The NFRCs and the backbone curve of the second mode show a softening behaviour of the beam, which is also seen in the phase lag between the measured acceleration and the input signal. Further increasing the amplitude of excitation would have been of interest; however, this was limited by the experimental setup, particularly due to the impedance head, which frequently detached as a result of the beam oscillations. The resonance phase of this mode occurs at a phase lag of about -2.2 rad between the voltage signal and the system's response, and shows the softening tendency of the second mode.

An unwrapping of the measured phase difference between the acceleration signal and the excitation voltage was performed to enable the computation of the NFRCs for this mode. The phase lag is computed in the adaptive filter by using MATLAB's `atan2` function, which returns values constrained within the interval $[-\pi, \pi]$ rad. As a consequence, discontinuous phase jumps occur at these boundaries. Although these jumps are purely numerical artefacts, they disrupt the application of phase sweeps required for NFRC computation, as the controller is designed to follow continuous, monotonic variations in phase.

Figure 6.7 demonstrates the quality of the adaptive filter to retrieve the amplitude of the acceleration signal when the fundamental harmonic dominates the dynamics. In this figure, the NFRCs obtained with the PLL algorithm align closely with the acceleration signal measured by the accelerometer.

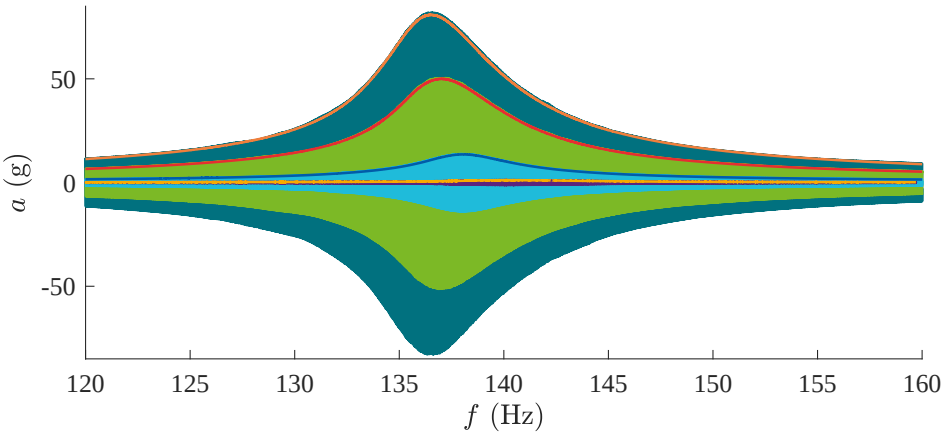

Figure 6.7: Comparison of the acceleration signal measured by the accelerometer and the NFRCs computed with the PLL method for the second mode of the nonlinear beam. Various excitation amplitudes were used: 0.4 N (—), 3.7 N (—), 13.6 N (—), and 22.6 N (—).

Third mode of the nonlinear beam

Finally, the third mode of the beam is at about 400 Hz. The integral and proportional gains of the controller used for the identification of these curves are summarised in Table 6.5. The NFRCs and the backbone curve identified using the PLL method, with the applied force having a mean amplitude ranging from 0.4 N to 20.6 N, are shown in Figure 6.8a. As observed in Figure 6.8, the third mode of the beam exhibits a similar behaviour to the second one, being characterised by a softening behaviour. The tuning of the PI controller gains was performed similarly as described for the second mode of the beam.

Figure 6.9 illustrates the variation of the excitation force measured at the impedance head as a function of its frequency. This figure highlights the shaker-structure interactions that were previously mentioned. Notably, whereas the amplitude of the excitation force is expected to be constant, a significant drop in the forcing signal is observed at the beam's resonance frequency. During this phenomenon, known as the *force drop-off*, the system appears to behave as if the beam were exciting the shaker, rather than the reverse. In strongly nonlinear systems, where higher-order harmonics are prominently present in the structural response, these components may also appear in the measured excitation force. Such behaviour is observed in detail in Section 8.4.2.

Type of curve	F (V)	F_{mean} (N)	k_p (s^{-1})	k_i (s^{-2})
NFRC	0.01	0.4	50	100
NFRC	0.1	4.4	50	125
NFRC	0.4	15	50	200
NFRC	0.7	20.6	50	250
Backbone	0.005 $\rightarrow$ 0.8	0.2 $\rightarrow$ 25	25	100

Table 6.5: Controller gains used for the identification of the NFRCs and backbone curve of the third mode of the nonlinear beam.

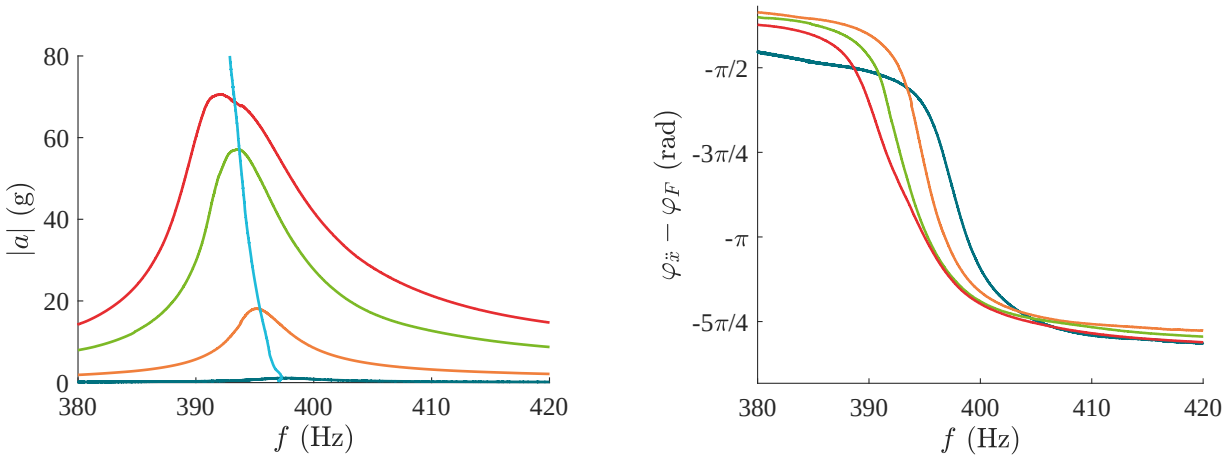

(a) NFRCs and backbone curve (—).

(b) Phase lag between the acceleration of the beam and the forcing signal.

Figure 6.8: Application of the PLL algorithm to the third mode of the nonlinear beam. Various amplitudes of excitation were used: 0.4 N (—), 4.4 N (—), 15 N (—), 20.6 N (—).

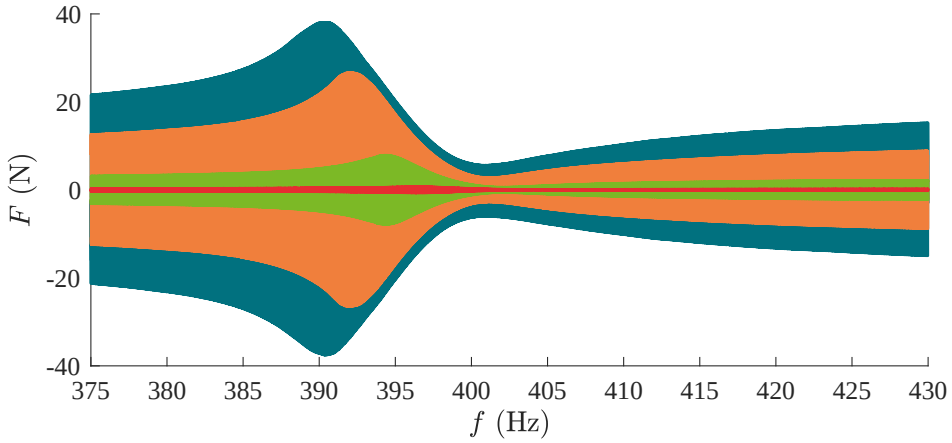

Figure 6.9: Excitation force measured by the impedance head. Various excitation amplitudes were applied: 0.4 N (—), 4.4 N (—), 15 N (—), and 20.6 N (—). The force drop-off phenomenon is illustrated.

6.5 Effects of controller gain tuning on the performance of the phase-locked loop method

A well-established fact in the application of PLL to the study of nonlinear dynamic systems is that gain tuning remains largely heuristic. To date, no fully automated method has been established for tuning of the controller and adaptive filter gains within the PLL, although some investigations into this topic have been conducted [15, 49].

During this initial series of experiments, several practical insights were gained regarding the selection of appropriate controller gains. These conclusions are outlined in the following paragraphs.

As mentioned in Section 3, the integral gain of the PI controller is used to eliminate the static error arising from the proportional gain, as well as dampen the effects of external disturbances. When adding the integral gain to the PI controller of the PLL method, the locking of the PLL to the desired phase was performed faster. The higher the gain, the faster the convergence towards the specified phase lag. However, an excessively high gain can cause oscillatory or unstable control, which should be avoided.

Another factor that influenced the performance of the PLL method in accurately tracking the backbone curve and the NFRCs was the imposed phase or force sweep. Lower sweep rates provide the controller with more time to adapt and converge towards the reference signal. However, excessively low sweep rates are impractical, as the time required to build an NFRC or a backbone curve can become prohibitively long. During the experiments presented in this chapter, a compromise was made between the magnitude of the gains and the imposed sweep rates.

Furthermore, it was observed that tuning the gains of the controller becomes more difficult when the system exhibits a pronounced unstable branch in its NFRC, as displayed in the highest amplitude NFRCs in Figure 6.2a. In such cases, it was observed that increasing the proportional gain of the controller helped to stabilise the unstable response.

Finally, it is interesting to note that the system must be properly locked to the specified initial state before starting to activate the sweep of the PLL. If the controlled system is not stabilised before starting the phase or force sweep, or if the sweep rate is too fast for the controller to follow, oscillations are observed in the NFRCs. Such transient regimes are illustrated in Figure 6.10, where oscillations are visible at the beginning of the highest amplitude NFRC. Similar observations were also made by Denis *et al.* in [13].

6.6 Conclusion

The implementation of the PLL algorithm in Simulink was successfully validated experimentally on both the electronic Duffing oscillator and the nonlinear beam. The NFRCs and backbone curves of both systems were identified, and their nonlinear behaviour was analysed.

In addition to validating the implementation of the PLL method, this chapter reviewed several challenges that may arise during experimentation. These factors include shaker-structure interactions, which affect the excitation force applied to the structure, and the tuning of the controller gains, which plays a fundamental role in the successful application of the PLL method, as the gains determine the system's ability to lock to the specified state. The effects of force and phase sweep rates on the

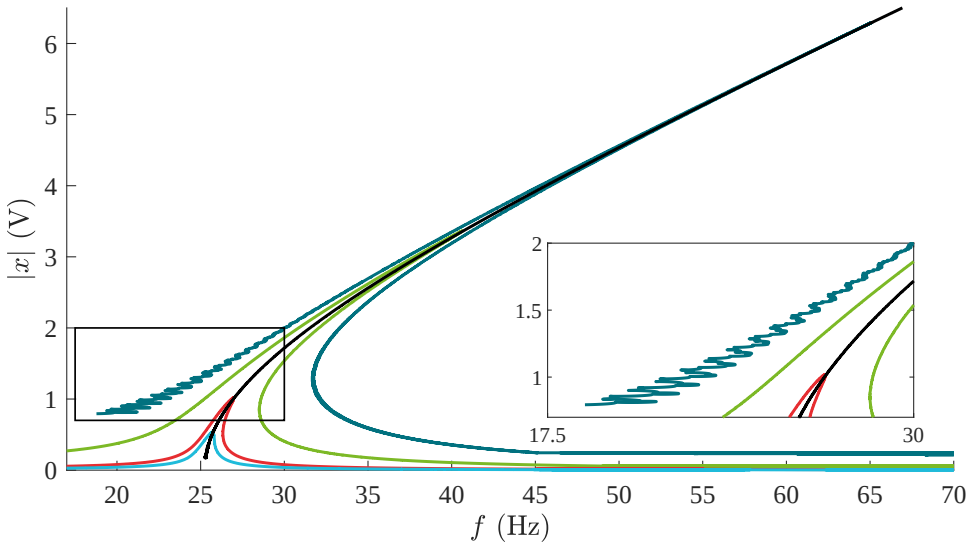

Figure 6.10: NFRCs and backbone curve identified using the PLL method on the electronic Duffing oscillator for various levels of excitation: 0.04 V (—), 0.08 V (—), 0.4 V (—), and 1.2 V (—). The 1.2 V NFRC shows the oscillations created by the controller of the PLL at the beginning of the phase sweep.

convergence of the PLL were also illustrated, and the effectiveness of the adaptive filter in retrieving the characteristics of a signal under real-time conditions was demonstrated.

7 Implementation of a phase-locked loop method in LabVIEW

The primary objective of this thesis is to investigate the feasibility of implementing a PLL method in LabVIEW to identify the NFRCs and backbone curves of nonlinear systems during vibration testing. This chapter first introduces LabVIEW software and its working principles. The emphasis is then placed on LabVIEW FPGA module, which enables the use of the designed circuit in a real-time module, a capability crucial for the experimental application of the PLL method. The challenges encountered during the implementation of the PLL using the LabVIEW FPGA module are discussed in detail, with an explanation of the design decisions made throughout the process. This chapter concludes with a discussion of the feasibility and potential applications of such a design for vibration testing in the industry.

7.1 Presentation of LabVIEW

LabVIEW is a graphical system design and development platform created and distributed by National Instruments (NI). It consists of a programming environment that employs a visual programming language, known as G, in which functional nodes are interconnected through wires that facilitate the flow of data, similar to the approach used in Simulink. LabVIEW is widely employed in data acquisition, instrument control, and is used for application development at V2i.

7.2 Introduction to FPGA

FPGAs, also known as *field-programmable gate arrays*, are reprogrammable, pre-fabricated integrated circuits capable of implementing user-defined logic operations and functions. A key characteristic of FPGAs is their ability to be reprogrammed multiple times.

FPGAs were first introduced in 1985 by Xilinx, which presented its XC2064 FPGA [57]. Their origins are linked to the development of integrated circuits during the previous decades. The initial cellular arrays primarily consisted of a two-dimensional array of logic cells that were programmed during the manufacturing process to implement a variety of two-input logic functions. Field-programmability, characterised by the potential to reconfigure the logic function of a chip after the manufacturing process, was accomplished in the 1960s. In the following decade, integrated circuits incorporating read-only memory (ROM) were developed, offering a novel approach to the implementation of logic functions. Since its inception, FPGA technology has evolved continuously, transitioning from static memory-based designs to ROM-based implementations, and has expanded exponentially. For instance, while the XC2064 device comprised 64 logic blocks and 58

input/output ports, modern FPGAs can contain over 300,000 logic blocks and approximately one thousand input/output ports [58].

7.2.1 Architecture of an FPGA chip

A typical structure of an FPGA integrated circuit is presented in Figure 7.1. In this architecture, three main components are found: an array of programmable logic blocks, which usually contain different types of logic, including general logic, memory, and multiplier blocks. A programmable routing fabric interconnects these blocks, transforming the circuit code into a functional electronic circuit. The third main component of an FPGA chip is input/output (I/O) ports, which are located at the boundary of the circuit. As their name suggests, these pins allow the FPGA to communicate with external components through its input and output interfaces. In this project, the inputs will be the signals from the accelerometers, whereas only one output will be used to actuate the shaker with the signal derived from the PLL algorithm.

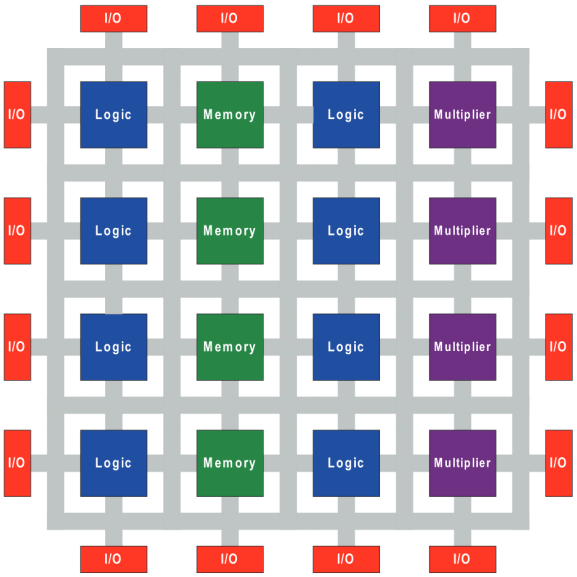

Figure 7.1: Standard FPGA architecture. [58]

FPGA chips operate based on a complex architecture and underlying principles. A comprehensive discussion of all elements constituting an FPGA cell is beyond the scope of this thesis. To ensure clarity and conciseness, this chapter will focus solely on the components relevant to the design of the PLL in LabVIEW. For a more in-depth understanding of FPGA chips and their fundamental principles, the reader is referred to [59, 60, 61].

7.3 Integration of FPGA hardware in LabVIEW

The implementation of a PLL in LabVIEW is undertaken using the LabVIEW FPGA module. This module enables the development of FPGA code written in LabVIEW on NI hardware equipped with user-programmable FPGAs [62]. In this project, a CompactRIO system was used.

In addition to the FPGA module, LabVIEW also includes the Real-Time module, which plays a crucial role in the development and deployment of stand-alone, real-time applications that run on embedded hardware devices. Together, these modules enable the execution of LabVIEW code on alternative hardware targets, such as the CompactRIO.

More precisely, the Real-Time module enables the LabVIEW project to be downloaded and executed on a dedicated controller board that has its own real-time operating system. As a result, this module ensures that the LabVIEW code will continue to run accurately, even if the host machine encounters a technical issue.

The FPGA module is used to run a LabVIEW program in an embedded system that uses FPGA. FPGA chips have the intrinsic property of being inherently parallel programmable logic devices. This

property is exploited by the LabVIEW FPGA module, where parallelism can be easily implemented by graphically coding parallel operations in the block diagram window. Naturally, for LabVIEW's parallelism to be effective, the parallelized operations must be independent of one another, as any data dependency between them would impose a sequential execution constraint.

7.3.1 CompactRIO

The CompactRIO is a real-time embedded controller produced by NI. It offers high-performance processing capabilities. The CompactRIO includes a real-time processor, configurable I/O modules, a user-programmable FPGA, which is useful for executing high-speed logic operations, and an Ethernet expansion chassis [63]. The controller inside the CompactRIO runs a Linux Real-Time operating system.

In this project, a CompactRIO-9054, presented in Figure 7.2, is used. Some of its specifications are listed in Table 7.1, and the complete datasheet can be found in [64].

Figure 7.2: CompactRIO-9054 chassis with I/O modules (NI 9234 and NI 9263).

Processor	
CPU	Intel Atom E3805
Number of cores	2
CPU frequency	1.33 GHz
Reconfigurable FPGA	
FPGA type	Xilinx Artix-7 A100T
Number of flip-flops	126,800
Number of 6-input LUTs	63,400
Number of DSP slices (18x25 multipliers)	240
Available block RAM	4.86 Mbits

Table 7.1: Processor and FPGA specifications of CompactRIO-9054. [64]

Hardware specifications

Certain FPGA specifications must be carefully considered when designing an FPGA-based application. These include the limitations of the FPGA board and its logic operation capabilities. To better understand these constraints, it is essential to introduce the concepts of look-up tables (LUTs),

flip-flops, digital signal processing slices (DSPs), and block random access memory (BRAM). The presentation of these FPGA components is based on [65].

Each FPGA chip consists of a specified number of resources with programmable interconnects, which facilitate the implementation of the electronic circuit designed using block diagram code in the LabVIEW FPGA module. When an FPGA VI is implemented, the coded block diagram represents the architecture of the logic on the FPGA chip. During compilation, the graphical code is converted into the corresponding FPGA circuit [65].

LUTs

LUTs are collections of logic gates that are hardwired onto the FPGA. They store precomputed output values for various input combinations, enabling the rapid retrieval of corresponding outputs for logic operations. LUTs are used to perform Boolean algebra inside FPGAs.

Flip-flops

Flip-flops are employed in FPGA systems to temporarily store processed results and to synchronise them with the global clock [66]. They are essential elements for implementing sequential logic, such as shift registers or pipelining architectures, where access to both current and previous states is required.

DSP48E

A DSP48E slice is a DSP logic element found in the Xilinx Artix-7. This type of slice is used to perform arithmetic operations such as (high-throughput) addition, multiplication or sine and cosine computation. DSP48E slice includes a multiply-accumulator, multiply-adder, and an n-step counter. In addition to performing arithmetic operations, this type of slice can also perform logic operations.

Block RAM

Block RAM, also known as block memory, is a RAM that is used inside the FPGA to store data. It is commonly used in FPGAs due to their efficiency in implementing large amounts of memory. LabVIEW generally uses block RAM when it comes to the use of `Memory` and `FIFO` functions in FPGA VIs.

LabVIEW FPGA resource allocation

A notable feature of LabVIEW FPGA that must be considered is its automatic allocation of logic resources. LabVIEW determines whether operations defined in the graphical code are implemented using look-up tables (LUTs), block RAM (BRAM), or DSP slices (DSP48s), depending on the type of logic described. This resource allocation is handled autonomously by the compiler and cannot be directly modified or overridden by the user, except by explicitly modifying the design of the code (*e.g.,* by changing the data type or the operation performed). It is therefore essential to consider this characteristic during design, as the number of available hardware resources is limited, as shown in Table 7.1.

7.3.2 Modules I/O

Two input and output modules are employed for experimental data acquisition and system actuation. This section provides a brief overview of the selected hardware.

ADC module - NI-9234

To acquire the data during experiments, an NI-9234 module [67] is used. This acquisition module has four analogue input channels, and some of its specifications are reported in Table 7.2. The complete datasheet can be found in [67].

Input characteristics	
ADC resolution (fixed-point data type)	<±24,4> bits
Type of ADC	Delta-Sigma (combined with analogue prefiltering)
Timebase used	
Maximum internal master timebase	51.2 ksample/s/channel

Table 7.2: Input characteristics and timebase of NI-9234 acquisition module. [67]

The data acquired by the NI-9234 module is encoded using a $\langle \pm 24, 4 \rangle$-bit format, in which 24 denotes the total number of bits used for encoding, and 4 represents the number of bits allocated to the integer part. This corresponds to a representable value range of $[-8, 7.99]$ with a resolution of 9.5×10^{-7}. This range and precision are well-suited to the intended applications, as the acquisition module enables the capture of high-precision signals across a sufficiently wide amplitude spectrum. It is worth noting that, in the context of the experimental vibration analysis presented in the following sections, accelerometers with either higher or lower sensitivity may be employed depending on the measurement requirements.

The NI-9234 is an ADC (analogue-to-digital converter) system, meaning that it transforms the measured continuous analogue signal into a discrete digital representation. To do so, the ADC must sample the analogue signal, which is done using a *Delta-Sigma modulation*. The Delta-Sigma modulation is an oversampling method that is used to encode signals into low bit depth digital signals at a very high sample-frequency. In a Delta-sigma modulator, the analogue input signal is sampled at a much higher rate than the Nyquist rate (which is 2 times the maximum frequency in the analysed frequency spectrum).

Another important consideration to take into account in the PLL design is the maximum internal master timebase of the NI-9234. This value indicates the maximal data rate that can be produced by the acquisition module when running at the maximal rate of the built-in clock. In consequence, the NI-9234 can produce, at maximum, 51,200 samples per second.

DAC module - NI-9263

To control the shaker, the NI-9263 is used. NI-9263 is a DAC (digital-to-analogue converter) system, meaning that it turns a digital signal into a continuous one. In this context, the DAC transforms the digital forcing signal into the signal sent to the shaker. NI-9263 has four analogue output channels. Some characteristics of the NI-9263 are presented in Table 7.3, and further specifications can be found in [68].

The data transmitted by the NI-9263 module is coded on $\langle \pm 20, 5 \rangle$-bit format, meaning that values

Output characteristics	
DAC resolution (fixed-point data type)	<±20,5> bits
Output nominal voltage range	± 10V
Maximum internal master timebase	100 ksample/s/channel

Table 7.3: Output characteristics and timebase of NI-9263 analogue output module. [68]

lie in the $[-16, 15.99]$ range, with a precision of 3.05×10^{-5}. This level of precision is sufficient for the intended application.

The data rate allowed by the NI-9263 module is higher than the one accepted by the acquisition module, so the NI-9234 will be the limiting hardware in this setup.

7.4 Implementation considerations

Implementing a PLL in LabVIEW using an FPGA requires a more in-depth understanding of the algorithm and its behaviour in comparison with an implementation in Simulink. Indeed, the LabVIEW FPGA module demands the explicit specification of data width at each node of the circuit, and the selection of a suitable data representation format. Due to the real-time requirements of the application, the controller must guarantee a rapid response with minimal *latency*. Consequently, execution time and delay become critical factors in the design process. Furthermore, it is imperative to consider the combinatorial path length of the implemented circuit, as an excessively long path may lead to timing violations. Such violations indicate that the circuit cannot reliably operate at the specified clock frequency. In addition, the FPGA chip provides a limited number of logic resources for implementing computational operations, which imposes additional design constraints.

This section investigates the various limitations and design challenges faced during the implementation of the PLL in LabVIEW. Most of the implementation details are sourced from the LabVIEW FPGA Module User Manual [69], which provided significant support throughout the exploration and implementation of the PLL code in LabVIEW.

7.4.1 Data type

In FPGA applications, it is a common choice to choose a fixed-point data type [59]. Fixed-point representation has the advantage of allowing higher computing performances as it allows binary and integer operations. These operations are generally less resource-intensive and energy-intensive compared to floating-point operations of equivalent calculations. In LabVIEW, the data fixed-point representation can be tailored by choosing the word length, which corresponds to the number of bits used to represent the whole number, but also the integer word length, which is associated with the number of bits used to represent the integer part of the number. It is also possible to choose if the data is signed, meaning that it can be negative, zero or positive, or unsigned, which means that the data can only be represented by zero or positive numbers. If the data is signed, a bit of the word length is associated with the sign of the number.

7.4.2 Data size

In addition to selecting the type of data to be processed, it is also essential to specify their size. The choice of the data size during the implementation of the PLL was led carefully. A compromise

between the data precision and data size had to be done, as larger data size requires more logic blocks to perform operations.

For example, during the implementation, issues were encountered with the number of DSP48 slices available. Indeed, multiplication operations are commonly assigned to DSP48 slices by LabVIEW. As the implementation of the PLL in LabVIEW requires a great number of such operations, the size of the data had to be selected so that the required number of DSP48 slices did not exceed the available number, which is of 240 (see Table 7.1). The allocation of DSP slices works as follows: one DSP slice is allocated when a 25 bit number is multiplied by a 18 bit one, two DSP slices are used when a 32 bit number is multiplied by a 25 bit number, and for two 32 bit data, 4 DSP logic blocks are required. As a consequence, the data size operated in the adaptive filter had to be slightly reduced. However, no lack of precision in the data was detected in the following.

7.4.3 Throughput versus latency

Another important consideration to take into account in the design is the *throughput* allowed by the program, as well as its latency. Indeed, the PLL implemented in LabVIEW must lead to a fast data processing with acceptable latency.

The throughput is an important consideration in the FPGA implementation of the real-time PLL application. In LabVIEW, the throughput corresponds to the rate at which a functional node delivers information, and more precisely, to the time a functional node requires to perform operations on an input, and return a valid output. The throughput is measured in number of cycles per sample.

On the other hand, the latency refers to the time lag with which signals are processed. The latency is often quantified in number of cycles or in seconds. To modulate the throughput and latency delivered by the implementation, *pipelining* can be used.

7.4.4 Pipelining

Pipelining can be used in LabVIEW to increase the clock rate and the throughput of an FPGA VI or subVI. In essence, pipelined code leverages the parallel processing capabilities of the FPGA to reduce the execution time of sequential operations. Figure 7.3 illustrates the principle of pipelining.

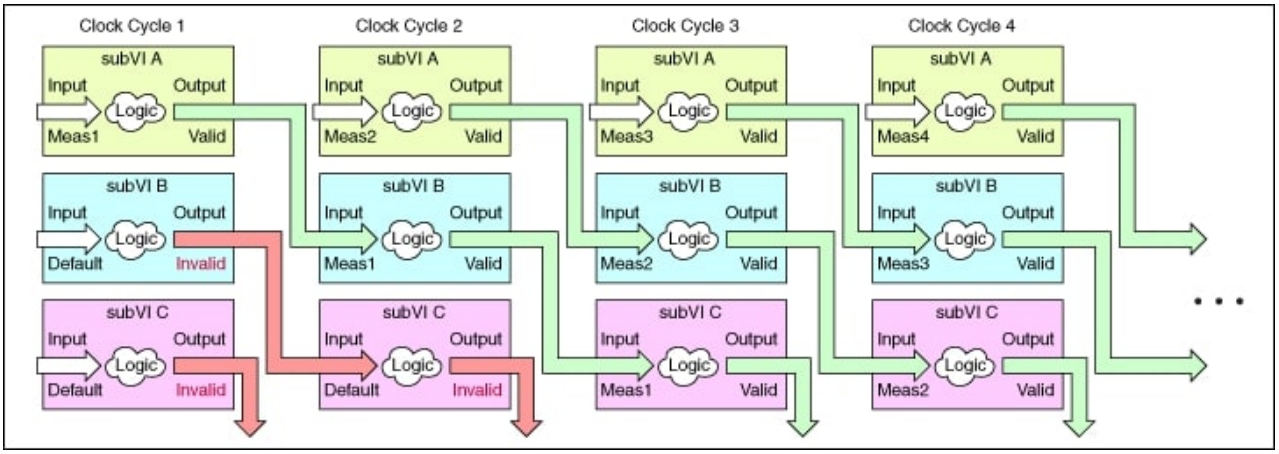

Figure 7.3: Illustration of a pipelining implementation. [70]

In Figure 7.3, the subVIs A, B, and C are placed within a single-clock timed loop. When the three subVIs execute sequentially and no pipelining is implemented, an iteration of the sequence of

subVIs requires the three subVIs to complete their operations before restarting. In consequence, the clock rate of the code sequence corresponds to the sum of the execution time of all the subVIs that it contains.

In a pipelined code, as illustrated in Figure 7.3, subVI A does not need to wait that subVI C has output a valid value to acquire new input. At each clock cycle at which subVI A has output a valid value, it can directly intake a new one. At the first clock cycle, subVI A performs an operation, and outputs a valid value. At that time, subVI A has not output anything valid yet such that subVIs B and C are not operating, and simply output invalid results. During the second clock cycle, the valid output of subVI A enters subVI B, which processes the valid output of subVI A of the first clock cycle, and subVI A takes a new input. SubVI C takes as an entry an invalid value from subVI B, such that it does not perform any operation and also outputs an invalid result. Finally, in the third clock cycle, each subVIs outputs valid results, as the valid output of subVI A of the first clock cycle has finally arrived to subVI C, which processes it. At that time, subVI A processes the third input, and subVI B processes the output of subVI A from the previous clock cycle. The pipeline is now said full, and a valid output exits the code at each clock cycle, having a constant latency of two clock cycles. In pipelined code, the execution time is limited by the subVI that has the longest time execution, i.e., the longest *combinatorial path*.

Note that, in such pipelined structures, the latency of the pipeline, which is often measured in terms of clock cycles, is proportional to the depth of the structure. In the example of Figure 7.3, the depth of the pipelined code is of 3. For a pipelined structure of depth N, a first valid result occurs after N clock cycles, and the valid output of each clock cycle lags behind the input by $N - 1$ clock cycles. As a consequence, the deeper the pipelined structure, the greater the latency of operation.

In the LabVIEW implementation of the PLL, a latency on the order of the microsecond was reached, which is deemed more than sufficient for the required application.

Note that in such FPGA implementations, the *bottleneck principle* applies. This principle is simple and based on the fact that the lowest throughput rate of a series of connected nodes, which corresponds to the shortest time after which valid data outputs the code, is only dependent on the throughput rate of the slowest node, *i.e.,* the node that has the highest throughput rate in the code. In this case, the bottleneck node dictates the operational rate of the circuit. To prevent data loss during operations, it is necessary for the input data rate to be lower than the processing rate.

7.5 Comparison of the implementations of the method in Simulink and LabVIEW

Both LabVIEW and Simulink provide an effective graphical interface for the development of a PLL algorithm. Their operational principles are comparable, as both platforms rely on graphical programming that is subsequently translated into an HDL, such as VHDL. The resulting FPGA code is then deployed onto hardware platforms, namely the MicroLabBox when using Simulink, and the CompactRIO when using LabVIEW.

The principal difference between the two environments is that Simulink offers a much higher-level description of the algorithm, which allows the user to experience greater productivity. On the other hand, the low-level capabilities of LabVIEW, while requiring greater implementation time and technical expertise, enable the user to develop a customised solution that is well suited to the specific problem. For instance, Simulink offers an extensive range of libraries in which a large

number of functions are already implemented. By contrast, the LabVIEW FPGA module provides a more limited set of functions for implementing the PLL, primarily comprising arithmetic and trigonometric operations. As a result, functions readily available in Simulink, such as integrators or phase unwrapping blocks, have to be manually implemented within the LabVIEW interface. However, these customised implementations do not significantly limit the design.

Concerning the performances, both implementations exhibited comparable operational characteristics. The maximal available sampling frequency on the MicroLabBox is of about 20 kHz, whereas a maximal rate of 51.2 kHz can be attained with LabVIEW implementation. An additional important factor to consider is the cost of the hardware and software. In this regard, the LabVIEW-based solution was found to be approximately half the price of the MicroLabBox, which is a significant advantage.

7.6 Conclusion

This chapter presented the implementation of the PLL in LabVIEW using the NI FPGA module. The fundamental operating principles of FPGAs relevant to the implementation were outlined, together with a description of the hardware characteristics. The challenges encountered during the implementation were reviewed, and the rationale behind key design choices was explained.

The chapter concluded with a comparison between the solutions offered by Simulink and LabVIEW, emphasising the respective advantages and limitations of both environments. This discussion included an evaluation of the performance achieved with each platform, confirming that comparable operating frequencies were attained. Moreover, the reached frequency range was deemed more than adequate for the industrial applications anticipated by the V2i company, thereby validating the PLL design in LabVIEW and enabling subsequent experimental validation.

8 Experimental validation of the phase-locked loop method implemented in LabVIEW

This chapter presents the experimental validation of the PLL implementation in LabVIEW. The ability of this implementation to retrieve the characteristics of nonlinear systems in real-time conditions is evaluated. More precisely, the speed of execution and the tracking ability of the method are assessed.

To investigate the method experimentally, three structures are analysed. Firstly, the first mode of the nonlinear beam described in Section 6.4 is investigated. Then, a bolted beam mounted on a shaker head is examined. This testing configuration is interesting for evaluating the PLL method, as the testing conditions resemble those encountered in practical applications at the V2i company. Thirdly, the first mode of a highly nonlinear thin beam is also investigated. For all three case studies, the results obtained using the PLL method implemented in LabVIEW will be compared with those obtained from the Simulink implementation, which was previously validated in Chapters 5 and 6.

8.1 Methodology

During the tests performed with LabVIEW, the sampling frequency was set to 25.6 kHz. It was set to 10 kHz for the Simulink implementation. In all experiments, these sampling frequencies were more than adequate to ensure accurate data acquisition and control, for the same reasons outlined in Section 6.1, as the identified linear natural frequencies of the studied systems ranged from 13 Hz to 50 Hz.

The NFRCs and backbone curves were obtained using the same methodology as described in Section 6.1. Furthermore, as discussed in Section 6.4, the forcing voltage signal, rather than the applied excitation force, was used in the feedback loop of the PLL algorithm.

To perform the computation, the MicroLabBox was used as the real-time interface for the Simulink implementation, similarly to the setup presented in Chapter 6. For the LabVIEW implementation, the CompactRIO presented in Section 7.3.1 was employed.

8.2 Nonlinear beam

The nonlinear beam introduced in Section 6.4 is used as the first case study to evaluate the implementation of the PLL method in LabVIEW. The test of the PLL algorithm on this system mainly aimes to qualitatively determine the ability of the hardware and the implementation to track resonance curves.

8.2.1 Setup description

The testing setup is identical to the one presented in Section 6.4; however, it is important to note that the lamina of the nonlinear beam fractured during transport following the tests conducted previously. It was still possible to clamp the lamina in steel blocks, but the length of the clamped part of the lamina was heavily reduced, so high excitation levels were not reached during these tests to prevent further damage to the beam.

8.2.2 Results

The NFRCs retrieved for the first mode of the nonlinear beam and the corresponding phase lag between the measured acceleration and the forcing signal are illustrated in Figure 8.1. During the tests, the gains were fixed at $k_i = 35\ \mathrm{s}^{-2}$ and $k_p = 10\ \mathrm{s}^{-1}$, and the adaptive filter gain μ was set at 0.01. This gain tuning enabled sufficiently fast and robust tracking of the NFRCs.

As observed in this figure, the first experimental results of the PLL implemented in LabVIEW are promising. The NFRCs still display a combined softening and hardening behaviour, as previously observed in Figure 6.5a, although the associated frequencies are slightly shifted. This outcome was anticipated, as the lamina had to be clamped slightly deeper due to the damage, leading to an increase in system stiffness. Concerning the behaviour of the phase lag, the results are coherent with what is expected from a hardening system, where a slight bump in the phase can be observed for the highest forcing curve. This behaviour was also observed in Figure 6.5b. By taking into account the phase lag existing between the voltage signal and the applied force, it is observed that the phase resonance is close to the amplitude resonance, which is consistent as the structure is lightly damped.

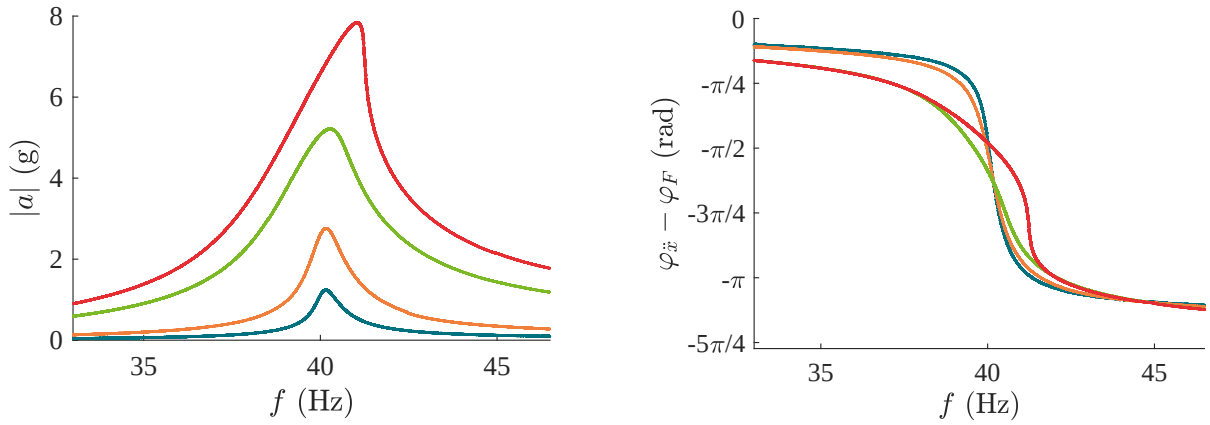

(a) NFRCs of the first mode of the nonlinear beam.

(b) Phase lag between the acceleration of the beam and the forcing signal.

Figure 8.1: Application of the PLL algorithm implemented in LabVIEW on the first mode of the nonlinear beam presented in Section 6.4. The NFRCs were computed for the following mean excitation levels measured at the impedance head: 1.6 N (—), 3.7 N (—), 7.7 N (—) and 10.7 N (—).

8.3 Bolted beam

The second system under investigation is the bolted beam depicted in Figure 8.2. The experimental analysis presented in this section focuses on the first mode of this system.

8.3.1 Setup description

The beam is mounted on an electrodynamic shaker table (G&W V2664), which excites the structure in the vertical direction. Two triaxial accelerometers are employed: one is positioned at the tip of the beam, where high accelerations are expected for the first mode, and the other is located at the base to measure the input acceleration.

The beam (400 mm×40 mm×1 mm) consists of two segments connected by a bolt. This academic system was tested at V2i, and a small rubber element was inserted between the two parts to promote the occurrence of potential nonlinearities within the system. As the objective of the experiments was to trace NFRCs of nonlinear systems, several screw torque levels were applied to determine the configuration that induced the strongest nonlinear behaviour. Although no significant differences were observed between these configurations, it was noted that, for a given excitation level, lower torque values resulted in slightly greater nonlinearity. However, a sufficiently high torque was required to ensure that the structure remained securely in place during the tests; consequently, the torque was set to 9 Nm.

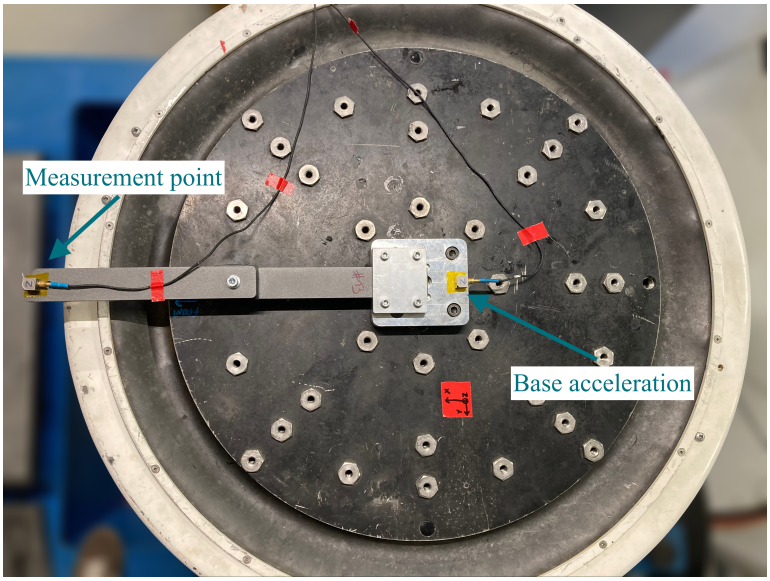

Figure 8.2: Setup of the bolted beam.

8.3.2 Results

The analysis of the bolted beam is restricted to its first mode. The NFRCs corresponding to this mode were computed using both implementations of the PLL method, namely those developed in Simulink and LabVIEW. The results are presented in Figure 8.3. The controller gains used for all computations and with both algorithms were the following: $k_p = 10\ \mathrm{s}^{-1}$, $k_i = 25\ \mathrm{s}^{-2}$, and the adaptive filter gain was set to $\mu = 0.01$. As no unstable response needed to be stabilised during the experiments, the tuning of the PI controller gains was relatively straightforward, and the gains were mainly selected to ensure sufficiently fast tracking by the PLL method.

Figures 8.3a and 8.3b illustrate the softening behaviour of the system, characterised by a decrease in resonance frequency with increasing excitation amplitude. As shown in Figure 8.3a, a slight frequency shift appeared between the 0.9 g, 1.6 g, 1.9 g curves compared to the others. As the experiments were conducted over two separate days, it is highly likely that environmental factors,

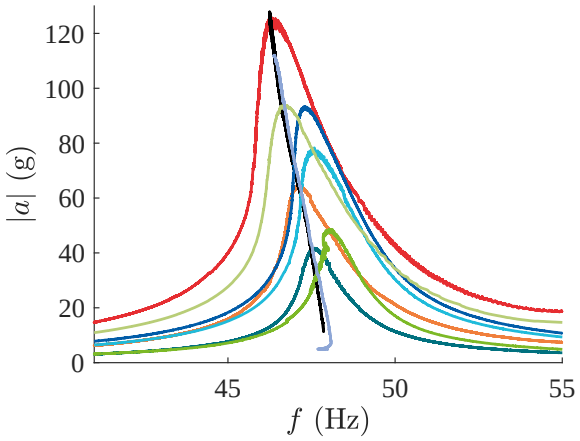

(a) NFRCs and backbone curves.

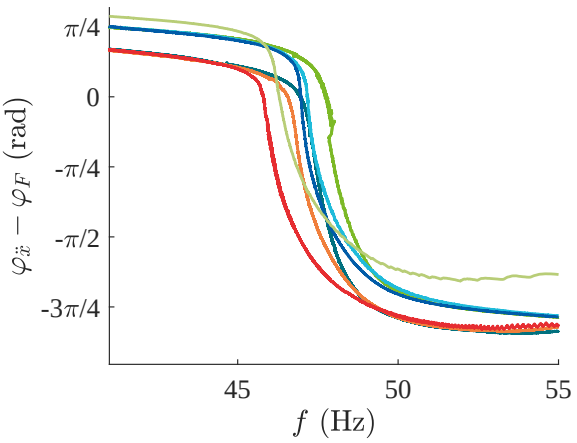

(b) Phase lag between the system acceleration and the forcing signal.

Figure 8.3: Application of the PLL algorithm implemented in Simulink and LabVIEW on the first mode of the bolted beam presented in Figure 8.2. The NFRCs were drawn for various levels of excitation measured at the base, for LabVIEW computations: 0.8 g (—), 1.4 g (—) and 3.4 g (—) and for Simulink computations: 0.9 g (—), 1.6 g (—), 1.9 g (—), 2.7 g (—). The backbone curves computed in LabVIEW (—) and Simulink (—) are also displayed.

such as room temperature or humidity, slightly influenced the system's characteristics, thereby causing a shift in the resonance frequencies. This phenomenon was also observed in the sine sweep tests that were performed, and which are presented in Figure 8.4. This shift in frequencies also accounts for the discrepancy between the backbone curve computed in Simulink and the locus of the three lower-level curves. Nonetheless, the two backbone curves still coincide, as they were computed one after the other, thereby confirming the hypothesis of a modification of material properties and validating the results obtained with both implementations. Tang *et al.* [71] investigated the effect of temperature variations between tests on a system's resonance frequency and concluded that an increase in structural temperature results in a decrease in resonance frequency, which likely accounts

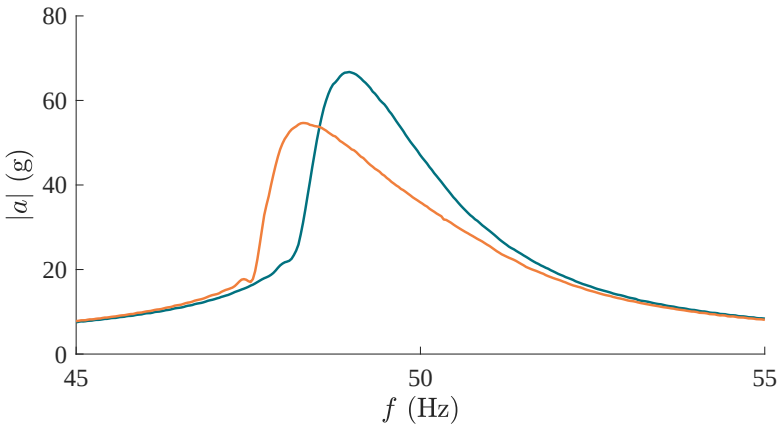

Figure 8.4: FRFs of the bolted beam to sine sweep down excitations of 1.5 g of amplitude measured at the base. The resonance frequency decreased between the measurements taken the first day of tests (—) and the second day of tests (—).

for the shift observed in the present study.

8.4 Thin nonlinear beam

To conclude the experimental validation of the PLL implementation in LabVIEW, an additional system is tested. This system consists of a thin nonlinear beam, which is clamped at both ends. The structure is presented in Figure 8.5. This system is particularly suitable for the experimental validation of the PLL method implemented in LabVIEW, as its response exhibits a significant unstable region even under moderate forcing levels. The analysis detailed in this section is limited to the first mode of this thin beam.

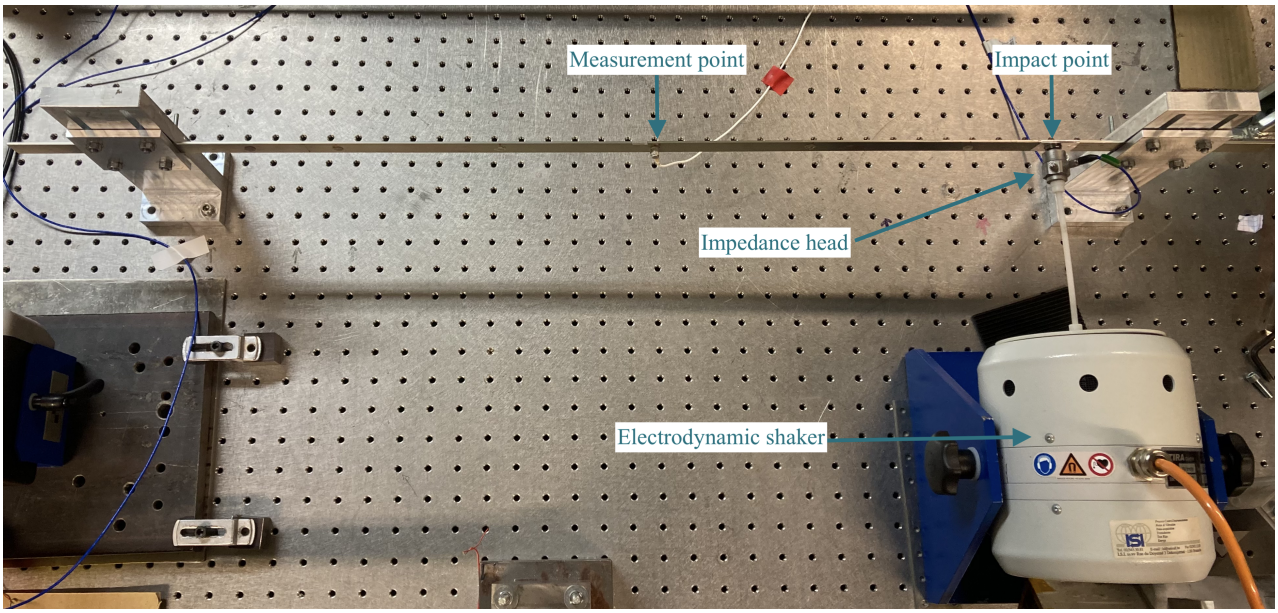

Figure 8.5: Setup of the thin nonlinear beam.

8.4.1 Setup description

The structure analysed is a doubly clamped beam (754mm×20 mm×2 mm) made of aluminium. The system is excited by an electrodynamic shaker (TIRA TV 51057), which is placed on an optical table. This shaker excites the beam through an impedance head (Dytran 5860B), which is linked to the beam through a plastic rod.

The excitation point is placed 70 cm away from the left clamping, whereas a triaxial accelerometer is fixed on the beam at a distance of 38 cm from the left clamping. This triaxial accelerometer is employed to measure the beam response, which is subsequently fed back into the PLL to control the system. Since the analysis focuses on the first mode of the beam, positioning the measurement point at the beam's midpoint is of particular interest, as this location corresponds to the maximum expected deformation. Moreover, because of the system configuration, and more precisely because of the fact that the structure has a mass that is of the same order of magnitude than the moving mass of the shaker, high shaker-structure interactions are expected within the system. Consequently, placing the shaker near the clamping, at a location that is responsive to the target mode shape, seems an interesting choice to minimise these interactions.

8.4.2 Results

The system investigated is heavily sensitive to temperature fluctuations. Consequently, the resonance frequency of its first mode varies depending on its temperature. During the tests, this frequency was estimated at about 13 Hz, but slight variations were observed.

The NFRCs and backbone curves were recovered using both implementations (LabVIEW and Simulink) of the PLL with comparable amplitudes of excitation. The controller gains used during the experiments are summarised in Table 8.1, which also reports the mean amplitude of the applied force measured at the impedance head. The results are presented in Figure 8.6, where Figure 8.6a depicts the NFRCs and backbone curves, and Figure 8.6b shows the variation of the phase lag between the beam acceleration measured by the triaxial accelerometer and the forcing signal. During all experiments, the adaptive filter gain was set to $\mu = 0.01$.

Type of curve	F_{mean} (N)	k_p (s^{-1})	k_i (s^{-2})
NFRC (LabVIEW and Simulink)	0.17 – 0.36	10	15
NFRC (LabVIEW)	1.5	10	75
NFRC (Simulink)	1.7 – 2.3	10	75
NFRC (LabVIEW)	3	5	300
Backbone (LabVIEW and Simulink)	0.05 → 3.5	10	75

Table 8.1: Controller gains used for the identification of the NFRCs and backbone curves of the first mode of the thin beam using both implementations (LabVIEW and Simulink) of the PLL method.

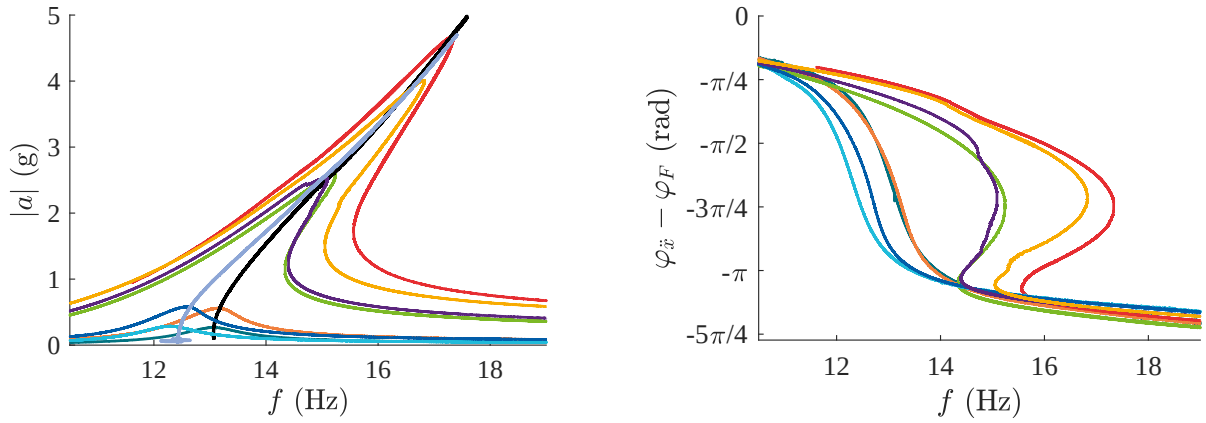

(a) NFRCs and backbone curves.

(b) Phase lag between the system acceleration and the forcing signal.

Figure 8.6: Application of the PLL algorithm implemented in Simulink and LabVIEW on the first mode of the thin beam presented in Figure 8.5. The NFRCs were computed for various levels of excitation measured at the impedance head, for LabVIEW computations: 0.17 N (—), 0.35 N (—), 1.5 N (—) and 3 N (—) and for Simulink computations: 0.19 N (—), 0.35 N (—), 1.7 N (—) and 2.3 N (—). The backbone curves computed in LabVIEW (—) and Simulink (—) are also presented.

Various observations can be made from Figure 8.6. First and foremost, it is observed that the results obtained with both implementations lead to similar outcomes, confirming that the PLL method implemented in LabVIEW can also stabilise unstable response branches. A slight frequency shift is observed in the low-level measurements, similarly to the observations made in Section 8.3. This

small difference is probably caused by the temperature change within the structure, which might have caused a small change in the beam properties.

Concerning the phase lag between the beam response and the voltage signal sent to the shaker, the results correspond to the expected behaviour of a hardening beam, as analysed previously. The backbone curves were traced for an imposed phase lag of -2.2 rad. By taking into account the constant phase lag existing between the forcing signal and the applied force, it is concluded that phase resonance and amplitude resonance coincide, which is expected as the beam is lightly damped.

Finally, it is interesting to note that the gain tuning of the PLL method was particularly difficult when tracking unstable response branches. In this case, the gain tuning had to be adjusted to avoid instabilities, which can be dangerous for both the structure under test and the exciter. In these experiments, stabilising the highest amplitude curves proved more difficult than stabilising the lower-level ones. The gain tuning consequently differed between the two implementations, as a finer gain adjustment was required, and the sampling frequency was set to a different value, necessitating corresponding adaptations of the gains. Specifically, a higher cut-off frequency for the adaptive filter was selected in the LabVIEW implementation, resulting in a phase lag detection that was more sensitive to signal variations and, consequently, a system more responsive to control inputs. Although reducing this cut-off frequency for tracking the curve could have been beneficial, the resonance curve was still successfully tracked.

As shaker-structure interactions are important in the system, the force drop-out phenomenon, which was described in Section 6.4, is clearly visible in the experiments. Figure 8.7 illustrates the phenomenon. Moreover, harmonics created by the beam response are clearly visible in the forcing signal, which is also typical of shaker-structure interactions.

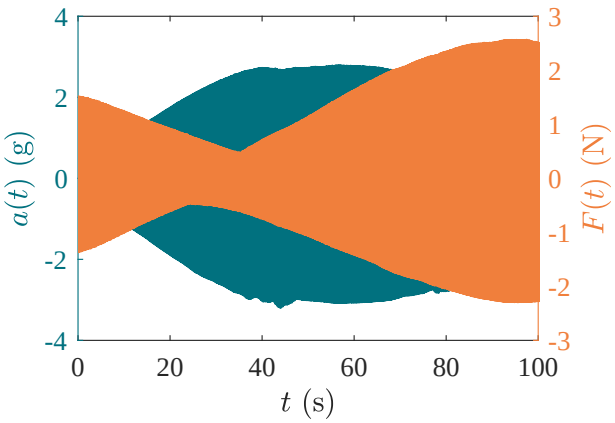

(a) Temporal response of the system and excitation force applied by the shaker.

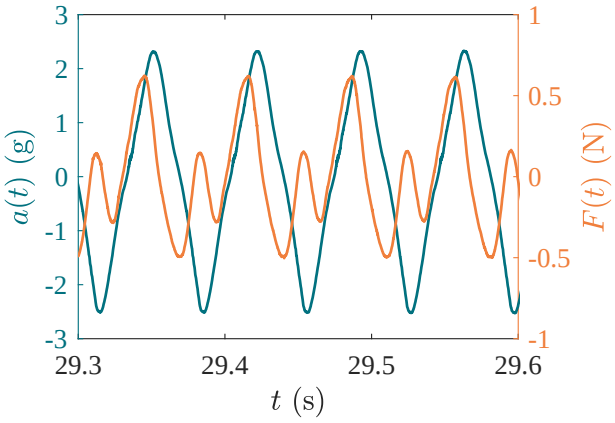

(b) Close-up on the signals at resonance.

Figure 8.7: Force drop-off phenomenon due to shaker-structure interactions. The beam acceleration is measured by the triaxial accelerometer and the force is measured by the impedance head. Non-fundamental harmonics are observed in the excitation force.

An interesting approach to analyse the effects of shaker-structure interactions on the calculated NFRCs involves constructing an NFRC surface from multiple measurements, followed by extracting sections of this surface at constant forcing amplitudes. Such analysis was proposed in [72], where it was observed that this method proved effective in retrieving the structural NFRCs from surface resectioning.

To construct the NFRC surface, the four-level NFRCs drawn with the PLL method implemented in Simulink were used. The surface was interpolated using `griddedInterpolant` MATLAB function. The results of this interpolation are shown in Figure 8.8a. The 0.35 N curve presented in Figure 8.6a is used as an illustrative example of shaker-structure interactions.

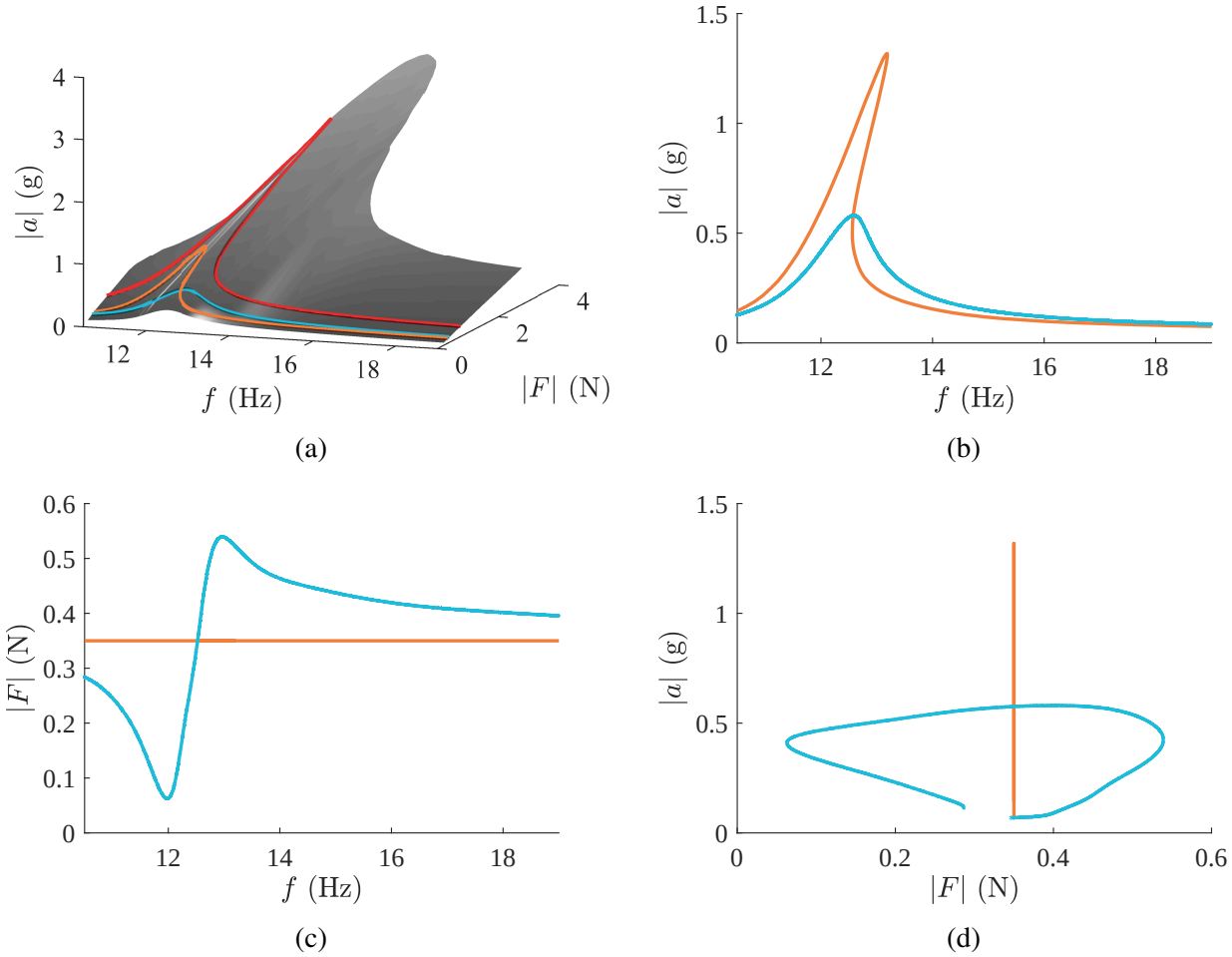

Figure 8.8: Illustration of shaker-structure interactions and force drop-off phenomenon observed during PLL testing on the thin beam. (a) NFRC surface identified by interpolating the computed NFRCs. (b)-(d) Comparison of the NFRC computed at a mean forcing amplitude of 0.35 N (—) and the NFRC obtained by resectioning the NFRC surface at a constant amplitude of 0.35 N (—). (—) represents the limit of the NFRCs that can be resectioned from the surface. For greater forcing amplitudes, the resectioned NFRCs are incomplete, and it would be necessary to use backbone curve measurements to interpolate the NFRC surface.

As observed in Figure 8.8, for this series of experiments, the shaker plays an important role in the system dynamics that were identified with the PLL method. The resonance peak of the NFRC identified with the resectioning method is sharper and happens at a slightly lower frequency. This result can be explained by the fact that, at resonance, the system behaves as if the shaker is driven by the beam. Consequently, at these frequencies, the shaker counteracts and damps the beam's motion, which leads to a reduction in the amplitude of the system response.

It is important to note that in cases of significant shaker–structure interactions, where the excitation force amplitude varies considerably during the experiment, the resulting interpolated NFRC may be

incomplete. In such instances, Zoltan *et al.* [72] propose interpolating an NFRC surface using backbone measurements acquired under various imposed phase lags between the system response and the excitation force, thereby covering the entire NFRC domain. Although this method is more time-consuming, it offers the advantage of controlling the forcing amplitude, and consequently the amplitudes at which the NFRC surface can be resectioned.

8.5 Conclusion and remaining challenges

The results obtained on the three distinct structures analysed in this chapter demonstrate that the LabVIEW-based PLL successfully managed to identify the characteristics of these nonlinear systems.

In terms of performance, the results were comparable to those obtained with the dSPACE MicroLabBox. Both platforms offered similar ease of use through their respective user interfaces and operated on the same underlying principles. These findings are promising for the potential industrial deployment of the PLL implementation in LabVIEW; however, two key issues remain to be addressed.

Firstly, as reviewed in Chapter 4.6, no robust method currently exists for selecting PI controller gains for NFRC tracking. Although this limitation does not impede the identification of backbone curves and stable branches of NFRCs, it becomes critical when entering unstable response regions. For the unstable parts of NFRCs, gain tuning is challenging, and inadequate tuning can precipitate instability, which is illustrated in Figure 8.9. At that time, the controller induces uncontrollable frequency fluctuations and, consequently, large amplitude variations. Without appropriate safety measures in the algorithm, these instabilities could inflict substantial damage on the test structure or exciter.

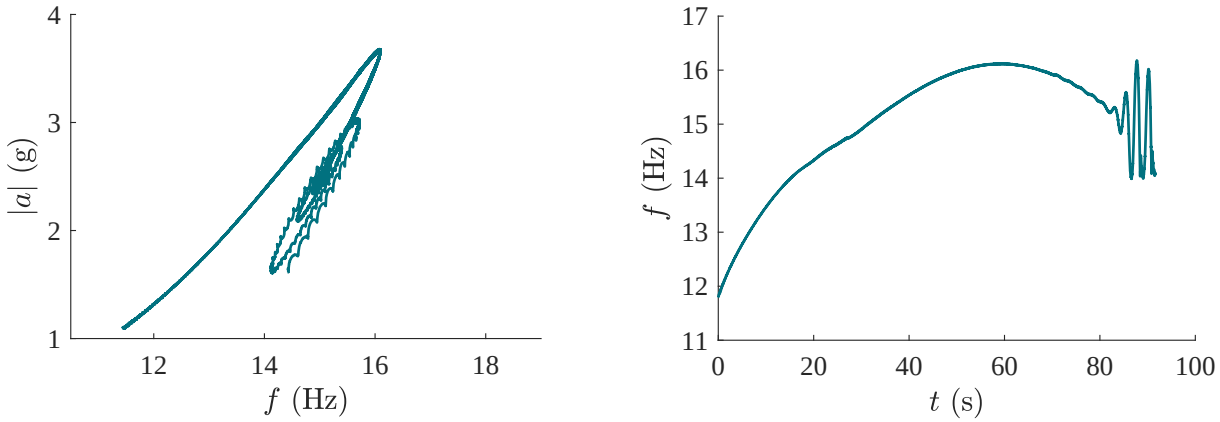

(a) NFRC drawn during the experiment.

(b) Variation of the excitation frequency during the experiment.

Figure 8.9: Unstable results obtained with inappropriate tuning of the controller gains of the PLL algorithm when controlling an unstable response branch.

Secondly, shaker–structure interactions present significant challenges during vibration testing. During the experiments, these interactions manifested as force drop-off and the presence of non-fundamental harmonic components in the applied force. While optimising shaker placement can mitigate these effects, it cannot eliminate them entirely. Several studies have addressed this issue. Abeloos [48] introduced a proportional controller to suppress non-fundamental harmonics in the applied force by adjusting the voltage signal; however, he specifies that the method lacks general

applicability and requires heuristic tuning. Similar investigations were carried out by Woiwode and Krack [31], who focused on controlling the fundamental excitation harmonic. More recently, Gabos *et al.* [72] proposed a post-processing approach to extract NFRCs at constant forcing amplitude, yielding results comparable to those obtained using an amplitude controller on the voltage signal. Although their alternative is more time-consuming, as it requires computing a sufficient amount of NFRCs or backbone curves to reconstruct the NFRC surface, it avoids the additional instability risk associated with amplitude control, which may compromise the structure or the exciter.

9 Nonlinear controller for the phase-locked loop method

Although the use of a PLL method for the characterisation of nonlinear systems is a currently investigated subject, the tuning of the controller gains in the method remains heuristic, as elaborated in Section 4.6. This chapter investigates the solution recently proposed by Chukwu *et al.* [15], who introduced a PLL algorithm incorporating a modified version of the conventional PI controller. This modified approach was termed the nonlinear controller PLL (NCPLL).

The objective of this novel control method, as outlined by Chukwu *et al.*, is to provide a unified approach for determining an upper bound on the controller gain that remains valid across various types of nonlinearities. As a result, Chukwu *et al.* aim to reduce the number of tuning parameters in the PLL method to one, thereby simplifying the gain tuning process.

This chapter presents the principles behind this new control methodology. The method is reviewed by numerically testing the controller on a case study presented in the original article. The results obtained using the NCPLL are subsequently compared with those derived from the classical PLL algorithm.

9.1 Presentation of the nonlinear controller

This section presents the nonlinear controller introduced by Chukwu *et al.* in [15]. The schematic representation of the algorithm incorporating the newly introduced nonlinear controller is shown in Figure 9.1. The underlying principles of the adaptive filter and VCO remain as described in Chapter 4, with the primary modification residing in the controller component.

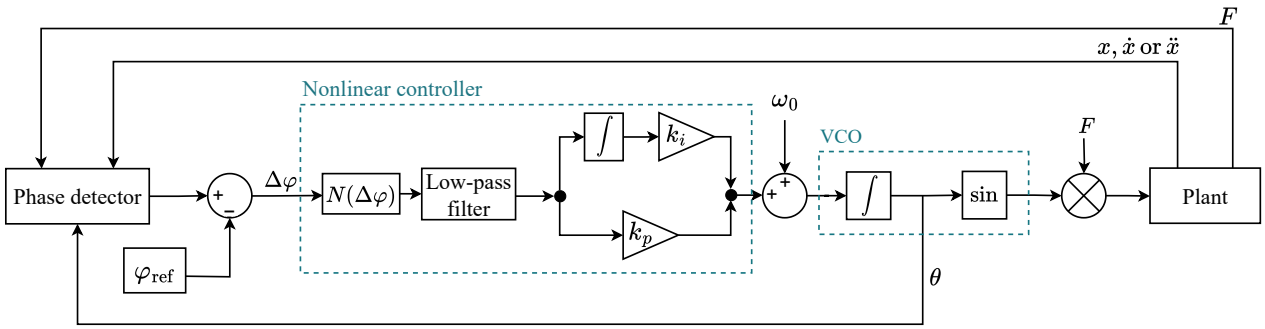

Figure 9.1: Schematic illustration of the NCPLL algorithm.

The nonlinear element $N(\Delta\varphi)$ takes the form of a hyperbolic function of the phase error $\Delta\varphi$, which

corresponds to the difference between the measured phase lag, *i.e.,* the phase difference between the system response and the excitation force, and a specified reference phase lag

$$N(\Delta\varphi) = K_n \tanh \frac{\Delta\varphi}{\beta}, \tag{9.1}$$

where $K_n > 0$ is the gain to be tuned, and $0 < \beta < 1$ is a steepness parameter. This steepness parameter is employed to adjust the influence of the controller on the system. Specifically, a small value of β results in a sharper response and abrupt transitions induced by the controller, while also promoting faster convergence. This value is independent of the system under investigation, and Chukwu *et al.* set it to 0.01, stating that this choice offers an effective compromise between rapid convergence and smooth transitions.

A low-pass filter is introduced in the control technique to remove the high-frequency components of the nonlinear element. The transfer function of this filter takes the following form

$$L(s) = \frac{1}{s/\alpha + 1}, \tag{9.2}$$

where α is the cut-off frequency of the filter and s is the Laplace variable.

In their methodology, Chukwu *et al.* set the open-loop frequency ω_0 to the linear natural frequency of the investigated mode. They also fix the PI controller gains k_i and k_p to unity. The sampling frequency f_s, the number of harmonics in the adaptive filter n_H, and the adaptive filter cut-off frequency $\tilde{\mu}$ are selected according to the guidelines presented in Section 4.7 and detailed in [49]. Consequently, the remaining parameters that require tuning are the low-pass filter cut-off frequency α and the nonlinear gain K_n.

Chukwu *et al.* do not provide a precise methodology for selecting the low-pass filter cut-off frequency. However, they recommend selecting a value of α within the range $1 < \alpha/\tilde{\mu} < 100$, noting that such values effectively suppress the oscillatory component of the phase error $\Delta\varphi$ without significantly slowing down the controller.

An expression for the upper bound of the nonlinear gain is derived by Chukwu *et al.*, and is presented in their paper [15]. This expression reveals that the stability limit of the nonlinear controller is strongly influenced by the low-pass filter cut-off frequency, the linear damping ratio of the system, with and without the exciter, and the modal mass of the exciter.

9.2 Review of the method

This section reviews the novel method by reproducing a numerical experiment originally presented in the referenced study. The experiment is carried out on a Duffing oscillator, whose dynamics are presented in Equation 2.24. Chukwu *et al.* set the following parameters for this oscillator: the linear natural frequency $f_0 = 62.8$ Hz, the damping ratio $\zeta = 0.05\%$, and the nonlinear stiffness coefficient $\alpha_3 = 5 \times 10^5$ N/(kg m^3). They fix the number of harmonics in the adaptive filter $n_H = 10$, the adaptive filter cut-off frequency $\tilde{\mu} = f_0/3$ and the low-pass filter cut-off frequency $\alpha = 30\tilde{\mu}$. Finally, the derived upper bound K_n is 5.919.

In their experiment, Chukwu *et al.* identified the NFRCs of the system for three forcing levels: 1 N, 5 N and 10 N. The results are computed with the advised values for the NCPLL method. Moreover, a computation is also carried out with the classical PLL method, with the integral gain

$k_i = 100\ \mathrm{s}^{-2}$ and the proportional gain $k_p = 25\ \mathrm{s}^{-1}$. The results are shown in Figure 9.2, where it is observed that both methods yield identical results with comparable computation times for similar accuracy. Furthermore, gain tuning for the classical PLL method was not particularly challenging in this scenario.

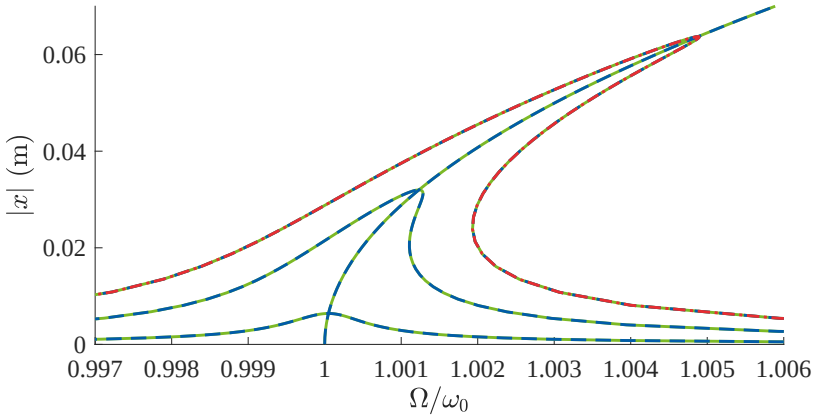

Figure 9.2: NFRCs and backbone curve of the Duffing oscillator obtained with the NCPLL (—) and PLL (—) methods. The NCPLL method was also tested with a controller gain of $3K_n$ (—).

To assess the stability limit, computations were performed using the NCPLL with a controller gain of $3K_n$. The computations revealed that the unstable region of the NFRC could still be stabilised using this gain value, thereby casting doubt on the stated stability limit. Furthermore, no mathematical derivation of this upper bound is provided in [15], leaving the basis for this gain unclear.

Finally, the influence of the cut-off frequency of the low-pass filter was also examined. The NCPLL was tested using various cut-off frequencies, and it was observed that neither the inclusion of the filter nor the specific choice of its cut-off frequency had a significant impact on the stabilisation of the system.

9.3 Conclusion

The methodology presented by Chukwu *et al.* introduces several noteworthy concepts, particularly the inclusion of a nonlinear element, which serves to moderate the influence of the controller on the system and avoid large overshoots in the control. However, the approach proposed by the authors raises certain questions.

Although the authors propose a method that requires the tuning of a single gain parameter, several other parameters of the PLL algorithm, such as the cut-off frequencies of the low-pass filter and the adaptive filter, are assigned arbitrarily in the article, with no clearly defined methodology provided for their selection.

Moreover, the derivation of the upper bound gain K_n is not explicitly detailed in the article, and numerical investigations indicate that this value does not represent a strict upper bound, as the system remains stable for higher gain values. Furthermore, the computation of this upper bound requires knowledge of the modal mass of the exciter, which is not straightforward to determine in the case of experimental application of the NCPLL. Based on these observations, the analysis was limited to the numerical domain and was not extended to experimental validation.

10 Conclusions and perspectives

Nonlinear systems are increasingly encountered during experimental vibration testing. The complex and, at times, erratic behaviour they exhibit renders their analysis particularly challenging. Phenomena such as jumps or secondary resonances, which may appear as attached or detached response branches, further complicate the characterisation of their full dynamic behaviour. Within this framework, classical modal testing methods, such as sine-sweep or dwell tests, are limited in effectiveness, as they only allow the identification of stable periodic orbits of nonlinear systems. Experimental continuation methods address this limitation by introducing a feedback control into the system to stabilise otherwise inaccessible unstable response branches.

In this context, the PLL method presents a promising approach for the experimental reconstruction of bifurcation diagrams around fundamental resonances of nonlinear systems. This derivative-less technique is advantageous as it does not require a mathematical model of the system, which can be highly intricate for complex structures. In experimental analysis, the PLL method enables the identification of NFRCs and backbone curves, which is of particular relevance to companies such as V2i.

This master's thesis was structured around two principal research questions:

(i) Can the PLL method be implemented in LabVIEW to experimentally identify NFRCs and backbone curves of nonlinear systems?

(ii) To what extent is this implementation suitable for application in an industrial context?

The initial chapters of this thesis established the theoretical context and outlined the key challenges addressed in this study. Chapter 2 presented the fundamental principles underlying the dynamics of linear and nonlinear systems, highlighting the foundational distinctions between the two paradigms. The various complex phenomena arising from nonlinear dynamics were also detailed. Chapter 3 reviewed basic concepts of control theory, with a particular emphasis on PID controllers, which underpin the PLL method. The theoretical background concluded with Chapter 4, which established the foundation of experimental continuation methods. The PLL algorithm and working principles were presented, and the adaptive filter, employed as a phase detector within the method, was described in detail.

The first experimentation of the PLL method began with numerical models implemented in Simulink. The PLL method was tested on both linear and nonlinear models, and successfully retrieved the complete bifurcation branches associated with the fundamental resonances. Experimental validation of this implementation was successfully performed on two systems, an electronic Duffing oscillator and a hardening nonlinear beam, both exhibiting unstable branches in their response curves.

The main research question of this thesis was addressed in Chapters 7 and 8, which introduced

the LabVIEW programming environment. This low-level graphical interface is widely employed in vibration testing for control and data acquisition, and is used at V2i for product development. The experimental application of the PLL requires fast and real-time control, which is achieved using an FPGA chip integrated within the LabVIEW hardware. The challenges encountered during the implementation, notably the timing requirements and data size management, were emphasised. The chapter concluded with a comparison between the solutions offered by dSPACE and National Instruments, from which it was concluded that both are suitable for implementing the PLL method. While Simulink offers a high-level interface that facilitates development, LabVIEW enables finer tuning of the algorithm due to its lower-level programmability. For instance, the data type, the data size, and the data exchange between the hardware and the host computer must be explicitly defined in LabVIEW, thereby providing greater insight into how the data are handled during computations.

Finally, Chapter 8 presented the experimental validation of the PLL implementation in LabVIEW. The method was tested on three distinct systems, and successfully retrieved their dynamic characteristics. The results obtained using both implementations showed strong agreement, thereby validating the LabVIEW-based approach. The performance achieved using National Instruments hardware was comparable to that of dSPACE, and no difficulties were encountered in the real-time tracking of systems response using the LabVIEW real-time controller.

10.1 Future work

The PLL method proposed in this thesis offers an promising solution to identify bifurcation diagrams around fundamental resonances of nonlinear systems. However, two main difficulties encountered during the practical applications of the method remain to be investigated.

Firstly, the gain tuning of the PLL method is heuristic. Recent research were conducted on the derivation of a systematic approach for the gain tuning of the PLL algorithm, but no generalised methodology was established. The principal difficulty in this absence of a defined methodology lies in the tracking of unstable responses. Indeed, while the gain tuning of the PLL method when identifying stable portions of NFRCs or backbone curves is relatively straightforward, the controlled system may rapidly become unstable if the tuning is not appropriately adjusted to stabilise unstable orbits.

The methodology employed in the experiments is as follows. The experiments begin with an open-loop system, where the controller gains are initially set to zero. These gains are then gradually increased to a user-defined level, recognising that the integral gain enhances the tracking capability of the controlled system, while the proportional gain contributes to its stability. To accelerate computations during the experiments, the integral gain was often set to relatively high values, typically exceeding the proportional gain. However, when tracking the unstable responses of nonlinear systems, the controller may become unstable, resulting in high-frequency variations in the driving signal. Such erratic behaviour must be avoided during experimental testing, as it may cause damage to either the structure under test or the exciter. Consequently, tracking unstable response branches necessitates a more precise tuning of the algorithm, which can be time-consuming.

Secondly, shaker–structure interactions prevent the application of a constant excitation amplitude to the structure. However, maintaining a constant amplitude is essential during vibration testing to accurately evaluate the structural characteristics. Furthermore, these interactions may introduce harmonic components into the excitation force, which is undesirable.

To mitigate shaker-structure interactions, several solutions were investigated. Abeloos *et al.* [50] proposed incorporating an amplitude controller within the PLL method. The proportional controller introduced in the feedback loop of the PLL aims to regulate the shaker input voltage, thereby suppressing non-fundamental harmonic components in the excitation force. However, this approach is not yet well-established, and no established methodology exists for the tuning of the proportional controller gain. Consequently, improper tuning may induce unstable system responses that could compromise structural integrity; therefore, its application in an industrial context is considered impractical. Gabos *et al.* [72] introduced an extraction technique to retrieve NFRCs of the structure under test based on an NFRC surface identified with classical PLL measurements. The method was compared with results obtained using an amplitude controller, and both approaches exhibited similar outcomes. The outlined methodology offers an appealing alternative as it neither requires further tuning nor entails the risk of instability associated with gain tuning in the PLL method; however, interpolating an NFRC surface demands a substantial number of measurements, which can be time-consuming. Finally, it is worth noting that the experimental configuration can also be adjusted to mitigate the influence of the shaker dynamics on the structure. For instance, minimal shaker–structure interactions are observed when the apparent mass of the structure is significantly greater than the moving mass of the shaker; however, this condition is not always feasible due to practical constraints in the experimental setups.

Following this discussion, it is concluded that the LabVIEW implementation of the PLL technique developed in this thesis can be employed to experimentally extract the dynamic characteristics of nonlinear systems. The method is considered sufficiently mature to support industrial applications focused on identifying backbone curves of fundamental resonances. However, although theoretically applicable, the use of the PLL method to recover unstable response branches remains impractical for industrial deployment, primarily due to the two challenges previously identified. Addressing these issues could constitute the focus of future work.

Bibliography

[1] A. E. C. Meijering, K. Sarlós, C. F. Nielsen, H. Witt, J. Harju, E. Kerklingh, G. H. Haasnoot, A. H. Bizard, I. Heller, C. P. Broedersz, Y. Liu, E. J. G. Peterman, I. D. Hickson, and G. J. L. Wuite, "Nonlinear mechanics of human mitotic chromosomes," *Nature*, vol. 605, pp. 545–550, 2022. https://doi.org/10.1038/s41586-022-05051-y.

[2] J. Ackermann and P. Müller, "Dynamical Behaviour of Nonlinear Multibody Systems Due to Coulomb Friction and Backlash," *IFAC Proceedings Volumes*, vol. 19, pp. 193–198, 1986. https://doi.org/10.1016/S1474-6670(17)59476-8.

[3] P. Castañeda, "The effective mechanical properties of nonlinear isotropic composites," *Journal of the Mechanics and Physics of Solids*, vol. 39, pp. 45–71, 1991. https://doi.org/10.1016/0022-5096(91)90030-R.

[4] R. A. Schapery, "On the characterization of nonlinear viscoelastic materials," *Polymer Engineering and Science*, vol. 9, pp. 295–310, 1969. https://doi.org/10.1002/pen.760090410.

[5] M. R. Shad, G. Michon, and A. Berlioz, "Nonlinear Dynamics of Rotors due to Large Deformations and Shear Effects," *Applied Mechanics and Materials*, vol. 110–116, pp. 3593–3599, 2011. https://doi.org/10.4028/www.scientific.net/AMM.110-116.3593.

[6] H. Ahmadian, H. Jalali, and F. Pourahmadian, "Nonlinear model identification of a frictional contact support," *Mechanical Systems and Signal Processing*, vol. 24, no. 8, p. 2844–2854, 2010. https://doi.org/10.1016/j.ymssp.2010.06.007.

[7] J.-P. Noël, L. Renson, G. Kerschen, B. Peeters, S. Manzato, and J. Debille, "Nonlinear dynamic analysis of an F-16 aircraft using GVT data," in *International Forum on Aeroelasticity and Structural Dynamics (IFASD 2013)*, pp. 990–1002, Royal Aeronautical Society, 2013.

[8] T. Dossogne, J.-P. Noël, C. Grappasonni, G. Kerschen, B. Peeters, J. Debille, M. Vaes, and J. Schoukens, "Nonlinear Ground Vibration Identification of an F-16 Aircraft - Part II: Understanding Nonlinear Behaviour in Aerospace Structures Using Sine-sweep Testing," in *International Forum on Aeroelasticity and Structural Dynamics*, 2015.

[9] CFM International, "RISE Program." https://www.cfmaeroengines.com/rise/, 2025. Accessed June 1, 2025.

[10] G. Raze, G. Abeloos, and G. Kerschen, "Experimental continuation in nonlinear dynamics: recent advances and future challenges," *Nonlinear Dynamics*, vol. 113, pp. 4949—4997, 2025. https://doi.org/10.1007/s11071-024-10543-9.

[11] L. N. Virgin, *Introduction to Experimental Nonlinear Dynamics: A Case Study in Mechanical Vibration*. Cambridge University Press, 2000. https://doi.org/10.1017/9781139175227.

[12] J. Sieber and B. Krauskopf, "Control based bifurcation analysis for experiments," *Nonlinear Dynamics*, vol. 51, p. 365–377, 2008. https://doi.org/10.1007/s11071-007-9217-2.

[13] V. Denis, M. Jossic, C. Giraud-Audine, B. Chomette, A. Renault, and O. Thomas, "Identification of nonlinear modes using phase-locked-loop experimental continuation and normal form," *Mechanical Systems and Signal Processing*, vol. 106, p. 430–452, 2018. https://doi.org/10.1016/j.ymssp.2018.01.014.

[14] T. Karaağaçlı and H. N. Özgüven, "Experimental modal analysis of nonlinear systems by using response-controlled stepped-sine testing," *Mechanical Systems and Signal Processing*, vol. 146, p. 107023, 2021. https://doi.org/10.1016/j.ymssp.2020.107023.

[15] A. C. Chukwu, C. Stephan, C. Touzé, and O. Doaré, "Implementation of a Nonlinear Controller in Phase-Locked Loop Experiments for Nonlinear Structure Identification," *Preprint at SSRN*, 2025. https://dx.doi.org/10.2139/ssrn.5195125.

[16] A. Dimarogonas, "The origins of vibration theory," *Journal of Sound and Vibration*, vol. 140, pp. 181–189, July 1990. https://doi.org/10.1016/0022-460X(90)90523-3.

[17] M. Geradin and D. J. Rixen, *Mechanical Vibrations: Theory and Application to Structural Dynamics*. John Wiley & Sons, Inc., 3rd ed., 2015.

[18] G. Genta, *Vibration Dynamics and Control*. Springer New York, 1st ed., 2009. https://doi.org/10.1007/978-0-387-79580-5.

[19] A. H. Nayfeh and D. T. Mook, *Nonlinear Oscillations*. John Wiley & Sons, Inc., 1995. https://doi.org/10.1002/9783527617586.

[20] G. Kerschen and G. Raze, "Nonlinear vibrations of aerospace structures," 2024-2025. University of Liège. http://www.s3l.be/en/education.

[21] G. Kerschen, M. Peeters, J.-C. Golinval, and A. F. Vakakis, "Nonlinear normal modes, Part I: A useful framework for the structural dynamicist," *Mechanical Systems and Signal Processing*, vol. 23, pp. 170–194, 2009. https://doi.org/10.1016/j.ymssp.2008.04.002.

[22] B. Peeters, H. Van Der Auweraer, P. Guillaume, and J. Leuridan, "The PolyMAX Frequency-Domain Method: A New Standard for Modal Parameter Estimation?," *Shock and Vibration*, vol. 11, no. 3-4, pp. 395–409, 2004. https://doi.org/10.1155/2004/523692.

[23] I. Kovacic and M. J. Brennan, eds., *The Duffing Equation: Nonlinear Oscillators and their Behaviour*. John Wiley & Sons, Inc., 1st ed., 2011. https://doi.org/10.1002/9780470977859.

[24] P. J. Holmes and D. A. Rand, "The bifurcations of Duffing's equation: An application of catastrophe theory," *Journal of Sound and Vibration*, vol. 44, p. 237–253, January 1976. https://doi.org/10.1016/0022-460X(76)90771-9.

[25] R. M. Rosenberg, "Normal Modes of Nonlinear Dual-Mode Systems," *Journal of Applied Mechanics*, vol. 27, pp. 263–268, 1960. https://doi.org/10.1115/1.3643948.

[26] S. W. Shaw and C. Pierre, "Non-linear normal modes and invariant manifolds," *Journal of Sound and Vibration*, vol. 150, pp. 170–173, 1991. https://doi.org/10.1016/0022-460X(91)90412-D.

[27] M. Volvert and G. Kerschen, "Characterizing Fundamental, Superharmonic, and Subharmonic Resonances Using Phase Resonance Nonlinear Modes," in *Advances in Nonlinear Dynamics: Proceedings of the Second International Nonlinear Dynamics Conference*, vol. 1 of *NODYCON Conference Proceedings Series*, pp. 661–671, Springer Cham, 2021. https://doi.org/10.1007/978-3-030-81162-4.

[28] S. Peter, R. Riethmüller, and R. I. Leine, "Tracking of Backbone Curves of Nonlinear Systems Using Phase-Locked-Loops," in *Nonlinear Dynamics, Volume 1* (G. Kerschen, ed.), Conference Proceedings of the Society for Experimental Mechanics Series, p. 107–120, Springer International Publishing, 2016. https://doi.org/10.1007/978-3-319-29739-2_11.

[29] M. Krack and J. Gross, *Harmonic Balance for Nonlinear Vibration Problems*. Mathematical Engineering, Springer Cham, 1st ed., 2019. https://doi.org/10.1007/978-3-030-14023-6.

[30] R. M. Rosenberg, "On Nonlinear Vibrations of Systems with Many Degrees of Freedom," *Advances in Applied Mechanics*, vol. 9, p. 155–242, 1966. https://doi.org/10.1016/S0065-2156(08)70008-5.

[31] L. Woiwode and M. Krack, "Experimentally uncovering isolas via backbone tracking," *Journal of Structural Dynamics*, pp. 122–143, 2024. https://doi.org/10.25518/2684-6500.180.

[32] T. Detroux, L. Renson, L. Masset, and G. Kerschen, "The harmonic balance method for bifurcation analysis of large-scale nonlinear mechanical systems," *Computer Methods in Applied Mechanics and Engineering*, vol. 296, pp. 18–38, 2015. https://doi.org/10.1016/j.cma.2015.07.017.

[33] M. Li and G. Haller, "Nonlinear analysis of forced mechanical systems with internal resonance using spectral submanifolds, Part II: Bifurcation and quasi-periodic response," *Nonlinear Dynamics*, vol. 110, no. 2, p. 1045–1080, 2022. https://doi.org/10.1007/s11071-022-07476-6.

[34] K. Hirai and N. Sawai, "A general criterion for jump resonance of nonlinear control systems," *IEEE Transactions on Automatic Control*, vol. 23, pp. 896–901, 1978. https://doi.org/10.1109/TAC.1978.1101850.

[35] R. J. Kuether, L. Renson, T. Detroux, C. Grappasonni, G. Kerschen, and M. S. Allen, "Nonlinear normal modes, modal interactions and isolated resonance curves," *Journal of Sound and Vibration*, vol. 351, p. 299–310, 2015. https://doi.org/10.1016/j.jsv.2015.04.035.

[36] G. Habib, G. I. Cirillo, and G. Kerschen, "Isolated resonances and nonlinear damping," *Nonlinear Dynamics*, vol. 93, p. 979–994, 2018. https://doi.org/10.1007/s11071-018-4240-z.

[37] O. Mayr, *The Origins of Feedback Control*. The M.I.T. Press, 1970.

[38] S. S. Nudehi, U. Farooq, A. Alasty, and J. Issa, "Satellite attitude control using three reaction wheels," in *2008 American Control Conference*, (Seattle, WA, USA), pp. 4850–4855, IEEE, 2008. https://doi.org/10.1109/ACC.2008.458.

[39] A. Sider, C. Di Fronzo, L. Amez-Droz, A. Amorosi, F. Badaracco, P. Baer, A. Bertolini, G. Bruno, P. Cebeci, and C. Collette, "E-TEST: a compact low-frequency isolator for a large cryogenic mirror," *Classical and Quantum Gravity*, vol. 40, p. 165002, 2023. https://doi.org/10.1088/1361-6382/ace230.

[40] T. P. Hughes, *Elmer Sperry: Inventor and Engineer*. Johns Hopkins University Press, Baltimore, 1971.

[41] C. W. Rowley and B. A. Batten, "Dynamic and Closed-Loop Control," in *Fundamentals and Applications of Modern Flow Control*, vol. 231, pp. 115–148, American Institute of Aeronautics and Astronautics, 2009.

[42] G. F. Frankin and J. D. Powell and A. F. Emami-Naeini, *Feedback Control of Dynamic Systems*. Pearson, 8th ed., 2020.

[43] A. Sharma, "Characteristics of RCIM Sensors." https://www.yourelectricalguide.com/2022/02/characteristics-of-rcim-sensors.html, 2022. Accessed March 28, 2025.

[44] K. J. Åström and R. M. Murray, *Feedback Systems: An Introduction for Scientists and Engineers*. Princeton University Press, 2nd ed., 2020. Available online at https://www.cds.caltech.edu/~murray/amwiki/.

[45] A. Callender, D. R. Hartree, and A. Porter, "Time-Lag in a Control System," *Philosophical Transactions of the Royal Society of London*, vol. 235, no. 756, pp. 415–444, 1936. https://doi.org/10.1098/rsta.1936.0007.

[46] J. G. Ziegler and N. B. Nichols, "Optimum Settings for Automatic Controllers," *Transactions of the American Society of Mechanical Engineers*, vol. 64, no. 8, pp. 759–765, 1942. https://doi.org/10.1115/1.4019264.

[47] S. Mojrzisch, J. Wallaschek, and J. Bremer, "An Experimental Method for the Phase Controlled Frequency Response Measurement of Nonlinear Vibration Systems," *Proceedings Applied Mathematics and Mechanics*, vol. 12, no. 1, p. 253–254, 2012. https://doi.org/10.1002/pamm.201210117.

[48] G. Abeloos, *Control-based methods for the identification of nonlinear structures*. PhD thesis, University of Liège, 2022.

[49] P. Hippold, M. Scheel, L. Renson, and M. Krack, "Robust and fast backbone tracking via phase-locked loops," *Mechanical Systems and Signal Processing*, vol. 220, p. 111670, 2024. https://doi.org/10.1016/j.ymssp.2024.111670.

[50] G. Abeloos, F. Müller, E. Ferhatoglu, M. Scheel, C. Collette, G. Kerschen, M. R. W. Brake, P. Tiso, L. Renson, and M. Krack, "A consistency analysis of phase-locked-loop testing and control-based continuation for a geometrically nonlinear frictional system," *Mechanical Systems and Signal Processing*, vol. 170, p. 108820, 2022. https;//doi.org/10.1016/j.ymssp.2022.108820.

[51] G. Abeloos, L. Renson, C. Collette, and G. Kerschen, "Stepped and swept control-based continuation using adaptive filtering," *Nonlinear Dynamics*, vol. 104, no. 4, p. 3793–3808, 2021. https://doi.org/10.1007/s11071-021-06506-z.

[52] S. Haykin, *Adaptive Filter Theory*. Prentice Hall, 2002.

[53] T. Zhou, G. Raze, G. Kosova, and G. Kerschen, "Experimental Nonlinear Modal Analysis of an F-16 Aircraft using Phase-locked Loop Control," *Journal of Aircraft*, 2025.

[54] M. Peeters, G. Kerschen, and J.-C. Golinval, "Dynamic testing of nonlinear vibrating structures using nonlinear normal modes," *Journal of Sound and Vibration*, vol. 330, no. 3, p. 486–509, 2011. https://doi.org/10.1016/j.jsv.2010.08.028.

[55] G. Raze, "An electronic Duffing oscillator." https://github.com/GhislainRaze/Electronic-Duffing, 2025. Accessed February 25, 2025.

[56] Z. Gabos and Z. Dombovari, "Open-loop swept frequency response of nonlinear structures subjected to weak coupling," *Nonlinear Dynamics*, vol. 113, no. 6, p. 5091–5108, 2025. https://doi.org/10.1007/s11071-024-10546-6.

[57] H. Amano, ed., *Principles and Structures of FPGAs*. Springer Singapore, 1st ed., 2018. https://doi.org/10.1007/978-981-13-0824-6.

[58] I. Kuon, R. Tessier, and J. Rose, "FPGA Architecture: Survey and Challenges," *Foundations and Trends in Electronic Design Automation*, vol. 2, pp. 135–253, 2008. https://doi.org/10.1561/1000000005.

[59] J. Serrano, "Introduction to FPGA design," *CAS - CERN Accelerator School: Digital Signal Processing*, pp. 231–247, 2008. https://doi.org/10.5170/CERN-2008-003.231.

[60] W. Wolf, *FPGA-Based System Design*. Prentice Hall, 2004.

[61] M. M. Mano, C. R. R. Kime, and T. Martin, *Logic and Computer Design Fundamentals*. Pearson, 5th ed., 2016.

[62] T. Travis and J. Kring, *LabVIEW for Everyone: Graphical Programming Made Easy and Fun*. Prentice Hall, 3rd ed., 2006.

[63] National Instruments, "CompactRIO Systems." https://www.ni.com/en/shop/compactrio.html, 2025. Accessed April 1, 2025.

[64] National Instruments, "cRIO-9054 Specifications." https://www.ni.com/docs/en-US/bundle/crio-9054-specs/page/specs.html, 2025. Accessed April 1, 2025.

[65] National Instruments, "Introduction to FPGA Hardware Concepts." https://www.ni.com/docs/en-US/bundle/labview-fpga-module/page/introduction-to-fpga-hardware-concepts-fpga-module.html, 2025. Accessed April 1, 2025.

[66] W. Zhao, E. Belhaire, V. Javerliac, C. Chappert, and B. Dieny, "A non-volatile Flip-Flop in Magnetic FPGA chip," in *International Conference on Design and Test of Integrated Systems in Nanoscale Technology*, pp. 323 – 326, 2006. 10.1109/DTIS.2006.1708702.

[67] National Instruments, "NI-9234." https://www.ni.com/nl-be/shop/model/ni-9234.html, 2025. Accessed April 1, 2025.

[68] National Instruments, "NI-9263." https://www.ni.com/docs/en-US/bundle/ni-9263-specs/page/specs.html, 2025. Accessed April 1, 2025.

[69] National Instruments, "LabVIEW FPGA Module User Manual." https://www.ni.com/docs/en-US/bundle/labview-fpga-module/page/user-manual-welcome.html, 2025. Accessed April 5, 2025.

[70] National Instruments, "Optimizing FPGA VIs Using Pipelining." https://www.ni.com/docs/en-US/bundle/labview-fpga-module/page/optimizing-fpga-vis-using-pipelining-fpga-module.html, 2025. Accessed April 4, 2025.

[71] M. Tang, C. Stephan, and M. Böswald, "Phase resonance method for nonlinear mechanical structures with phase locked loop control," in *ISMA International Conference on Noise and Vibration Engineering*, 2020.

[72] Z. Gabos, G. Raze, G. Kerschen, and Z. Dombovari, "Extraction technique of nonlinear frequency response curves on coupling-affected structures through phase-locked loop testing," *Under review*, 2025.

A Simulink diagrams

A.1 Phase-locked loop method

The Simulink implementation of the PLL method, as illustrated in Figure 4.1, is presented in the present appendix.

In Figure A.1, the integrated excitation frequency $\theta(t)$ and the system response $x(t)$ are fed back into the adaptive filter. A Fourier basis with n_H harmonics is constructed from the instantaneous excitation frequency, and the coefficients associated to these harmonics are computed using the LMS algorithm presented in Equation 4.6. The Fourier coefficients corresponding to the k-th harmonic,

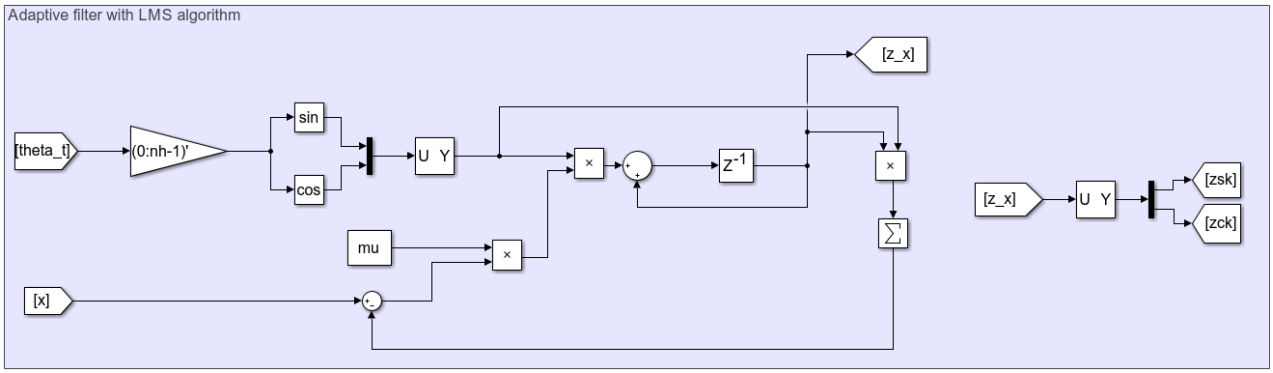

(a)

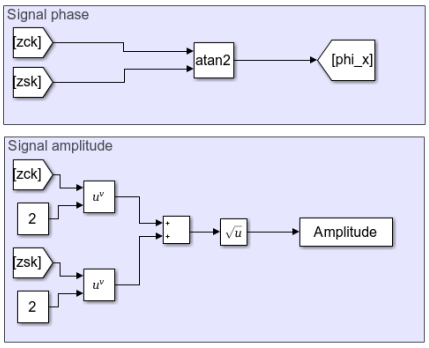

(b)

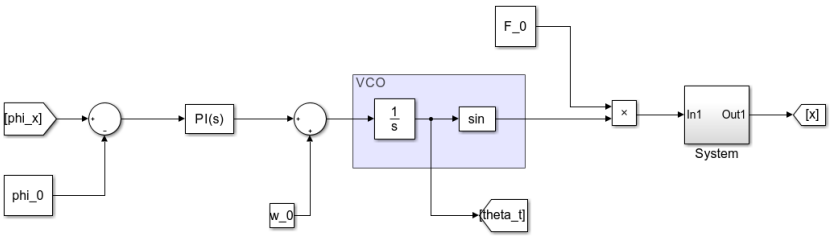

(c)

Figure A.1: Simulink implementation of the PLL algorithm. Subfigure (a) presents the implementation of the adaptive filer with the LMS algorithm. Subfigure (b) shows the computation of the phase lag and amplitude of the k-th harmonic of the signal, as decomposed by the adaptive filter. Subfigure (c) shows the implementation of the PI controller and the VCO.

denoted z_{sk} and z_{ck}, are then extracted to retrieve the amplitude and the phase of the selected harmonic of the signal. In the PLL experiments, the fundamental harmonic was consistently selected. Finally, the phase difference between the system response and the excitation force is compared to the reference phase lag, and the resulting error is fed into a PI controller. The controller output provides a frequency variation used to excite the system and drive it to the desired state through a VCO. The amplitude of the excitation force is selected by the experimenter.

B Experimental modal analysis of the nonlinear beam

This appendix presents the experimental modal analysis (EMA) performed on the nonlinear beam presented in Section 6.4 and shown in Figure 6.4. The objective of this EMA is to identify the first three linear modes of the beam.

B.1 Setup description

The EMA was conducted using V2i Acquisitor software. An impact hammer with a sensitivity of 2.23 mV/N and fitted with a vinyl tip was used to excite the structure. The choice of vinyl material was appropriate, as the study focused on responses in the medium-frequency range. The tests involved roving a triaxial accelerometer, with measurement points uniformly spaced at 10 cm intervals along the beam. The impact point was located 25 cm from the left end of the beam. A schematic of the testing setup is presented in Figure B.1.

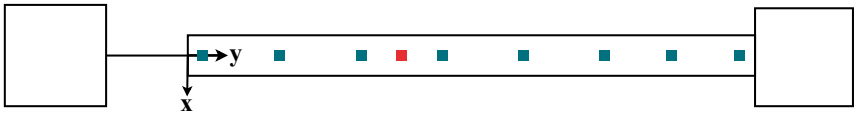

Figure B.1: Schematic of the testing setup of the nonlinear beam. Measurement points (■) and impact point (■) are highlighted.

To mitigate the effects of the leakage that occur due to the imperfect periodicity of the signals, windows were used. As the hammer signal resembles a Dirac peak, a uniform window was applied to the excitation signal; for the measured acceleration, an exponential window was added, as the structure is naturally damped. Finally, to reduce the randomness effects that can appear during experimental testing, three measurements were averaged for the FRFs collected at each measurement point.

B.2 Results

The EMA proved particularly useful for computing the FRFs of the structure along the excitation direction, denoted x, and its perpendicular direction z. The sum of the eight measured FRFs and their corresponding coherence functions, is presented in Figure B.2.

As observed in Figure B.2a, three resonance frequencies appear in the direction of excitation, at approximately 35 Hz, 140 Hz, and 400 Hz. Concerning the z direction, two modes are distinguished,

one at about 87 Hz and another at 270 Hz. The two coherence functions indicate a high coherence in the results, especially near the resonance frequencies, validating the accuracy of the measurements.

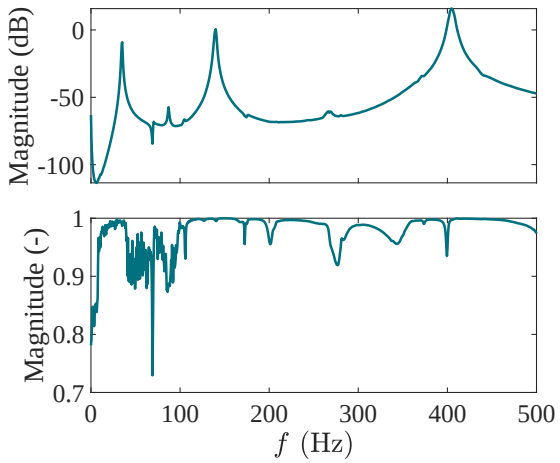

(a) FRF in the x direction and its corresponding coherence function.

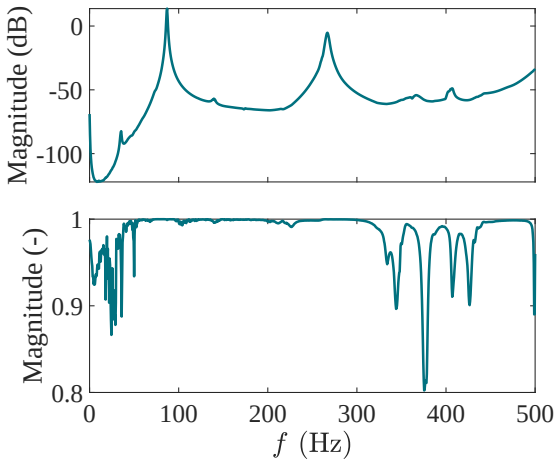

(b) FRF in the z direction and its corresponding coherence function.

Figure B.2: Sum of the eight measured FRFs of the nonlinear beam in the 0 – 500 Hz frequency range (top) and their corresponding coherence functions (bottom).

Moreover, it is essential to verify the excitation signals when conducting an EMA. In the case of hammer excitation, the power spectral density (PSD) of the input force provides valuable insight. As observed in Figure B.3, the vinyl tip excites the frequency range of interest almost equally. Indeed, the use of a vinyl tip, classified as medium-hardness, limits the excitation bandwidth, thus focusing the excitation on the frequency range of interest.

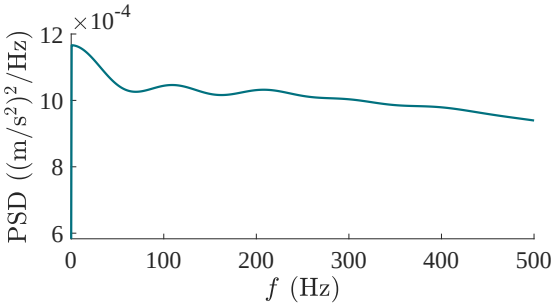

(a) Average of the PSD of the hammer impacts in the x direction.

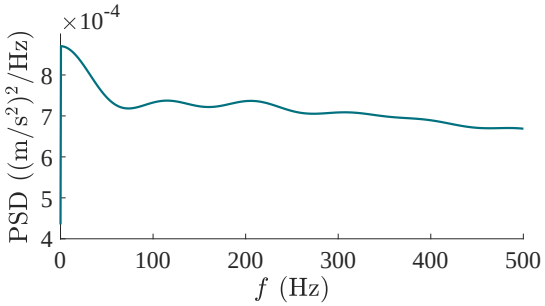

(b) Average of the PSD of the hammer impacts in the z direction.

Figure B.3: Average of the PSD of the hammer impacts.

Finally, the EMA concludes with a presentation of the three modes of interest. This preliminary analysis provides quantitative indication of the ideal location for the accelerometer and the impedance head, which will subsequently be used to experimentally extract the NFRCs and backbone curves of the first three modes of the system using the PLL method. Furthermore, it should be noted that this type of EMA is particularly relevant for obtaining a linear basis for industrial applications where systems exhibit nonlinear behaviour even at the lowest excitation levels achievable with a shaker.

The first three modes have been identified using a stabilisation diagram, computed with PolyMAX method for a polynomial order of 70 [22]. The mode shapes and the stabilisation diagram were computed in LMS software, and the results are shown in Figure B.4. As observed in the three mode shapes, the displacement at the left end of the beam, located at $y = 0$ cm, is significant across all three modes, making it a suitable location for the accelerometer. Regarding the excitation point, it must be positioned such that all three modes are responsive to the excitation, meaning it should not be placed at a nodal point of the beam. Consequently, the shaker was positioned 30 cm from the left edge of the beam ($y = 30$ cm), where the first three horizontal modes exhibit varying degrees of response.

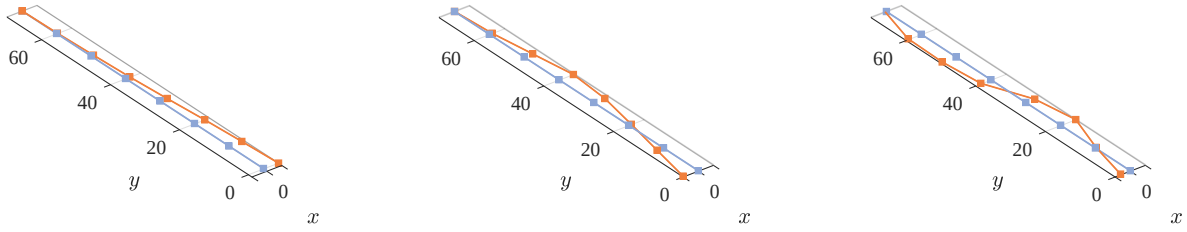

(a) First mode at 34.7 Hz. (b) Second mode at 139.2 Hz. (c) Third mode at 406.3 Hz.

Figure B.4: Firsts three mode shapes of the nonlinear beam in the direction of excitation (—). The undeformed structure is also illustrated (—).